The Interaction of Water and 2:1 Layer Silicates

Zur Erlangung des akademischen Grades eines

DOKTORS DER NATURWISSENSCHAFTEN

von der Fakultät für

Bauingenieur-, Geo- und Umweltwissenschaften

des Karlsruher Instituts für Technologie (KIT)

genehmigte

DISSERTATION

von

M.Sc. Florian Schnetzer

aus Kandel

Tag der mündlichen Prüfung: 15.02.2017

Referentin: PD Dr. Katja Emmerich

Korreferent: Prof. Dr. Thorsten Schäfer

Karlsruhe (2017)

Eidesstattliche Versicherung

Eidesstattliche Versicherung gemäß § 6 Abs. 1 Ziff. 4 der Promotionsordnung des Karlsruher Instituts für Technologie für die Fakultät für Bauingenieur-, Geo- und Umweltwissenschaften.

1. Bei der eingereichten Dissertation zu dem Thema „The interaction of water and 2:1 layer silicates" handelt es sich um meine eigenständig erbrachte Leistung.

2. Ich habe nur die angegebenen Quellen und Hilfsmittel benutzt und mich keiner unzulässigen Hilfe Dritter bedient. Insbesondere habe ich wörtlich oder sinngemäß aus anderen Werken übernommene Inhalte als solche kenntlich gemacht.

3. Die Arbeit oder Teile davon habe ich wie folgt/ bislang nicht an einer Hochschule des In- oder Auslands als Bestandteil einer Prüfungs- oder Qualifikationsleistung vorgelegt.

Titel der Arbeit: The interaction of water and 2:1 layer silicates

Hochschule und Jahr: Karlsruher Instituts für Technologie 2017

4. Die Richtigkeit der vorstehenden Erklärungen bestätige ich.

5. Die Bedeutung der eidesstattlichen Versicherung und die strafrechtlichen Folgen einer unrichtigen oder unvollständigen eidesstattlichen Versicherung sind mir bekannt.

Ich versichere an Eides statt, dass ich nach bestem Wissen die reine Wahrheit erklärt und nichts verschwiegen habe.

Karlsruhe, 09.03.2017   Florian Schnetzer

Acknowledgement

IV

Summary

The interaction of solid surfaces with water is one of the most important reactions in nature and in industry. This work focuses on clay mineral surfaces. Clay minerals are ubiquity on earth and used in a broad range of applications thus desiring highest interest in research.

Clay minerals are characterized by a very small particle size and are regarded as natural nanoparticles. Small particle size results in a large specific surface area, which makes it possible to bind large amounts of water. In the case of the swellable 2:1 layer silicates, water is bind additionally by hydration of the interlayer cations. This hydratration enables 2:1 layer silicates to adsorb water up to 700% of their dry weight, but this is strongly influenced by factors such as layer charge, charge density, hydration properties of interlayer cations, particle size distribution and surface properties.

The aim of this thesis was to discriminate water binding mechanisms in 2:1 layer silicates and to study how their structural intrinsic properties affect their hydration behavior using different methods in dependence of the smectite and vermiculite structure. To achieve this goal, the project pursued a series of interrelated activities.

In the first part of this thesis, several 2:1 layer silicates were selected with respect to their layer charge, charge location (octahedral vs. tetrahedral charge) and morphology. Four bentonites, a vermiculite and a fine grained illite sample were chosen to study the influence of structural intrinsic properties on the hydration characteristics of 2:1 layer silicates. Prior to homoionic saturation all materials were Na^+-exchanged. For characterization of the structure X-ray diffraction (XRD) analysis, chemical analysis and simultaneous thermal analysis (STA) were applied. The layer dimension and stacking was determined using microscopical methods, gas adsorption analysis and XRD, which clarified the differences in edge site proportions of the selected 2:1 layer silicates.

After a fundamental understanding of smectites, vermiculite and illite properties, a particular emphasis was placed on the study of water vapor de- and adsortions isotherms. Thereby, the water uptake was determined by gravimetrical and volumetrical techniques. XRD patterns were used to determine differences in hydration states for adsorption-desorption isotherms. In order to detect the respective number of

H_2O molecules per Na^+ of each sample equilibrated at different r.h. the values were collected on the desorption branch of the water vapor sorption isotherms. For the samples stored at 53 % r.h. a 1W hydration state was observed for all smectite samples. The corresponding water contents ranged between 5.9 and 10 H_2O / Na^+ and implied that a mono-hydrated (1W) state can even exist at water contents above 6 H_2O / Na^+. On the desorption branches of all swellable 2:1 layer silicates, clear changes between 6 and 4 H_2O / Na^+ in the gradient could be assigned. These transitions could not be clearly identified on the adsorption branches of the smectite isotherms. However, since the gravimetrical water vapor sorption isotherms are kinetically controlled, the equilibration times and their corresponding change in gradient enable a discrimination between different hydration states in 2:1 layer silicates. Domains in the de- and adsorption of water vapor of the smectite samples with a slightly increasing slope were explained by a heterogeneous layer charge distribution, which enables the coexistence of different hydration states even under controlled conditions.

Additionally, the question has been raised of whether a full dehydration can be observed using only dry nitrogen at ambient conditions. For this purpose, isothermal long-time measurements were carried out at 35 °C (nominal). These results showed that for a complete dehydration of the selected 2:1 layer silicates a temperature above 40 °C is required. A tightly bound water after isothermal treatment was observed for all samples. For dioctahedral smectites a trend with increasing layer charge was observed. Increasing the layer charge resulted in a higher amount of residual moisture. In addition, a tightly bound water was also observed for the Na^+-exchanged illite sample indicating that the exchangeable cations hydrate in the same manner as in the smectites samples.

Particular interest was focused on the differentiation of bulk water and water bound in the hydration shell of the interlayer cation. Thereby, infrared spectroscopic measurements were carried out to get a model on molecular scale and to investigate the microscopic structure of water de- and adsorption.

The purpose of the first IR study was to investigate coupled processes of (de-)hydration and changes in the 2:1 layer of a Na^+-exchanged dioctahedral smectite using in situ IR transmission spectroscopy. The key to this work was the sample preparation technique tethering by aggregation and growth (T-BAG) applied on clays for the first time. Thin

films of 200 nm of a pure smectite sample were prepared on the silicon wafers and scanning electron microscopy confirmed that T-BAG is perfectly reproducible for the use of clay minerals in future. The observed shift of δ(H-O-H) and (Si-O)^{LO} to lower wavenumbers was correlated to an increase of water-surface attraction, which means that the water molecules are highly polarized in the mono-hydrated state (1W layer) and have a lower O-H bending mode (1628 cm^{-1}) compare to liquid water (1643 cm^{-1}). The increase of surface-water attractions with increasing temperature was displayed in a coupled shift of the longitudinal optical Si-O phonon mode to lower wavenumber. As a result, the montmorillonite lattice constants decrease along the a- and b-axis as a function of dehydration. The total-energy and ground-state structure calculations in the present work were performed using DFT as implemented in the Vienna ab initio simulation program (VASP) and done by Dr. Peter Thissen.

In the first IR study, the mechanism was observed at the transition from 1W to 0W state. In a further IR study the focus was on the transition from the 2W to 1W hydration state (and backwards) and the influence of layer charge and octahedral composition. Thereby, the selected materials were studied by an *in-situ* method that allowed FTIR spectra and water vapor sorption isotherms to be obtained simultaneously. The aim of this study was to elucidate the hysteresis mechanism in 2:1 layer silicates during desorption and adsorption of water vapor. Whereas hysteresis was observed over the entire isothermal range of the smectites, the isotherm of the vermiculite sample only showed hysteresis in the transition from 0W to 1W and 1W to 2W state. It was also shown that hysteresis is a function of the layer charge distribution, the achieved water content and the particle size with resulting edge site contribution. Increasing the edge site proportions resulted in an increased hysteresis. The findings from the experimental FTIR/gravimetric analysis showed that the transition from 2W to 1W and backwards is visible using IR spectroscopy. The shifting of δ(H-O-H) was influenced by the layer charge, charge distribution, octahedral substitutions and the layer dimension. Finally, the experimental results were supported by *ab initio* thermodynamic simulations that revealed the different shifting behavior of δ(H-O-H) related to the differences in surface charge density and octahedral compositions.

Kurzfassung

Die Wechselwirkung von Wassermolekülen mit Festkörperoberflächen ist eine der bedeutendsten Reaktionen in Natur und Technik. Im Fokus dieser Arbeit stehen dabei Tonmineraloberflächen. Tonminerale sind ubiquitär und werden in einer Vielzahl von geotechnischen und technischen Anwendungen eingesetzt.

Tonminerale sind natürliche Nanopartikel mit einer großen spezifischen Oberfläche, die es ermöglicht, große Wassermengen zu binden. Bei den quellfähigen Tonmineralen findet die Wasseranlagerung zusätzlich durch Hydratation der Zwischenschichtkationen statt. Diese ermöglichen eine Wasseraufnahme von bis zu 700% des Eigengewichtes des quellfähigen Tonminerals. Dies wird durch eine Reihe an Eigenschaften, wie der Schichtladung, Ladungsverteilung, Hydratationseigenschaften des Zwischenschichtkations, Partikelgrößenverteilung und den Oberflächeneigenschaften der 2:1 Schichtsilicate bestimmt.

Das Ziel dieser Arbeit war es, die Wasserbindungsmechanismen in 2:1 Schichtsilicaten zu untersuchen und wie deren strukturellen Eigenschaften das Hydratationsverhalten beeinflussen. Dies erfolgte mit Hilfe unterschiedlicher Messmethoden. Um dieses Ziel zu erreichen, verfolgt das Projekt eine Reihe von miteinander verbundenen Aktivitäten.

Im ersten Teil dieser Arbeit wurden mehrere 2:1 Schichtsilicate hinsichtlich ihrer Schichtladung, Ladungsverteilung (oktaedrische vs. tetraedrische Ladung) und der Morphologie ausgewählt. Vier Bentonite, ein Vermiculit und ein feinkörniger Illit wurden ausgewählt, um den Einfluss der strukturellen intrinsischen Eigenschaften auf die Hydratationseigenschaften von 2:1 Schichtsilicaten zu untersuchen. Die ausgewählten Materialien wurden aufgereinigt und in der Tonfraktion (< 2 µm) angereichert. Nach homoionischer Na^+-Sättigung wurden die mineralogische und chemische Zusammensetzung der 2:1 Schichtsilicate mittels Röntgenbeugung, Röntgenfloureszenzanalyse, optische Emissionsspektrometrie mittels induktiv gekoppelten Plasmas (ICP-OES) und der simultane thermische Analyse (STA) untersucht. Die Partikelgrößen und -verteilung wurde unter Verwendung mikroskopischer Verfahren, der Gasadsorptionsanalyse und der Röntgenbeugung

bestimmt, wodurch die Unterschiede der Kantenanteile der ausgewählten 2:1 Schichtsilicate verdeutlicht wurden.

Ein besonderes Augenmerk lag auf der Untersuchung von Wasserdampf De- und Adsorptionsisothermen. Dabei wurde die Wasseraufnahme durch gravimetrische und volumetrische Methoden bestimmt. Um die basalen Abstände in den jeweiligen Hydratationszuständen zu bestimmen, wurden Röntgendiffraktogramme in Abhängigkeit der relativen Luftfeuchte aufgenommen. Die Proben wurden bei unterschiedlichen relativen Luftfeuchten gelagert und deren Anzahl an H_2O Molekülen pro austauschbaren Na^+ wurde auf dem Desorptionszweig der Wasserdampf-Sorptionsisothermen bestimmt. Für die Smectitproben, die bei 53% r.h. vorgesättigt wurden, war immer ein 1W-Hydratationszustand zu beobachten. Der entsprechende Wassergehalt lag zwischen 5,9 und 10 H_2O / Na^+ und deutete an, dass der mono-hydratisierte Zustand auch bei Wassergehalten über 6 H_2O / Na^+ vorliegt. Auf den Desorptionszweigen aller quellfähigen 2:1 Schichtsilicate konnten im Gradienten klare Änderungen zwischen 6 und 4 H_2O / Na^+ zugeordnet werden. Auf den Adsorptionsästen der Smectit Isothermen konnten diese Übergänge jedoch nicht eindeutig gezeigt werden. Da jedoch die gravimetrische Wasserdampfsorption kinetisch gesteuert ist, ermöglichte die Betrachtung der Äquilibrierungszeiten und den entsprechenden Änderungen in der Steigung auch eine Unterscheidung zwischen verschiedenen Hydratationszuständen in der Wasserdampfadsorption von 2:1 Schichtsilicaten. Weiterhin wurden Bereiche in den Wasserdampfadsorptions-isothermen der Smectitproben festgestellt, die nicht mit den bekannten Isothermentypen beschrieben werden konnten. Diese Bereiche wurden durch eine heterogene Ladungsverteilung erklärt, die die Koexistenz verschiedener Hydratationszustände auch unter kontrollierten Bedingungen ermöglicht.

Es stellte sich weiterhin die Frage, ob eine vollständige Dehydratation auch unter Verwendung von trockenem Stickstoff bei Umgebungsbedingungen beobachtet werden kann. Zu diesem Zweck wurden isotherme Langzeitmessungen bei 35 ° C (nominal) durchgeführt. Diese Ergebnisse zeigten, dass für eine vollständige Dehydratation der ausgewählten 2:1 Schichtsilicate mittels N_2 eine Temperatur über 40 ° C erforderlich ist. Ein fest gebundenes Wasser nach isothermer Behandlung wurde für alle Proben beobachtet. Für dioktaedrische Smectite wurde ein Trend mit zunehmender Schichtladung beobachtet. Eine Erhöhung der Schichtladung führte zu

einer höheren Restfeuchte. Zusätzlich wurde ein fest gebundenes Wasser auch für den Na^+-ausgetauschten Illit beobachtet. Dies deutete darauf hin, dass die austauschbaren Kationen des Illits in der gleichen Weise wie in den Smectitproben hydratisieren.

Besonderes Interesse galt der Unterscheidung von leicht gebundenen Wasser und Wasser, das in der Hydratationshülle des Zwischenschichtkations gebunden ist. Dabei wurden infrarotspektroskopische Messungen durchgeführt, um ein Modell auf molekularer Ebene zu erhalten und die Mechanismen von Wasserde- und -adsorption zu untersuchen.

Ziel der ersten IR-Studie war es, gekoppelte Prozesse der (De-) Hydratation und Veränderungen der 2:1 Schicht eines Na^+-ausgetauschten dioktaedrischen Smectits mittels *in-situ* IR-Spektroskopie zu untersuchen. Dabei wurde ein dünner Film von 200 nm einer reinen *trans-vacante,* dioktaedrische Smectitprobe mittels 'tethering by aggregation and growth' (T-BAG) auf einen Siliziumwafer aufgebracht. Dabei wurde ein heizbarer Probenhalter verwendet, auf den der beschichtete Siliziumwafer befestigt wurde und in einer Handschuhbox in reiner Stickstoffatmosphäre mittels IR-Spektroskopie untersucht wurde. Im Zuge des Dehydrationsversuches wurde eine Verschiebung der Deformationsbande von Wasser $\delta(H\text{-}O\text{-}H)$ zu niedrigen Wellenzahlen beobachtet. Diese Verschiebung wurde mit einer Erhöhung der Anziehung von basaler Silicatoberfläche korreliert. Diese Zunahme der Silicatoberflächen-Wasser-Anziehung mit zunehmender Temperatur und schließlich abnehmenden Wassergehalt wurde durch die gekoppelte Verschiebung des optischen (longitudinalen) Phononen Mode von SiO $(Si\text{-}O)^{LO}$ zu niedrigen Wellenzahl bestätigt. Die Interaction von Wassermolekül und basaler Silicatoberfläche hat zur Folge, dass im monohydratisierten Zustand Wassermoleküle in der Zwischenschicht stark polarisiert sind. Dementsprechend wurde eine niedrigere Wellenzahl von $\delta(H\text{-}O\text{-}H)$ bei 1628 cm^{-1} im Vergleich zu flüssigem Wasser mit 1644 cm^{-1} beobachtet. Weiterhin wurde ein dioktaedrischer Montmorillonit mit unterschiedlichen Wassergehalten mittels Dichtefunktionaltheorie berechnet. Die Modelle zeigten, dass die Kristallgitterabstände a_0 und b_0 mit Abnahme des Wassergehaltes kleiner werden. Dies zeigte, dass neben dem bekannten kristallinen Quellverhalten entlang [001] es ebenfalls zu geringen Änderungen in [100] und [010] im Zuge der Dehydration kommt. Die Änderung der Gitterabstände erklärten den damit verbundenen Shift von $(SiO)^{LO}$ zu kleineren

X

Wellenzahlen. Die Berechnungen der Modelle wurden von Dr. Peter Thissen durchgeführt.

In der ersten IR-Studie wurde der Mechanismus im Übergang von 1W zu 0W beobachtet. In einer weiteren IR-Studie wurde der Übergang von 2W zu 1W, sowie der Einfluss der Schichtladung und der oktaedrischen Zusammensetzung betrachtet. Dabei wurden die ausgewählten Materialien mittels einer *in-situ*-Messeinrichtung untersucht, die gleichzeitig FTIR-Spektren und die Aufnahme von Wasserdampf-Sorptionsisothermen ermöglichte. Weiterhin war das Ziel dieser Studie, Einflussfaktoren zur Größe der Hysterese in 2:1 Schichtsilicaten während der Desorption und Adsorption von Wasserdampf zu beschreiben. Während eine Hysterese über den gesamten isothermen Bereich der Smectite beobachtet wurde, zeigte die Isotherme der Vermiculitprobe nur eine Hysterese im Übergang von 0W zu 1W und 1W zu 2W. Es zeigte sich, dass die Hysterese eine Funktion der Schichtladungsverteilung, des erreichten Wassergehaltes und der Partikelgröße ist. Eine Erhöhung der Kantenanteile führte zu einer größeren Hysterese. Die Ergebnisse der FTIR Studie zeigten auch, dass der Übergang von 2W nach 1W mittels IR-Spektroskopie sichtbar ist. Die Verschiebung von δ(H-O-H) zu kleineren Wellenzahlen wurde durch die Schichtladung, Ladungsverteilung, oktaedrische Substitutionen und der Partikelgröße beeinflusst. Die experimentellen Ergebnisse wurden ebenfalls von DFT Simulationen (durchgeführt von Dr. Peter Thissen) unterstützt, mit denen die unterschiedlichen Wellenzahlen von δ(H-O-H) in Bezug auf die Oberflächenladungsdichte und der oktaedrischen Zusammensetzungen erklärt werden konnte.

List of abbreviations

0W	dehydrated state
1W	mono-hydrated state
2W	bi-hydrated state
3W	tri-hydrated state
a_0	lattice constant in [100] direction
$a_{S,BET}$	specific surface area according to the BET model
$a_{s,edge}$	specific edge surface area
$a_{s,basal}$	specific basal area
AFM	atomic force microscopy
ATR	attenuated total reflectance
b_0	lattice constant in [010] direction
BET	Brunauer-Emmett-Teller
c_0	lattice constant in [001] direction
CEC_P	permanent cation exchange capacity
CEC_T	total cation exchange capacity
Cu-trien	Cu^{2+}-triethylentetramine
cv	cis -vacant
CV	coefficient of variation
d	mean weighted equivalent diameter
$\delta(H\text{-}O\text{-}H)$	H-O-H bending vibration
$\delta(M^{x+}N^{y+}\text{-}OH)$	$M^{x+}N^{y+}$-OH bending vibration of OH groups of the octahedral sheet
δ^+	partial positive charge

d_{001}	basal spacing in [001] direction
DFT	density functional theory
di	dioctahedral
DSC	differential scanning calorimetry
DTA	differential thermal analysis
DTGS	deuterated-triglycine sulfate detector
DVS	dynamic vapor sorption
ε	dielectric constant
EDL	electrostatic double layer
EG	ethylene glycol
EGA	evolved gas analysis
eps	equivalent particle size
ESEM	environmental scanning electron microscopy
esd	equivalent sphere diameter
ξ	net negative charge per layer or formula unit
ξ_T	tetrahedral charge
FIR	far infrared
f.u.	formula unit
FTIR	fourier transform infrared spectroscopy
FWHM	full width at half-maximum
η_0	viscosity of water
g	gravity force
h	settling distance of the particles

ICP-OES	inductively coupled plasma – optical emission spectroscopy
ICTAC	International Confederation for Thermal Analysis and Calorimetry
IUPAC	International Union of Pure and Applied Chemistry
LB	Langmuir-Blodgett
$m_{0\ \%\ r.h.}$	dry mass of the sample related to the mass at the first 0.0% r.h. stage
Δm_{DHD}	mineralogical water content = w_{min}
MIR	mid infrared
MS	mass spectrometry
$v(O\text{-}H)_{H2O}$	O-H stretching vibration of water
$v(M^{x+}N^{y+}O\text{-}H)$	O-H stretching vibration of OH groups of the octahedral sheet
$v(Si\text{-}O)$	Si-O stretching vibration
n	layers per stack of d
NIR	near infrared
NLDFT	non-local density functional theory
O_a	tetrahedral apical oxygen atom
O_b	tetrahedral basal oxygen atom
$p_{tol.}$	pressure tolerance
ρ	density
ρ_0	density of water
r.h.	relative humidity
SSF	self-supported clay films
$Si\text{-}O^{LO}$	longitudinal optical Si-O phonon mode

STA	simultaneous thermal analysis
SAXS	small-angle X-ray scattering
T-BAG	tethering by aggregation and growth
$t_{tol.}$	time in tolerance
t_{EQ}	time to achieve equilibrium
TGA	thermogravimetry
TOT layer	tetrahedral-octahedral-tetrahedral layer
tv	trans -vacant
TEM	transmission electron microscopy
tri	trioctahedral
UV/VIS	ultraviolet–visible spectroscopy
vdW	von der Waals forces
w_{GT}	geotechnical water content
w_{min}	mineralogical water content = Δm_{DHD}
χ	electronegativity
XRD	X-ray diffraction
XRF	X-ray fluorescence

Mineral abbreviations according to Whitney & Evans (2010)

Table of contents

1 Introduction

1.1 Motivation

Our society aims for sustainable use of natural resources and conscientious land use. By far the most abundant natural resources are phyllosilicate-containing geomaterials (clays and soils) that are utilized as they occur in nature in various applications. These applications span from technical applications (e.g. in molding sands) and geotechnical applications (e.g. barriers for radioactive and toxic waste deposits or caprock for CO_2 storage) to geological processes (e.g. formation and storage of crude oil and quick clays), biogeochemical reactions (e.g. as prebiotic catalysts). Due to their water binding capability clays are also important in agriculture and flood management as well as climate modeling.

One of the most important type of clays are bentonites. Bentonites act as hydraulic sealing by swelling under hydration. Bentonites mainly consist of low-charged swellable clay minerals called smectites and other phases (minerals, liquids, organic matter and air). Smectites, the most heterogeneous phyllosilicates, are built of 2:1 layers. They do not only hydrate and swell but also act as cation exchanger and adsorber. After saturation the main transport mechanism for e.g. radionuclides is molecular diffusion along mineral surfaces and through pores. Saturation depends on available moisture and compaction of the bentonites, which determine the ratio between strongly bound water in hydration shells of interlayer cations and surface bound water together with pore water.

Thus, the understanding of the hydration of smectites is mandatory for understanding and controlling related processes and for monitoring of the hydration state in various applications.

For determination of water content in soils and clays several (geo-)physical methods such as time domain reflectometry or tensiometry are available. Geophysical methods are indirect approaches that require calibration for transformation of measured values such as complex dielectric permittivity or suction pressure into water content (Wagner et al., 2011). The most common method for calibration is static heating at 105 °C and determination of the gravimetric water content while geophysical methods are based

on volumetric water content. Thus, bulk density of the material additionally influences calibration functions. On the other hand dynamic heating methods show, that clays and soils still contain notable amounts of water after static heating at 105 °C (Kaden, 2012). This is due to the complexity of water binding mechanisms in smectites.

Smectites are characterized by a very small particle size and are regarded as natural nanoparticles. Small particle size results in a large specific surface area of up to 800 m²/g. In addition, swellable 2:1 layer silicates can bind a tremendous amount of water in hydration shells of interlayer cations. However, the water binding is strongly influenced by the structure of the 2:1 layer silicates (e.g. layer charge, charge density and surface properties).

Additionally, hysteresis of water suction and water content occurs when wetting and drying soils and clays. Both materials display different water suction pressures at the same water content depending on whether the system is on desorption or adsorption path. Similarly, soils and clays possess different gravimetric water contents when exposed to a certain relative humidity (r.h.) until weight equilibrium is reached. Plate-like particle shape of phyllosilicates and porosity seems to be important for hysteresis but no quantitative model exists so far. Therefore, the influence of all parameters on water bindings and dielectric properties has to be assessed first for reference phyllosilicate samples as a sound basis for calibration functions.

1.2 Objectives

The aim of this thesis was to discriminate water binding mechanisms in 2:1 layer silicates and how their structural intrinsic properties affect their hydration behavior using different methods in dependence of the smectite and vermiculite structure. To achieve this goal, the project pursued a series of interrelated activities.

Characterization of structural features of selected 2:1 layer silicates

Natural phyllosilicates and especially swellable 2:1 layer silicates are characterized by an intrinsic structural heterogeneity of the silicate layers and interlayer occupation. These heterogeneities within the material can lead to coexistence of different hydration states. Heterogeneity in the layer structure cannot be avoided but must be known in detail as layer charge determines the amount of interlayer cations that will hydrate. For characterization of the structure X-ray diffraction (XRD) analysis, chemical analysis, thermal analysis and Fourier Transform Infrared Spectroscopy (FTIR) will be applied. Several 2:1 layer silicates comprising smectites of different layer charge between 0.2 to 0.6 / formula unit (f.u.) and charge location (octahedral vs. tetrahedral charge), a vermiculite and a very fine grained illite sample will be studied.

Study of hydration by XRD, thermal analysis and vapor sorption

Heating at 105 °C will not dehydrate 2:1 layer silicates completely. Therefore, dynamic thermal analysis will be applied to determine the water content for adsorption-desorption isotherms after storing the samples at defined relative humidities (r.h.). XRD patterns are the basis for determining the respective hydration state as a function of r.h.. Results obtained by water adsorption will give a first general overview by mean of a qualitative and quantitative information of water ad- and desorption taken up by the 2:1 layer silicates.

Accompanied structural changes in 2:1 layer silicates during the release of interlayer water

The coupled processes of (de-)hydration and structural changes will be studied by *in-situ* transmission FTIR. Therefore, a sample preparation technique based on the Tethering by aggregation and growth (T-BAG) method will be extended to clay minerals to obtain a thin film of montmorillonite on a silicon wafer. Using a very thin

film, deviation of the Si-O phonon modes can be simultaneously study with the vibrational modes of water. The structural changes in the 2:1 layer of the montmorillonite during dehydration can be recognized from the shift of longitudinal optical Si-O phonon mode $((Si\text{-}O)^{LO})$.

In order to gain deeper understanding of the coupled processes of dehydration and Si-O phonon mode evolution, models with different water contents will be employed by state-of-the art calculations using density functional theory (DFT).

Analysis of hydration hysteresis

In the last part, the aim is to elucidate the hysteresis mechanism in 2:1 layer silicates during desorption and adsorption of water vapor. First, the shape of the selected materials will be determined using Environmental scanning electron microscopy (ESEM), XRD and gas adsorption analysis, which will give a detailed picture of the particle size with resulting edge site proportion. Then, the samples will be studied by *in-situ* coupling of FTIR and the gravimetrical determination of water vapor sorption isotherms and relate these experimental results to the intrinsic properties (e.g. layer charge, charge location, octahedral composition and particle size) of the 2:1 layer silicates being studied.

To support the experimental findings, DFT calculations will be employed to explain the different shifting behavior of the H-O-H bending vibration of water (δ(H-O-H)) related to the differences in surface charge density and octahedral compositions.

2 Structure of 2:1 layer silicates

2.1 The 2:1 layer silicates

The layered structure of 2:1 layer silicates consists of two tetrahedral (T) and one octahedral (O) sheet forming a layer. In the tetrahedral sheet each SiO_4 tetrahedron is linked to an adjacent tetrahedron by sharing three oxygen atoms (the basal oxygen atoms O_b) to form a hexagonal and pseudohexagonal ring, respectively, in the plane spanned by a_0 and b_0. The fourth tetrahedral apical oxygen atom (O_a) of all tetrahedra points to the same direction and connects tetrahedral and octahedron sheets (Figure 2.1). The octahedral part consists of [$Al(O_4OH_2$] or [$Mg(O_4OH_2)$)] octahedra and linked to neighboring octahedra by sharing edges. The octahedral sheet can be occupied by either divalent cations (trioctahedral) or trivalent cations (dioctahedral). In the 2:1 layer structure, the unit cell includes six octahedral and eight tetrahedral sites. If all octahedral sites are occupied by divalent cations, the structure is called trioctahedral (Figure 2.2 A). In a dioctahedral sheet only four of six octahedral sites are occupied by trivalent cations (Figure 2.2 B). Octahedral cations are frequently Al^{3+}, Fe^{3+}, Mg^{2+} or Fe^{2+}.

Isomorphic substitutions in the octahedral and in the tetrahedral sheets generate a negative layer charge. Exchangeable cations such as Na^+ in the interlayer space, between two TOT layers, compensate the charge to obtain electroneutrality. The layer charge per formula unit (f.u.), ξ, is the net negative charge per layer and expressed in a positive number. In case of dioctahedral pyrophyllite and trioctahedral talc no substitutions occur and the layer is electrically neutral. For true micas ξ is close to 1, while for brittle micas ξ is up to 2. In the latter case, the interlayer is occupied by divalent anhydrous cations. In true micas, the charge is commonly compensated by monovalent K^+ ions. A further subgroup of micas is defined as interlayer-deficient micas, if ξ is < 0.85 and ≥ 0.6 (Rieder et al., 1998). According to these authors, illite is used as a series name and defined as an interlayer-deficient mica. The most common 2:1 layer silicates are smectites and vermiculites, which are characterized by the presence of hydrated cations in the interlayer. ξ ranges from 0.6 and 0.9 for vermicuites and 0.2 to 0.6 for smectites (Table 2.1). The calculation of the structural formula from the chemical composition is commonly reported based on the half unit cell (UC) or f.u. and, hence, based on three octahedral sites of $O_{10}(OH)_2$ per FU. Here, the calculation

is based on the assumption of tetrahedral occupation by four cations ($^{IV}SI+^{IV}AI$) with a complete occupied octahedral sheet resulting in 22 negative charge per FU (Emmerich, 2013).
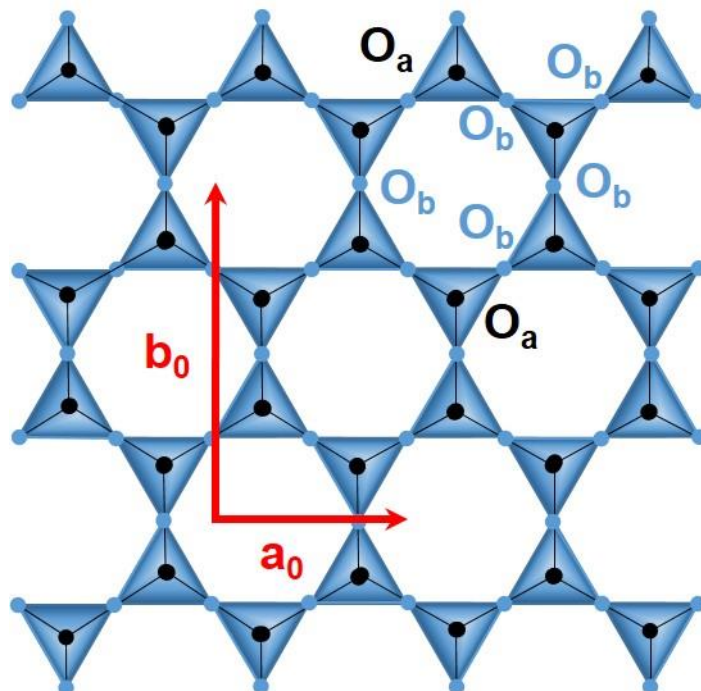
Figure 2.1 Tetrahedral sheet. a_0 and b_0 refer to unit cell parameters, respectively, O_a and O_b refer to apical and basal oxygen atoms.

A   **B**
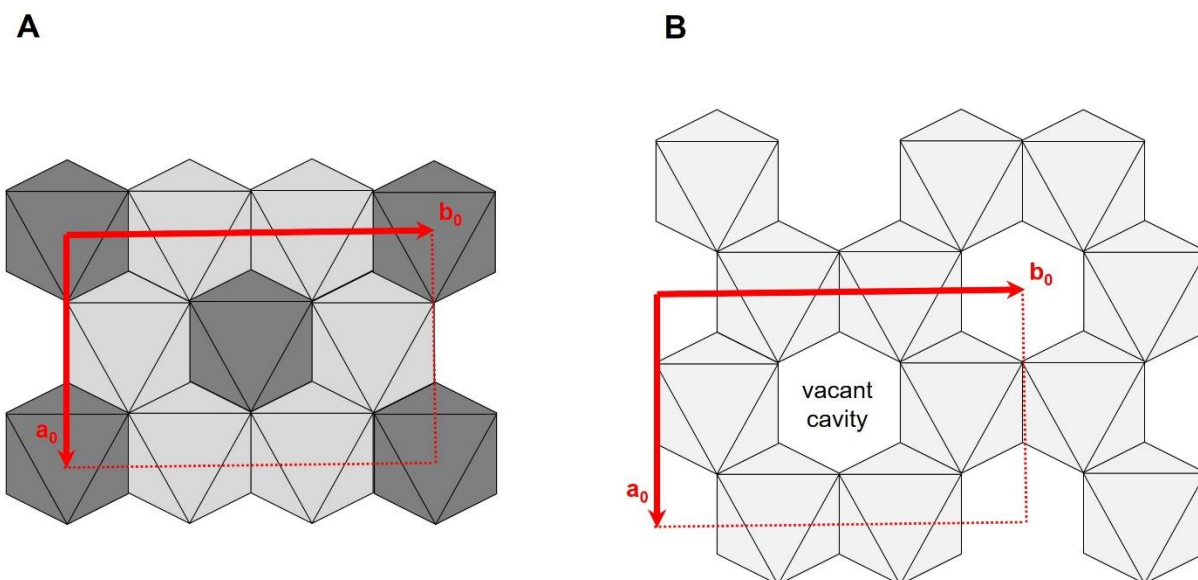
Figure 2.2 (A) Trioctahedral and (B) dioctahedral sheet. a_0 and b_0 refer to unit cell parameters.

Table 2.1 Classification and nomenclature of planar hydrous 2:1 layer silicates (without chlorites) including interlayer deficient micas, tri = trioctahedral, di = dioctahedral. According to (Bergaya and Lagaly, 2013; Brigatti and Guggenheim, 2002; Rieder et al., 1998).

Interlayer material	Charge per formula unit (ξ)	Group	Octahedral character	Species
None	$\xi \approx 0$	Talc-pyrophyllite	Tri	Talc
			Di	Pyrophyllite
Hydrated, exchangeable cations	$\xi \approx 0.2\text{-}0.6$	Smectite	Tri	Hectorite
			Di	Montmorillonite
Hydrated, exchangeable cations	$\xi \approx 0.6\text{-}0.9$	Vermiculite	Tri	trioctahedral vermiculite
			Di	drioctahedral vermiculite
Non-hydrated, monovalent cations	$\xi \approx 0.6\text{-}1.0$	True mica	Tri	Phlogopite, annite
			Di	Muscovite
Non-hydrated, divalent cations	$\xi \approx 1.8\text{-}2.0$	Brittle mica	Tri	Clintonite
			Di	Margarite
Non-hydrated, monovalent cations	$\xi \approx 0.6\text{-}0.85$	Interlayer deficient mica	Tri	Wonesite
			Di	Illite, glauconite

2.2   Smectites ($\xi \approx 0.2 - 0.6$)

Smectites are swellable 2:1 layer silicates with a negative layer charge between 0.2 and 0.6 per formula unit (f.u.). Isomorphic substitutions in the octahedral sheet (Al^{3+} substituted by Mg^{2+} and Fe^{3+}/Fe^{2+}) and in the tetrahedral sheet (Si^{4+} substituted by Al^{3+}) generate a negative layer charge. The charge-compensating counterions in the interlayer space of smectites are naturally Na^+, K^+, Ca^{2+} or Mg^{2+}. These cations are commonly hydrated and easily exchangeable. This property is known as cation exchange capacity (CEC). Due to different octahedral structure and different location of deficit charge (octahedral vs. tetrahedral) a huge structural variety exist (Emmerich, 2013; Wolters et al., 2009).

Table 2.2 Most common smectite end-members (according to Emmerich, 2013)

Name	Formula unit
Dioctahedral species	
Montmorillonite	$M^+_{x+y} (Si_4) [(Al^{3+})_{2-y} (Mg^{2+},R^{2+})_y] O_{10}(OH)_2$
Beidelite	$M^+_{x+y} [(Si_{4-x})(Al^{3+})_x] [(Al^{3+},R^{3+})_2] O_{10}(OH)_2$
Nontronite	$M^+_{x+y} [(Si_{4-x})(Al^{3+})_x] [(Fe^{3+},Al^{3+})_{2-y} (Fe^{2+},Mg^{2+})_y] O_{10}(OH)_2$
Trioctahedral species	
Hectorite	$M^+_{x+y} (Si_4) [(Mg^{2+})_{3-y} (Li^+)_y] O_{10}(OH)_2$
Saponite	$M^+_{x+y} [(Si_{4-x})(Al^{3+})_x] [(Mg^{2+})_3] O_{10}(OH)_2$
Sauconite	$M^+_{x+y} [(Si_{4-x})(Al^{3+})_x] [(Mg^{2+},Zn^{2+})_3] O_{10}(OH)_2$

The general formula for dioctahedral species is

$$M^{n+}_{(x+y)/n} [Si_{4-x}(Al,T^{3+})_x] [(Al,Fe^{3+},R^{3+})_{2-y} (Mg,Fe^{2+},R^{2+})_y] O_{10}(OH)_2$$
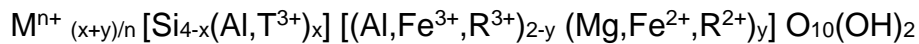
and that for trioctahedral smectites is

$$M^{n+}_{\chi/n} [Si_{4-x}(Al,T^{3+})_x] [(Mg,Fe^{2+})_{3-(y+z+u)} (R^{3+})_y (R^+)_z (X)_u] O_{10}(OH)_2$$
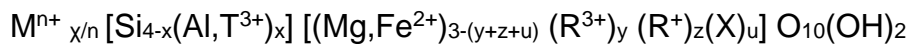
with $\chi = x - y + z + 2u$. R^{3+}, R^{2+} and R^+ represent the common mono-, di- and trivalent octahedral cations and M^{n+} symbolize the interlayer specie. T^{3+} (mainly Fe^{3+}) represents cations that substitute tetrahedral cations and X stands for non-occupied (vacant) positions (Emmerich, 2013).

The layer charge, the charge location and the kind of interlayer cations strongly influence the chemical and physical properties of the smectites (Emmerich, 2013). Dioctahedral smectites with two of three occupied octahedral positions show distinct differences in the structure of their octahedral sheet (Figure 2.3). With respect to the spatial arrangement of the OH groups of vacant positions, *trans-* (*tv*) and *cis*-vacant (*cv*) varieties were distinguished (Tsipursky and Drits, 1984). To determine the ratio of *tv* and *cv* layers dynamic thermal analysis is used (Wolters and Emmerich, 2007). *Cv-vacant* dioctahedral smectites dehydroxylate between 650 and 700 °C and *tv-vacant* varieties between 500 and 550 °C. These structural features in dioctahedral smectites led to a new classification of the montmorillonite-beidelite series, which are the most common dioctahedral smectites (Emmerich et al., 2009).
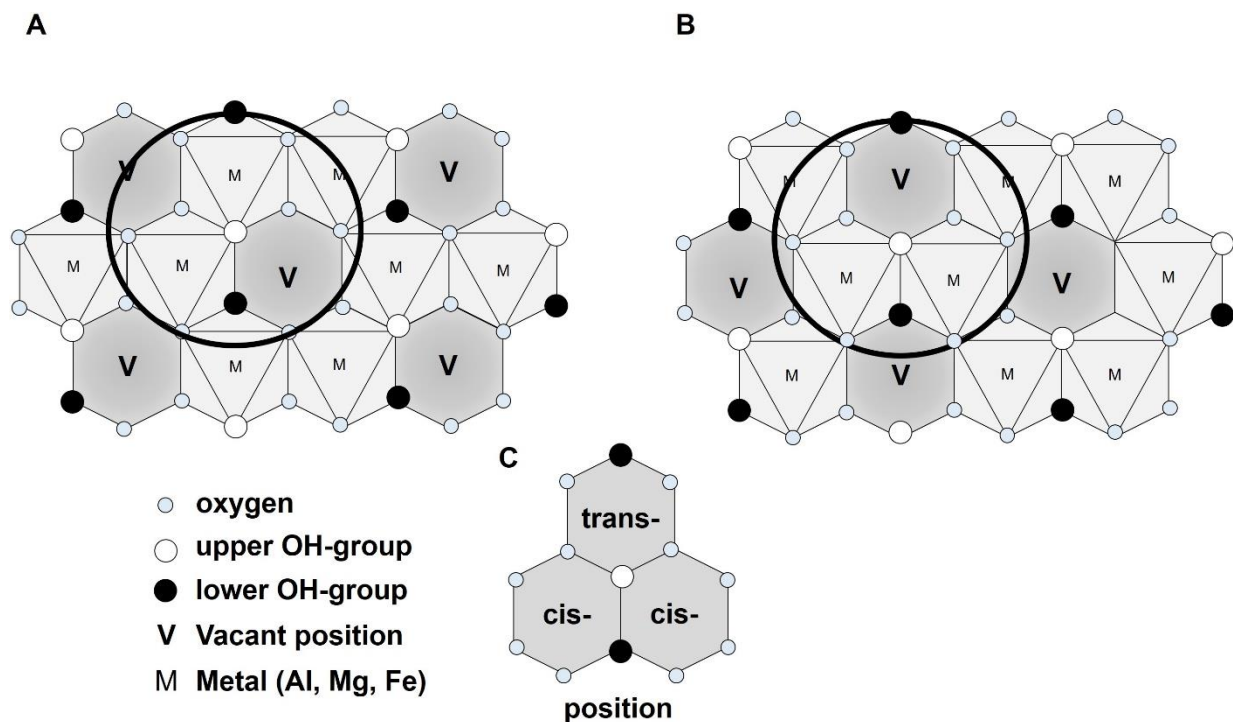
Figure 2.3 Projection of the octahedral sheet of a dioctahedral 2:1 clay mineral perpendicular to the c-axis. (A) The *cis*-vacant (*cv*) variety, (B) The *trans*-vacant (*tv*) variety. (C) *Trans* (M1)- and *cis* (M2)-positions with respect to the location of the hydroxyl groups. Modified from (Wolters and Emmerich, 2007).

The structure and the morphological character determine the smectite properties. pH dependent edge sites play a significantly role of the stability and reactivity of the smectite (Delavernhe et al., 2015). A variable charge is lying at the edge of the layers associated with amphoteric sites such as Si-OH and Al-OH (Sposito, 1984). Based on the theoretical studies on edge site properties of White and Zelazny (1988), Tournassat

et al. (2003) correlated edge site properties with the chemical character of a Na-saturated dioctahedral smectites (Tournassat et al., 2003; White and Zelazny, 1988). Delavernhe et al. (2015) used that approach and showed in a comprehensive characterization that edge site properties also differ within four representative dioctahedral smectites (Delavernhe et al., 2015). The reason for this was primarily the layer dimension, which determines edge site properties.

Beside the complexity in their chemical composition, smectites often exhibit a broad particle size distribution. Together with the mineralogical composition, the particle size distribution determines their engineering properties (Harvey and Lagaly, 2013). Smectites are naturally fine-grained with an equivalent particle size (eps) of mainly < 2 µm. They consist of plate-like particles and have a seemingly cloudy morphology of aggregates. However, natural smectite particles are not equal (monodisperse) in size but exhibit different types of distributions (bi-, uni and multimodal). Microscopic investigations such transmission electron microscopy (TEM), scanning electron microscopy (SEM) or atomic force microscopy (AFM) are useful to determine directly the shape and geometric dimensions within the inherent instrumental and preparation uncertainties (Lagaly and Dékány, 2013).

Together with their chemical and morphological heterogeneity smectites exhibit a turbostratic, disordered arrangement of layers. In a turbostratically disordered phase, the layers are randomly rotated around the c-axis. As a consequence, the *hk0* reflections are displayed as extremely asymmetric peaks and the *hkl* reflections with l ≠ 0 and h or k ≠ 0 are lacking in XRD patterns. Details about smectite identification by XRD will be given in chapter 5.

2.3   Vermiculites (ξ ≈ 0.6 – 0.9)

As an industrial commodity the term 'vermiculite' is used to describe any commercially exploited deposits of micaceous minerals which can be exfoliated when heated rapidly to high temperatures (Emmerich et al., 2017). The exfoliation of 'vermiculite' was well known but poorly understood till the detailed studies of Hillier et al. (2013) elucidated its mechanism. Exfoliation is explained as a volume expansion with individual platelet-shaped particles expanding in an accordion-like fashion to up to 20-30 times their original volume. Paradoxically, pure vermiculite does not exhibit the property of exfoliation (Tsipursky and Drits, 1984). However, the name 'vermiculite' originates from its accordion-like, vermiform appearance in its exfoliated form. Despite their vague definition in commercial commodity sense, vermiculites are precisely mineralogical defined. Such as smectites, vermiculites are swellable 2:1 layer silicates, but carrying a higher net negative charge between 0.6 and 0.9 per f.u. (Besson et al., 1974; de la Calle and Suquet, 1988). In vermiculites, the negative charge is mainly generated in the tetrahedral sheet due to exchange of Si^{4+} by Al^{3+}. Vermiculites are commonly Mg^{2+}-rich, trioctahedral and mainly formed from the alteration of biotites and chlorites. Only few dioctahedral species are reported in the literature (Stepkowska et al., 2004). In contrast to smectites, vermiculite can have a particle size > 20 µm and, consequently, vermiculite particles are often large enough for detailed structural studies (Ferrage et al., 2015).

As well as in smectites, the formation of discrete water layers in the interlayer and the layer stacking orders in vermiculite depend on the type of interlayer cation and the r.h. (Beyer and Graf von Reichenbach, 2002). When the transition from one layer to the next can be obtained by rather two or more different translations along the b-axis, the term semi-ordered is used for the structure of vermiculite. The semi-ordered structure of vermiculite results from a translation shift between adjacent 2:1 layers, which is always –a/3 along [100] and alternates ±b/3 along [010] (Argüelles et al., 2010). Two types of layers, A and B, were proposed for vermiculites (de la Calle and Suquet, 1988). A- and B-layers differs in the position of the hydrated interlayer cation within the interlayer. In both cases, the position of the exchangeable cation is located above the base of the SiO_4 tetrahedron. In the A-layer, the hydrated cation occupies the *m1* position and *m2* position in the B-layer. For more detailed information, the reader is referred to Argüelles et al. 2010, and references herein.

Comparing the layer stacking sequences for a given interlayer cation and a given r.h. of a low-charged vermiculite with those of a high-charged trioctahedral smectite, e.g. saponite, there is no difference (De la Calle et al., 1988). According to these authors, there is no reason that would justify an abrupt division of trioctahedral smectites with tetrahedral substitutions at a layer charge of 0.6 per f.u., which is the upper limit for the group of smectites.

2.4   Illites ($\xi \approx 0.6 - 0.9$)

Illite is described as an interlayer-deficient mica with a huge variety of chemical composition (Brigatti and Guggenheim, 2002). Illites are dioctahedral 2:1 layer silicates with a non-expandable interlayer found in soils and sedimentary rocks. The layer charge ranges from 0.6 to 0.9 per f.u. and its interlayer cation is commonly K^+. The structure of illite is similar to those of dioctahedral muscovite, but differs in the interlayer with H_3O^+ replacing K^+ (Nieto et al., 2010). The charge in illite is commonly neutralized by K^+ ions, but the interlayer composition may also include water molecules, which was confirmed by structural refinements for illite-1M (Gualtieri et al., 2008). The term illite-1M is related to one of the possible polytypism of illite (Figure 2.4). Polytypism is commonly found in illites, which is a special form of polymorphism and defined in (Bailey et al., 1977; Guinier et al., 1984).
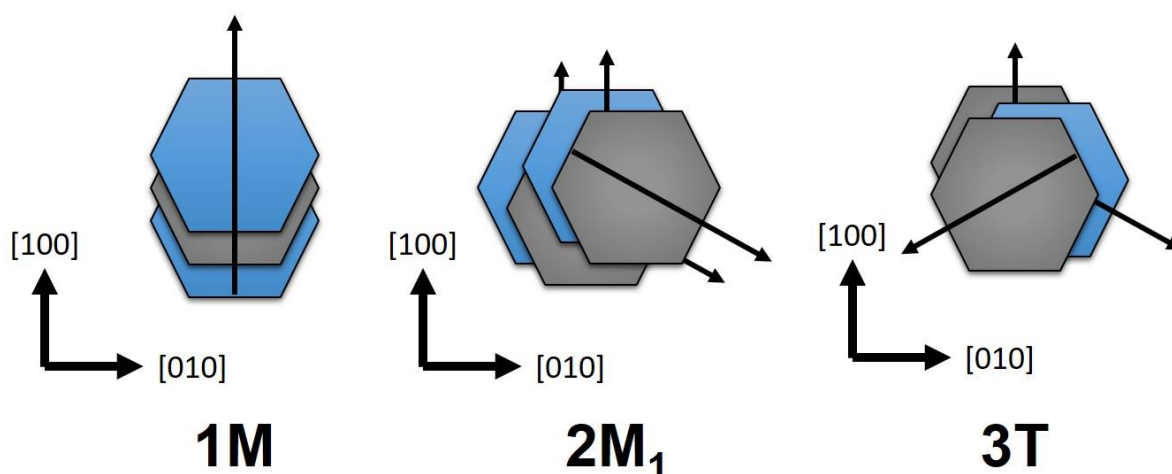
Figure 2.4 Viewed normal to the (001) plane the (A) 1M stacking polytype, (B) ± 120 ° rotations producing the 2M₁ polytype and (C) successive 120 ° rotations producing the 3T polytype. According to Moore and Reynolds Jr. (1997).

The polytypes (Figure 2.5) for illites found in nature are 1M (common in sandstones), $2M_1$ (detrital in shales; authigenic in low grade metamorphic rocks), $1M_d$ (diagenetic in shales and bentonites) and 3T (Grathoff and Moore, 1996), but also co-existing of different polytypes were reported in the literature (Zöller and Brockamp, 1997).

A large variety of mixed-layered clay minerals exist, where illite/smectite are the most common mixed-layer minerals. These minerals are even more common than discrete illite or discrete smectites (Moore and Reynolds Jr., 1997). The identification of these mixed-layer clay minerals is extensively described in (Srodon, 1984).

In contrast to smectites, the occupancy of the octahedral sheet can be derived from XRD patterns (Drits, 2003; Drits et al., 1993). These authors established a statistical relationship between the interlayer shift of two adjacent illite layers and the *cis-* and *trans-*vacant sites in the octahedral sheet. Thereby, the displacements along the [100] direction is larger for *trans-*vacant illites and smaller for *cis-*vacant illite as the theoretical value of 1/3 of (100).

3 Hydration of 2:1 layer silicates

Since the motivation of the current thesis is to investigate water in hydration shells of interlayer cations, excess water in interlayers and water bound to silicate surface as well as in pores of homoionic saturated smectites in dependence of the lamellar structure of 2:1 layer silicates, an interdisciplinary topic of clay mineralogy and material science is discussed.

3.1 Concepts of bulk and bound water

Bulk water

Water is a highly reactive substance. The decisive property is the polar character of the O-H bonds in a water molecule. The reason for their polar character is the difference in electronegativity[1] of the oxygen atom ($\chi_O \approx 3.44$) and the hydrogen atom ($\chi_H \approx 2.2$) leading to a partial charging for the hydrogen bonding of water molecules (Huheey, 1983). As a result, the oxygen atoms act as an H-bond acceptor and the H atoms act as H-bond donor with their partial positive charge (designated as δ^+, Figure 3.1). H_2O is a neutral molecule and, hence, the partial charge on oxygen must exactly balance that on the two hydrogen atoms. One of the most important facts for H-bonds is that they exhibit linearity and a direction (Figure 3.1). In this case, linearity means that the connected two oxygen atoms lie on the same line and the corresponding bond angle is 180 ° in the smallest water cluster, called water dimer (Feyereisen et al., 1996). As an isolated water molecule (gaseous phase), the angle between the two protons is 104.5 ° and the O-H bond length is 0.9584 Å (Benedict et al., 1956). In liquid, the bond angles for H-O-H were found to range between 104.52 and 109.5 ° with O-H bond length between 0.957 and 1.0 Å (Stern et al., 2001).

---

[1] Electronegativity, symbol χ, is defined as the tendency of an atom to attract electrons to itself. The values for χ_H and χ_O are refered to the dimensionless Pauling units Schoonheydt, R.A. and Johnston, C.T. (2013) Chapter 5 - Surface and Interface Chemistry of Clay Minerals, in: Faïza, B., Gerhard, L. (Eds.), Developments in Clay Science. Elsevier, pp. 139-172.
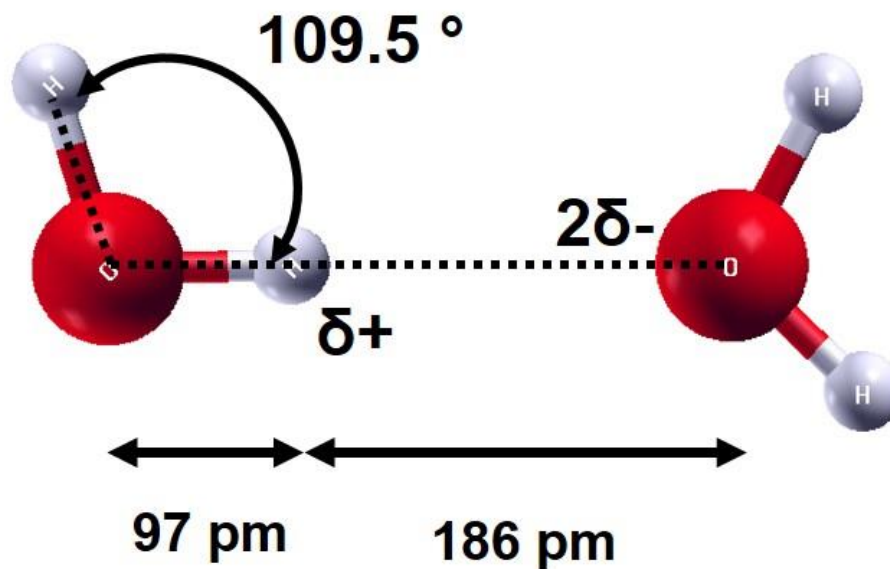
Figure 3.1 Characteristics of two water molecules associated through a hydrogen bond. δ^+ and $2\delta^-$ represent the partial positive and negative charges on the proton and oxygen.

The structure of bulk water is highly dynamic and according to Eisenberg and Kauzmann (1969) water has instanteaneous (called I-structure), vibrational (V-structure) and diffusional (D-structure) structures corresponding to different time domains of observation. The I-structure is the result of random vibrational motions within a lifetime of an electronic excitation ($< 10^{-15}$ s) and was investigated by methods such as the X-ray absorption spectroscopy (Head-Gordon and Johnson, 2006; Nilsson and Pettersson, 2011; Wernet et al., 2004). However, the determination on the instantaneous structuring of water is behind the scope of thesis. The V-structure of water include only the effects of vibrational motions and can be determined by methods such as the infrared spectroscopy (chapter 4). Averaging the vibrational motions in a short time scale (10^{-12} and 10^{-15} s) this structure would lead to a snapshot of a tetrahedral arrangement of H_2O molecules. Here, the term time scales refer to the meaning of how long a water molecule exist in a given arrangement. In this sense, on a larger time scale (10^{-4} to $\approx 10^4$ s) the D-structure can be obtained. This structure will be more ordered since it comprises only the most probable molecular configurations (Sposito and Prost, 1982). Accordingly, it is of utmost importance to keep this feature in mind when discussing the experimental methods used to study the structural arrangement of water. The specific time scale of each used method will be shown in the following chapters.

The properties of water have been investigated exhaustively and a large number of concepts exist for bulk water definitions (Sposito, 1984; Sposito and Prost, 1982). Here, the term bulk water or bulk-like water describes a kind of water, which has the character of a water cluster at ambient temperature and pressure. This means that all molecules of water interact with each another via hydrogen bonds. These molecules move unhindered and constantly in relation to each other. Among the most common water phases, liquid water, falls under the concept of bulk water. To a certain degree, the gaseous phase of water (water vapor) has also the characteristics of bulk water, however, it has a considerable different character related to its dielectric character (chapter 4).

'Bound water' in solids

Depending on the community, the concept of 'bound water' is used in different ways and has multiple definitions. In food science, bound water is defined as water that does not freeze and has non-solvent properties (Caurie, 2011). In the dictionary of geotechnical engineering bound water is defined as "(a) water that is a portion of a system such as tissues or soil and does not form ice crystals until the materials temperature is lowered to about -20 °C. (b) Water held strongly on the surface or in the interior of colloidal particles" (Herrmann and Bucksch, 2014). In soil science, bound water is still difficult to quantify and it is often neglected or barely estimated in practical applications (Wagner et al., 2011). In any case, bound water is defined in terms of the way how it is measured. Indeed, bound water has a different character than bulk water and the water molecules are bound that they cannot be easily removed.

Thus, this approach suggests that depending on the issue an appropriate measurement method must be selected to meet specific statements on the interaction of water with any kind of surfaces (Johnston, 2010). Here, the interaction of water and 2:1 layer silicates was investigated. Thereby two significant processes were considered: (a) the ion hydration and (b) the interaction of water and solid surfaces. In any case, the term 'bound water' is related to water molecules, which are in close proximity of a solid interface or of an ion, which possesses an unbalanced charge.

'Bound water' in liquid

Introducing a charged ion into pure liquid water, the structure of bulk water is perturbed. Water molecules, which are in close proximity to the charged ion will become ordered and form a shell around the ion. In case of a cation, the partially negative oxygen atom of the water molecules will be attracted to and pointing toward the cation, while the hydrogen atoms will be repelled and pointing outward (Figure 3.2).
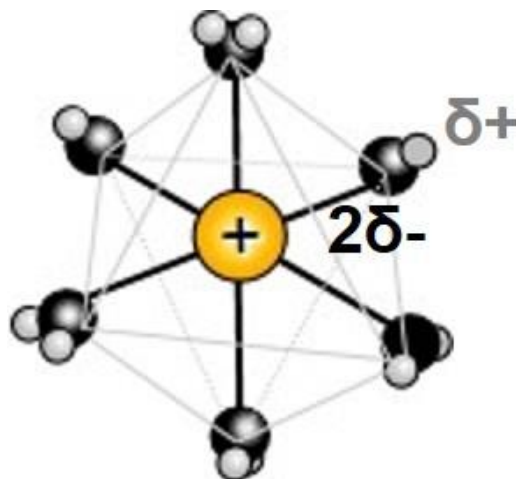
Figure 3.2 Illustration of a hydration sphere of a cation in octahedral coordination. δ^+ and $2\delta^-$ represent the partial positive and negative charges on the proton and oxygen.

In this sense, water molecules can bind to metal ions through ion-dipole bonds of mainly electrostatic character. The process is called hydration reaction and always strongly exothermic. This reaction is defined as the transfer of an ion from the gaseous phase to aqueous phase:

$$M^{n+}(g) + nH_2O(l) \rightarrow [M(H_2O)_n]^{n+}(aq)$$
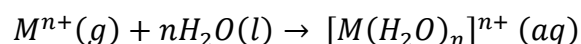
Whereby the heat of hydration increase with increasing charge density of the ion. The hydrated metal ions exhibit different configurations depending on the size and electronic properties of the metal ion (Persson, 2010). The structural basic models for hydrated metal ions are those with a high symmetry: for four-coordinated metal ion the tetrahedron and for six-coordinated the octahedron (Figure 3.2). For higher coordinated metal ions square antiprismatic and tricapped trigonal prismatic configurations are expected. A comprehensive overview of the structures of hydrated metal ions is given in Persson (2010).

3.2   Water binding in 2:1 layer silicates

A voluminous literature exists on the interactions of H_2O with 2:1 layer silicates using a broad range of different experimental methods (Ferrage, 2016; Güven, 1992; Iwata et al., 1995; Schoonheydt and Johnston, 2013; Sposito, 1984; Sposito and Prost, 1982). 2:1 layer silicates contain water in several forms. Water can be hold in interparticle or interaggregate space, so-called pore water, and in the interlayer forming a hydration shell with the interlayer cation and interacting with the basal surface. The more weakly bound pore- or interparticle water can already be released by drying under ambient conditions and have a similar character as bulk-like water (Sposito and Prost, 1982). The interlayer water has a significantly different character as bulk-like water. Together with these water types, an electrostatic double layer (EDL) water forms the transition zone from the mineral surface to free porewater (Bourg et al., 2003; Bradbury and Baeyens, 2003; Kozaki et al., 2008; Tournassat and Appelo, 2011). According to these authors, this EDL contains water, cations and anions, where an excess of charge-compensating cations neutralize the remaining charge at the outer surface of the particles.

The attraction of the EDL at mineral-water interfaces of clay mineral surfaces has been investigated on an atomic scale and led to detailed insights into how water reacts with those surfaces (Emmerich et al., 2015). They showed that the dielectric constant of water, or relative dielectric permitivity[2], decreases in function of the number of H_2O molecules. They determined to be $\varepsilon_{W1} \approx \varepsilon_{W2} \approx \varepsilon_{W3} = 22$ and, accordingly, lower than that of bulk water at room temperature ($\varepsilon_W = 80$). These results reflect the ability of water molecules to reorient and, consequently, influence chemical reactions near interfaces. This showed that the structure and physical properties of water near mineral surfaces can be substantially different from those of bulk water, that surfaces can perturb the fluid structure and properties up to several molecular diameters from the surface, and that these differences can be key to understanding mineral surface chemistry (Bonaccorsi et al., 2004; Kalinichev and Kirkpatrick, 2002; Korb et al., 2007; Pellenq et al., 2008; Richardson, 2004). A recent study on the molecular origin of a sharp high-frequency IR band (chapter 4.1.1) showed that such interfacial H_2O

---

[2] The dielectric constant is also known as relative permittivity and indicates how easily a material can become polarized by imposition of an electric field on an insulator. (1998) IEEE Standard Definitions of Terms for Radio Wave Propagation. IEEE Std 211-1997, i.

molecules exist in in the interlayer of 2:1 layer silicates and have even bidentate and monodentate[3] orientation with respect to the solid surface (Szczerba et al., 2016).

Interlayer water is strongly influenced by the structure of the 2:1 layer silicates (e.g. layer charge, charge location), hydration properties of interlayer cations and particle size distribution with resulting surface area. In addition, the edge sorption sites play a key role for the water reactivity of the hydrous layer silicates, although the edge surface area represents only 1-3 % of the total surface area (Tournassat et al., 2003) and its contribution is up to 10 % of the CEC (Delavernhe et al., 2015). These sorption sites depend on the pH value by means of protonated or deprotonated edge sites. In case of deprotonated edge sites, cations can be bound on these surfaces and may form a hydration shell. Since the selected 2:1 layer silicates lay in the pH range of 7-9, the edge site reactivity for water may play a significant role for the proportions of the different water types.

In sum, probing the water distribution in 2:1 layer silicates addresses mainly the issue of length scales (Johnston, 2010). The smallest length scale is that of hydrogen bonds, which is defined on the basis of their bond length (< 0.35 nm). The next larger scale is assigned to the inner crystalline swelling, where smectites and vermiculites expand in a stepwise fashion. The next larger scale of the multi-scale organization of highly porous smectite is the crystallite aggregate scale (2-200 nm). The largest scale is the scale of the clay particles themselves ('macro-aggregate scale' with 0.2 μm – 1.5 mm).

In these described interactions with associated length scales, there are two basic processes to consider. The first one is called crystalline swelling with d-spacings between 10 and 22 Å, which will be explained in the following. The second one is called osmotic swelling and occurs beyond d-spacings of 22 Å with diffuse double layers. Note, the last one preferentially occurs in case of smectites saturated with interlayer cations such as Na^+ and Li^+ (Lagaly and Dékány, 2013).

---

[3] Denticity is related to the number of donor groups in a single ligand that bind to central atom in a coordination complex Zelewsky, A.v. (1996) Stereochemistry of Coordination Compounds. John Wiley, Chichester.

Crystalline swelling

At low water contents, the crystalline swelling of smectites is a stepwise expansion of the layer-to-layer distance leading to the well-known 1W, 2W and 3W hydration states with increasing basal spacings (d_{00l}) that can be observed by XRD (Ferrage, 2016; Ferrage et al., 2011; Glaeser et al., 1967). In addition to the dehydrated state (0W, layer thickness ≈ 9.6-10.7 Å), these discrete hydration states are known as mono-hydrated (1W, layer thickness ≈ 11.6-12.9 Å), bi-hydrated (2W, layer thickness ≈ 14.9-15.7 Å) and tri-hydrated (3W, layer thickness ≈ 18.0-19.0 Å) (Figure 3.3). The latter is being less common (Ferrage, 2016). Many studies have recognized that these hydration states usually coexist in smectites, even under controlled conditions (Ferrage et al., 2011). Using XRD, such a coexistence is shown by the irrationally of the 00l reflections as well as by peak profile asymmetry at the transition between two hydration states. To quantify the amount of different layer types with different hydration states as a function of r.h., XRD profile modelling procedures were developed and extensively described in Ferrage et al. (2016).
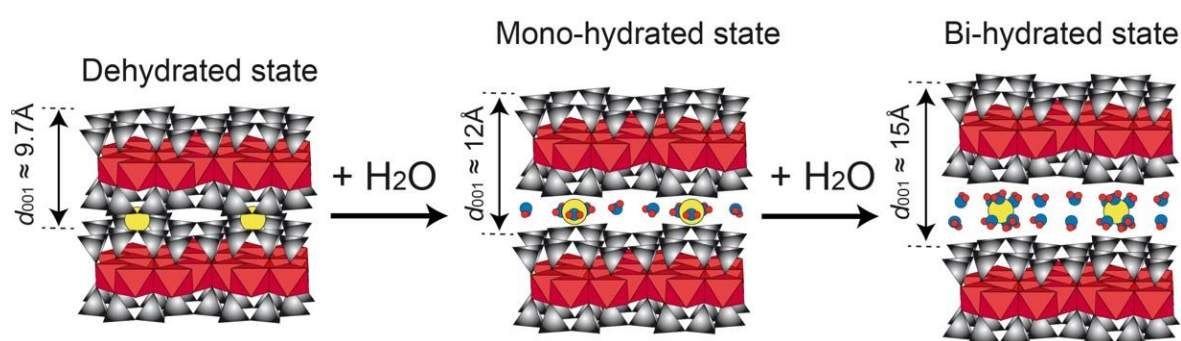
Figure 3.3 Schematic representation of crystalline swelling model and ranges of layer-to-layer distances (d_{001}). According to Ferrage, 2016.

The effect of layer charge on the interlayer water arrangement in natural dioctahedral smectites (Ferrage et al., 2007) and in synthetic tetrahedral charged trioctahedral smectites (saponites) (Dazas et al., 2015; Ferrage et al., 2010a) has also been studied using XRD profile modelling. From the relative proportions of hydration states, they demonstrated the influence of layer charge. They showed that smectite layer-to-layer distance decrease with increasing layer charge because of the enhanced cation-layer electrostatic attraction and the transition from 2W to 1W state shifts to lower H_2O / Na^+ during dehydration. However, questions regarding the orientation of interlayer water molecules cannot be answered by such structural studies (Ferrage et al., 2011).

Vermiculites have been the subject of several hydration studies since this group of minerals exhibits ordered stacking sequences of layers and, hence, eases the structural characterization of the interlayer configuration as compared to smectite (de la Calle and Suquet, 1988). As a result, most of the structural determination of 2W interlayer water arrangement were performed on vermiculite. These structural studies have led to different configurations for the interlayer water in 2W state. Figure 3.4 gives a schematic description of the different interlayer water arrangements proposed in the literature for vermiculite and smectite in 2W state.
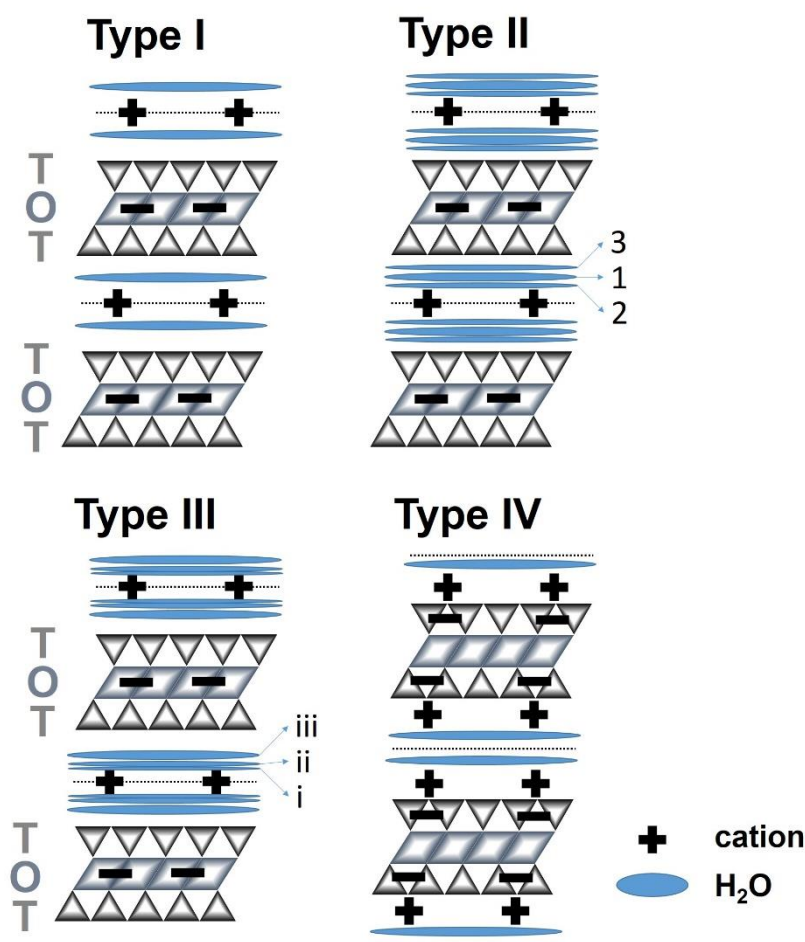
Figure 3.4 Schematic description of the different interlayer water arrangements proposed in the literature for 2W state. O and T refer to the octahedral and tetrahedral sheets of the 2:1 layer, respectively. (adopted and extended from Ferrage et al. 2005).

Type I: In 2W state interlayer cations are located in the mid-plane of the interlayer with one sheet of H_2O molecules on each side of this plane. The structure of the interlayer hydrated Na^+ cations in bi-hydrated state is proposed as a chain-like arrangement of $Na(H_2O)_6$ octahedra oriented along [100], sharing two oxygen atoms each (Beyer and

Graf von Reichenbach, 2002). In addition to the octahedrally coordinated Na^+, additional H_2O molecules are located on the same plane as the six cation-bound H_2O molecules. The same interlayer water arrangement was proposed for Mg^{2+}-saturated vermiculite (Cadene et al., 2005).

Type II: Slade et al. (1985) proposed a further arrangement of interlayer water in Ca^{2+}-saturated vermiculite and displayed as Type II in Figure 3.4. According to their model, two different coordinations were reported for Ca^{2+}. One Ca^{2+} exhibits a cubic coordination and two of three are octahedrally (six-fold) coordinated (the same as in Type 1). This dual coordination leads to two further discrete planes of water molecules (Figure 3.4, Type II plane 2 and 3) in addition to the type I arrangement. This arrangement of water molecules was also proposed for Na^+-saturated vermiculites (Slade et al., 1985).

Type III: The third type is the 2W smectite model proposed by Moore and Reynolds (1997). However, this model does not allow the description of experimental XRD patterns and was questioned by Ferrage et al. (2005a). The reason was that for smectites, the coexistence of different hydration states leads to unrealistic values to satisfactorily reproduce experimental XRD date, when using the proposed model (Ferrage et al., 2005a; Moore and Reynolds Jr., 1997). Moore and Reynolds (1997) suggested a 2W smectite model that contained three sets of planes of water molecules in the interlayer (Figure 3.4, Type III). Ferrage et al. (2005a) demonstrated a new distribution of interlayer water in bi-hydrated smectite. Their further refining for the interlayer structure of bi-hydrated smectite showed that the interlayer cations are located in the mid-plane of the interlayer, whereas H_2O molecules are scattered about two main positions according to Gaussian-shaped distributions (Ferrage et al., 2005a). A recently published work of Ferrage (2016) gives a detailed review of the methodology of combining XRD data and theoretical structural refinements (Ferrage, 2016).

Type IV: In case of Na^+-saturated beidelite with solely tetrahedral charges, Ben Brahim et al. (1983) proposed an arrangement of water molecules in the interlayer, where Na^+ cations are intended in the ditrigonal cavities of the 2:1 layers. As a result, the coordinated water molecules form 'inner-sphere' complexes with the monovalent cation (Figure 3.5 B).

'Inner-sphere' and 'outer-sphere' complexes

For octahedral substituted smectites, the majority of interlayer Na^+ cations are located in the mid-plane and mainly form 'outer-sphere' complexes with the 2:1 layer surface (Type I – III), whereas the formation of 'inner-sphere' complexes being favored by tetrahedral substitutions (Type IV). In the former case, the interlayer cation is completely surrounded by H_2O molecules, whereas in inner sphere complexes, the cation directly interact with the internal surface on the one side and to a number of H_2O molecules on the other side (Skipper et al., 1995). Inner-sphere complexes, such as one illustrated with a K^+ cation in Figure 3.5 C, are more frequent (Sposito, 1984). In case of K^+ as interlayer cation, interlayer complexes tend to build inner-sphere complexes in the interlayer space and, accordingly, acting as a swelling inhibitor (Boek et al., 1995b; Chang et al., 1995).
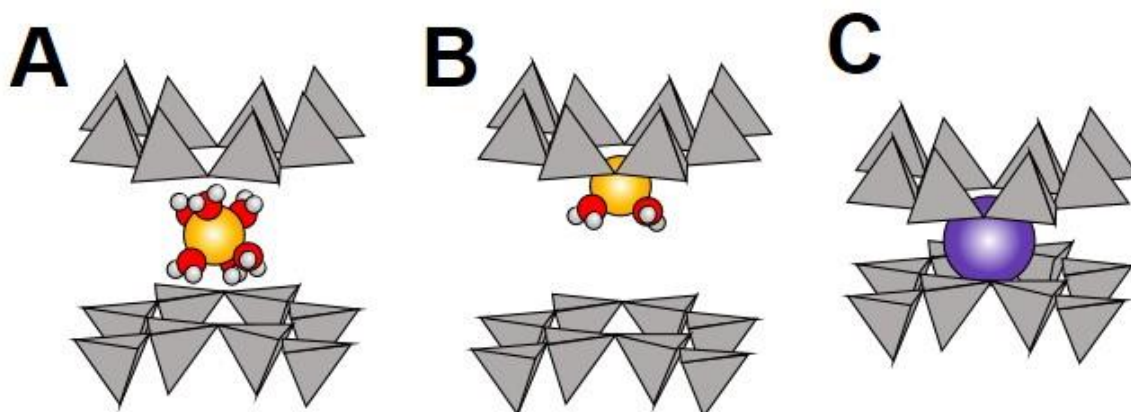
Figure 3.5 Illustration of (A) 'outer-sphere' complex with $Na(H_2O)_6$ and (B) 'inner sphere' complex $Na(H_2O)_2$ in the interlayer of a Na^+-saturated 2:1 layer silicate. (C) represents a anhydrous potassium often also called 'inner-sphere' complex . Yellow spheres represent Na, red spheres represent O and white spheres represent H. K is represented as a purple sphere.

Mechanism of crystalline swelling and spatial arrangement of adsorbed H_2O

The crystalline swelling of 2:1 layer silicates is controlled by the layer charge density and the hydration properties of the exchangeable cations (Bérend et al., 1995; Cases et al., 1992; 1997; Sato et al., 1992). This reversible swelling mechanism is induced by hydration of the exchangeable and charge-compensating counterions in the interlayer of swellable 2:1 layer silicates. IR spectroscopic studies of smectite hydration (Poinsignon et al., 1978; Prost, 1975) suggested that the first stage of water adsorption is the solvation of the exchangeable cations, which was confirmed by DFT calculations (Emmerich et al., 2015). After the solvation of the cations, water starts to reorient with its environment by forming hydrogen bonds. In 2W state water molecules form an octahedral complex with 6 water molecules surrounding the Na-ion (Emmerich et al., 2015; Ferrage, 2016). Thereby, a part of the H_2O molecules forms a hydration shells around the interlayer cations while further H_2O molecules fill the space between them. This general arrangement of water molecules was also reported by experimental studies on smectites (Johnston et al., 1992) and Na^+-saturated vermiculite (Swenson et al., 2001).

Beside the complexity of water bindings in the interlayer of hydrous 2:1 layer silicates, the proportions of the different water types depend on the size and shape of the smectites and vermiculites particles. Whereas water sorption in the interlayer is related to the permanent charge generated by the structure, edge sorption mechanism is related to acid-base properties of the edges (Delavernhe et al., 2015). Due to non-exchangeable or non-accessible interlayer cations and exchangeable cations at the edges, water content correlates more strongly with the exchangeable cations (measured as CEC) than with layer charge (Kaufhold, 2006; Kaufhold et al., 2011). This correlation is even more pronounced for small particles with an increased contribution from edge sites to CEC (Emmerich, 2010).

To summarise, the main forces affecting the hydration of the interlayer cation are the hydration energy of the interlayer cation, polarization of water molecules by interlayer cations, variation of electrostatic surface potentials because of differences in layer charge location and the size and the morphology of the smectite and vermiculite particles.

Osmotic swelling

Beyond d_{001} –spacings of 22 Å osmotic swelling occurs with diffuse double layers, where the driven force is the concentration gradient (Lagaly and Dékány, 2013). Thereby, a competition of repulsive electrostatic forces and long-range attractive von der Waals (vdW) forces govern the interactions between adjacent layers (Gilbert et al., 2015; Laird, 2006). Recent cryogenic transmission electron microscopy (cryo-TEM) and small-angle X-ray scattering (SAXS) studies on Na^+-saturated montmorillonites showed the importance of long-range vdW forces to the structure of osmotic hydrates (Tester et al., 2016). Indeed, the tendency of osmotic swelling of Na^+-saturated smectites is the principal cause of for example shale deposit instability, which can potentially lead to a collapse of bore-holes in oil well drilling operations, however, this kind of swelling is beyond the scope of this thesis. Nevertheless, it should be pointed out that the influence of particle size and layer charge will be discussed and how vdW forces also contribute to the crystalline swelling process (see chapter 9).

4 Infrared (IR) spectroscopy

IR spectroscopy is a technique based on the interaction between electromagnetic radiation and molecules in the IR wavelength range. It is an energy sensitive method and its principle is based on periodic changes of dipolmoments caused by molecular vibrations between 10^{-12} and 10^{-15} seconds of molecules or group of atoms (Griffiths, 2006). Thus, IR spectroscopy allows studying molecular structures on a time scale that is much shorter compared to those of other experimental techniques such as e.g. nuclear magnetic resonance (NMR) measurements (10^{-3} to 10^{-10} s) or dielectric relaxation[4] spectroscopy, which measured transitions that occur in the 10^{-2} to 10^{-12} s time domain (Sposito and Prost, 1982).

Planck's law describes the energy of electromagnetic radiation:

$$E = h \times \nu \qquad (4.1)$$

The frequency ν of electromagnetic radiation is:

$$\nu[Hz \ or \ s^{-1}] = \frac{c[^m/_s]}{\lambda[m]} \qquad (4.2)$$

(4.2) in (4.1):

$$E[J] = \frac{h[Js] \times c[^m/_s]}{\lambda[m]} \qquad (4.3)$$

With E = energy of light [J or eV], h = Planck's constant [6.63×10^{-34} Js], v = frequency [Hz or s^{-1}], λ = wavelength [nm] and c = speed of light [2.999×10^8 m/s].

The relation between the wavelength λ and the wavenumber $\tilde{\nu}$ is:

$$\tilde{\nu}\,[cm^{-1}] = \frac{10000}{\lambda[\mu m]} \qquad (4.4)$$

---

[4] The dielectric relaxation spectroscopy covers all techniques that measure the result of a movement of dipoles and electric charges due to an applied alternating field in the broad frequency regime from 10^{-6} Hz up to 10^{12} Hz (λ = 3×10^{16} to 0.03 cm) Kremer, F. and Schönhals, A. (2003) Broadband dielectric measurement techniques, in: Kremer, F., Schönhals, A. (Eds.), Broadband dielectric spectroscopy. Springer, pp. 35-56.

According to (4.3) energy and frequency are directly proportional. Depending on the wavelength, the absorption of electromagnetic radiation by a material (atoms and molecules) causes different changes (Figure 4.1). In case of a high energy radiation in the UV/VIS range with short wavelengths ($\approx$ 180-800 nm) affects the movement of the electrons in an atom and lifts them into a higher energetic state. The absorption of IR radiation with lower energies leads either to a stretching of the bond lengths (stretching vibration) or to change in the bond angles (bending vibration).

An infrared spectrum is obtained when radiation is sent through a sample and is determined how much of the incoming radiation is absorbed at a particular wavelength. The energy at which an absorption band is measured corresponds to the vibration energy of a chemical bond in a molecule. The intensities and positions of these absorption bands depend on the atom mass, length and strength of bonds, the degree of crystallinity and the morphology of the investigated particles (Gottwald and Wachter, 1997).
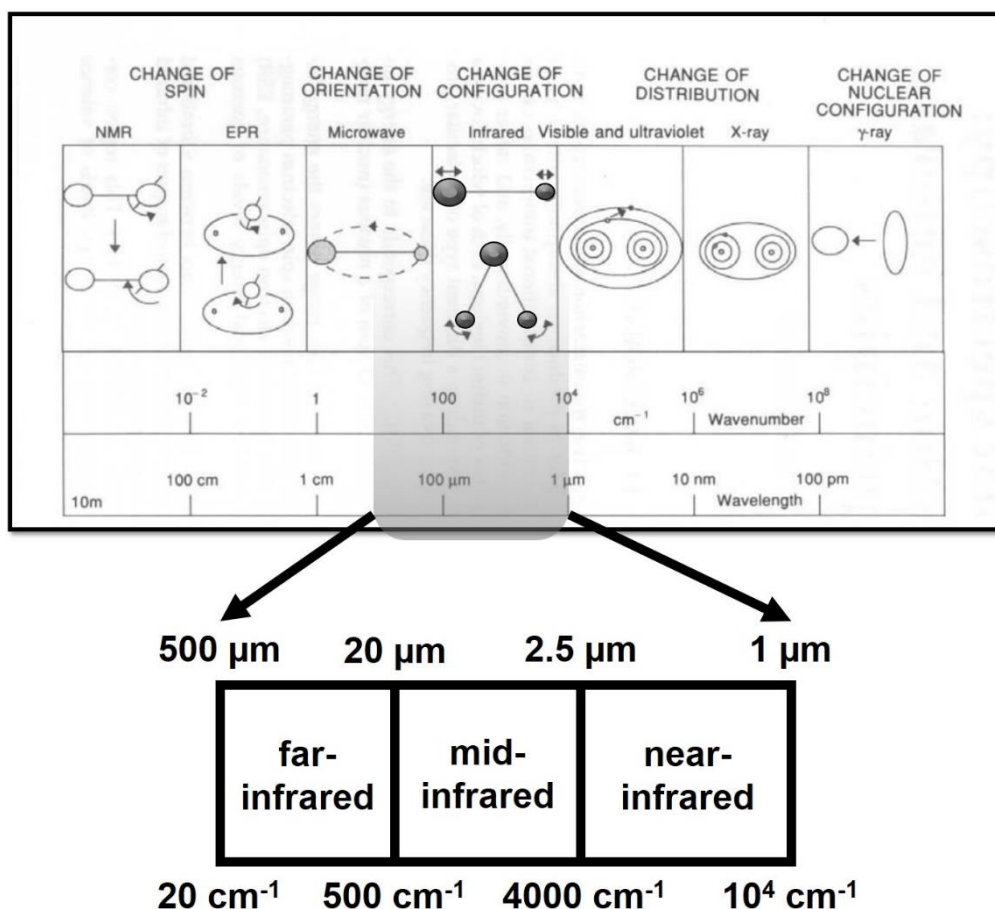
Figure 4.1 The Illustration shows the infrared range within the electromagnetic spectrum. According to. (Russell and Fraser, 1994).

In clay mineral studies, IR spectroscopy is frequently used to investigate the chemical properties and composition, isomorphous substitution, bonding and structural changes upon chemical modification of clay minerals (Johnston, 2010; Komadel, 2003; Madejova, 2003; Madejová et al., 1998; 2002; Petit and Madejova, 2013; Zviagina et al., 2004). Commonly, it is a complementary method to XRD and other analytic methods, however, the advances of this spectroscopic technique makes IR spectroscopy an informative single technique for revealing crystal-chemistry of 2:1 layer silicates (Madejova and Komadel, 2001; Petit, 2006). Beside STA it is a useful tool for detecting mineral impurities, notably the presence of organic compounds or associated minerals like calcite and kaolinite in bentonite (Johnston, 1996; Madejova et al., 2002). In contrast to XRD, both crystalline and amorphous minerals or rather impurities can be identified using IR spectroscopy. IR spectra can serve as a fingerprint for mineral identification, or probably the most effective way to use IR is that it can also give unique information about the intercalation and migration behavior of ions into the clay interlayers (Friedrich et al., 2006; Johnston et al., 1992; 2012).

Since the continuous developments using Fourier transform instrumentation the application of IR spectroscopy is significantly increased in clay mineral studies (Madejova, 2003). In contrast to the old dispersive method, the entire spectrum is detected via an interferogram (time depended) and converted by a Fourier transformation in a conventional spectrum. This spectrum is frequency depended and has the significant advantage over a dispersive spectrometer that it not only detect intensity over a narrow range of wavelengths at a time. In general, the infrared region can be divided into near infrared ($10000 - 4000$ cm^{-1}), mid infrared ($4000 - 400$ cm^{-1}) and far infrared ($400 - 50$ cm^{-1}). By far the most used and established region is the mid infrared (MIR) region where the fundamental vibrations of layer silicates occur (Farmer, 1974).

4.1   Vibrations of 2:1 layer silicates

The pioneering IR spectroscopic studies of clay minerals (Farmer, 1968, 1974; Farmer and Russell, 1964) provided a sound basis for many assignments of IR spectral bands of 2:1 layer silicates. According to the lamellar structure, the vibrations of layer silicates can be separated into those of the constituent units: the structural hydroxyl groups of the octahedral sheet, the tetrahedral sheet and the interlayer cations.
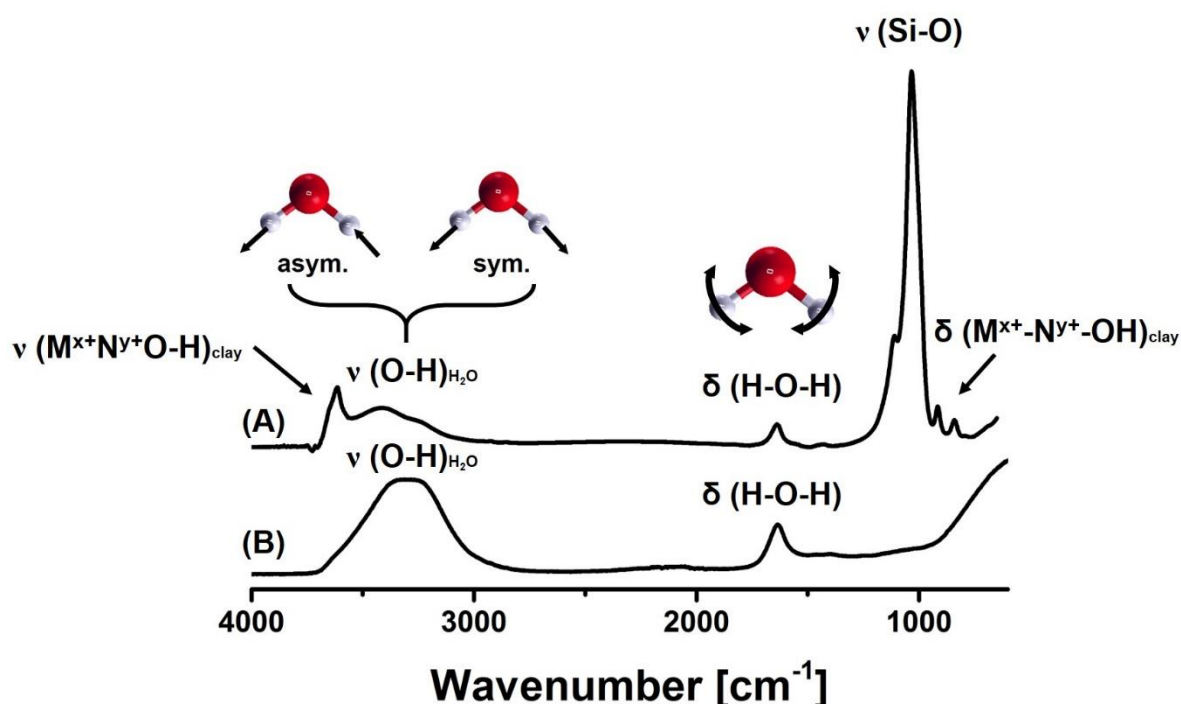
Figure 4.2 FTIR spectra of (A) Na$^+$-saturated smectite and (B) water in the 4000-600 cm^{-1} region showing where the three fundamental vibrational mode of H_2O and the vibrations of the 2:1 layer silicate absorb. M^{x+} and N^{y+} represent the cation of the octahedral sheet.

To illustrate these vibrational bands, representative IR spectra of a hydrated smectite and bulk water are shown in Figure 4.2 showing the overall spectral assignments of the bands of H_2O called O-H stretching (asymmetric and symmetric ν(O-H)$_{H2O}$) and H-O-H bending vibration δ(H-O-H). In bulk (liquid) water (Figure 4.2 A), the asymmetric and symmetric ν(O-H)$_{H2O}$ are shifted to lower frequency at 3490 and 3280 cm^{-1} and δ(H-O-H) is observed at 1644 cm^{-1}(Eisenberg and Kauzmann, 1969). Between ≈ 3700 and 3400 cm^{-1} ν(M^{x+}N^{y+}O-H) bands occur and correspond to the stretching vibrations of OH groups of the octahedral sheet. ν(O-H)$_{H2O}$ of adsorbed water is observed

between $\approx$ 3700 and 2900 cm^{-1} and the δ(H-O-H) band is observed in the in the 1640 to 1610 cm^{-1} region (Russell and Farmer, 1964). Si-O stretching vibrations ν(Si-O) in the tetrahedral sheet are characterized by a broad absorption band between 1250 and 1000 cm^{-1}. The bending vibrations of the structural OH groups δ(M^{x+}N^{y+}-OH) are diagnostics of the chemical composition of the octahedral sheet and can be obtained between 950 and 550 cm^{-1}.

Since this thesis only deals with the MIR region, the vibrational bands of the interlayer cation in FIR region and the additional combination and overtone bands in the NIR are not shown in Figure 4.2. A study of the FIR and NIR was not performed and the determination of combination bands found in NIR is beyond the scope of this thesis. However, it should be pointed out that field spectrometers and remote-sensing only work in the NIR region (Petit and Madejova, 2013).

4.1.1 Vibrations of adsorbed and interlayer water

The major vibrational bands of H_2O occur in two regions of the MIR corresponding to the ν(O-H) and δ(H-O-H) region and illustrated in Figure 4.2. Unfortunately, the analysis of ν(O-H) is commonly impeded due an overlap of bands produced by the structural OH groups ν(MO-H) and absorbed water. The δ(H-O-H) region is comparatively free from any other band. In addition, δ(H-O-H) is sensitive to the extent of hydrogen bonding between H_2O molecules and, hence, it can be used as a molecular probe for water-clay interactions.

IR studies showed that the vibrational bands of water change as a function of water content and that at water contents lower than 6 H_2O per interlayer cation the H_2O molecules are highly polarized by their proximity to the exchangeable cation (Johnston et al., 1992; Madejová et al., 2002; Schuttlefield et al., 2007; Xu et al., 2000). A decrease and shifting of δ(H-O-H) to lower wavenumbers, commonly observed in smectite dehydration (Johnston et al., 1992; Madejová et al., 2002; Xu et al., 2000), indicate an overall decrease in H-bonding. In addition, numerous studies based on other dielectric measurements and neutron scattering data (Sposito and Prost, 1982) have shown that the water molecules coordinated to the interlayer cation are in a less mobile, constrained environments relative to those in bulk water (Johnston et al., 1992). The focus of this early studies was based on the evolution of δ(H-O-H) and their

relation to the exchangeable cation and water content, but the accompanied spectral changes of $v(O-H)_{H2O}$ could not be determined due an overlap of bands produced by $v(MO-H)$.

As an alternative method to avoid this overlapping, deuteration exchange can be used. Using D_2O saturation, the absorption bands of water shift to lower wavenumbers whereas the position of $v(MO-H)$ of the structural OH groups remains unaffected (Russell et al., 1970; Russell and Fraser, 1971). Kuligiewicz et al. (2015) reestablished D_2O saturation of homoionic Na^+- and Ca^{2+}-exchanged smectites and proved the existence of a high-frequency $v(O-H)$ of interlayer water assigned to water molecules located at the interface of the siloxane surface (Kuligiewicz et al., 2015b). This band can be found between 3630 and 3610 cm^{-1}. Using D_2O, $v(O-D)$ appears at frequencies ranging from 2695 and 2680 cm^{-1}. The position of this band is correlated with layer charge and provides a less time consuming method compared to the traditional ones (see chapter 5).

4.1.2 Vibrations of the octahedral sheet

The position and intensity of the vibrations of the structural OH groups, which means the $v(M^{x+}N^{y+}O-H)$ between 3700 and 3400 cm^{-1} and $\delta(M^{x+}N^{y+}-OH)$ between 950 and 550 cm^{-1}, are strongly influenced by their immediate chemical environment. In this sense, IR spectroscopy allows to probe all cation pairs that share OH groups, regardless of the cation mass or valence (Gates, 2005). Unfortunately, the analysis of the $v(O-H)$ region is commonly impeded as described above. In addition, local disorder causes broadening of discrete vibrational bands resulting in overlap and poor resolution of spectral features in IR spectra. For this purpose a decomposition and curve-fitting methodology to IR spectra, especially to the $v(M^{x+}N^{y+}O-H)$ region, was made (Besson and Drits, 1997a, b; Slonimskaya et al., 1986). Their calculations were based on the IR spectra of well-known dioctahedral micas with varied chemical composition. Further researchers have applied this procedure to the interpretation of $v(M^{x+}N^{y+}O-H)$ in the IR spectra of dioctahedral smectites (Gates et al., 2002; Madejova et al., 1994; Petit et al., 2002; Zviagina et al., 2004). According to their studies some general regularities regarding the sequence of the different structural OH groups can be derived:

In case of identical (or similar) mass, a decrease in the valence sum will decrease the resulting wavenumber:

(1) $v(Al^{3+}_2O-H) > v(Al^{3+}Mg^{2+}O-H) > v(Mg^{2+}O-H)$,

(2) $v(Fe^{3+}Al^{3+}O-H) > v(Fe^{3+}Mg^{2+}O-H) > v(Fe^{2+}Mg^{2+}O-H)$

(3) $v(Fe^{3+}_2O-H) > v(Fe^{3+}Fe^{2+}O-H) > v(Fe^{2+}Fe^{2+}O-H)$

In case of a same valence sum, an increase in the mass (by means of $m(M^{x+}N^{y+})$ in g/mol) will decrease the resulting wavenumber:

(4) $v(Al^{3+}Mg^{2+}O-H) > v(Fe^{3+}Mg^{2+}O-H) > v(Fe^{3+}Fe^{2+}O-H)$,

(5) $v(Al^{3+}_2O-H) > v(Al^{3+}Fe^{3+}O-H) > v(Fe^{3+}_2O-H)$,

(6) $v(Mg^{2+}_2O-H) > v(Fe^{2+}Mg^{2+}O-H) > v(Fe^{2+}_2O-H)$.

The same rules from the O-H stretching vibration, described above, can be applied to $\delta(M^{x+}-N^{y+}-OH)$. The amount of the $\delta(M^{x+}-N^{y+}-OH)$ vibration bands reflects partial substitutions of octahedral Al^{3+} by Mg^{2+} and Fe^{2+} in dioctahedral smectites. The position of the $\delta(M^{x+}-N^{y+}-OH)$ is strongly influenced by the occupancy of the octahedral sheet and, consequently, dioctahedral 2:1 layer silicates absorb in the 950 – 800 cm^{-1} region while $\delta(M^{x+}-N^{y+}-OH)$ of trioctahedral species is shifted to lower wavenumbers in the 700 – 600 cm^{-1} region. For dioctahedral smectites, the $\delta(M^{x+}-N^{y+}-OH)$ region of the MIR is quite well resolved. Numerous IR studies have paid attention to this region since this region (a) is well suited for monitoring structural modifications during acid treatment of smectites (Komadel, 1999; Komadel and Madejová, 2013; Madejová et al., 1998) and (b) provides valuable information on the composition of the octahedral sheet (Vantelon et al., 2001).

In addition, a correlation between $\delta(M^{x+}-N^{y+}-OH)$ and the water content can also be found (Xu et al., 2000). Sposito et al. (1983) observed at dehydration under vacuum a change of the intensities of $\delta(M^{x+}-N^{y+}-OH)$, which they interpreted as an evidence that the OH groups contained within the clay structure itself are influenced by changes in water content. Xu et al. 2000 quantified the change in molar absorptivity upon lowering the water content and showed the influence of water content on the band position. Interestingly, $\delta(M^{x+}-N^{y+}-OH)$ corresponding to the isomorphous substitutions $\delta(AlFe-OH)$ and $\delta(AlMg-OH)$ were most perturbed by lowering the water content.

4.1.3 Vibrations of the tetrahedral sheet

Regarding the structure of a tetrahedral sheet, each SiO_4 tetrahedron is linked to an adjacent tetrahedron by sharing three oxygen atoms (O_b, chapter 2.1) to form a hexagonal and pseudohexagonal ring, respectively, in the plane spanned by a_0 and b_0. Their corresponding Si-O stretching vibrations $\nu(Si-O_i)$ were called in-plane vibrations. The fourth tetrahedral apical oxygen atom (O_a) of all tetrahedra points to the same direction and were called out-of-plane vibrations $\nu(Si-O_o)$. Accordingly, four $\nu(Si-O)$ vibration bands are discussed in dioctahedral smectites (Yan et al., 1996). The spectral region of these Si-O bonds is characterized by a broad absorption band between 1250-1000 cm^{-1} (Figure 4.2), where $\nu(Si-O_i)$ and $\nu(Si-O_o)$ are strongly superimposed. Besides using curve-fitting methods it is hardly possible to distinguish between different $\nu(Si-O)$ in the smectite layer. On the basis of early pleochroic studies of Farmer and Russel (1964) the $\nu(Si-O_o)$ at 1086 cm^{-1} was assigned to a perpendicular, out-of-plane vibration, which was confirmed by Johnston and Premachandra (2001) for a Na^+-exchanged montmorillonite using polarized ATR-FTIR. Yan et al. (1996) proposed that $\delta(H-O-H)$ of interlayer water and the $\nu(Si-O_i)$ at 1046 and 1020 cm^{-1} of the tetrahedral sheet are coupled as the layers come closer together. They interpreted that these $\nu(Si-O_i)$ are somehow coupled to the vibrations of interfacial water molecules, but no details about the coupling mechanism were provided (Yan et al., 1996). In addition, this study were based on clay gels with very high water contents ratio m_w/m_c (mass water per mass clay sample) ranging between 25.49 and 0.71, and consequently, their results for low water contents are not well correlated and huge divergences in their measurement values were observed. In this thesis, the coupling of water release and the structural changes in the tetrahedral sheet was re-evaluated at very low water contents (< 3 H_2O / Na^+) and described in chapter 8.

4.1.4 Phenomenological description of optical phonons

In recent years, theoretical methods have provided new insights into the calculation of phonons and vibrational spectra (Acik et al., 2010; Queeney et al., 2003). Phonons are regarded as quantum of crystal vibrational energy or can be considered as standing elastic waves. A distinction is made between acoustic phonons and optical phonons. Acoustic phonons oscillate in phase and optical phonons propagate in an out-of-phase

movement through a solid. Optical phonons were called optical since in an ionic crystal such as a silicon oxide they are excited by infrared radiation (Chabal et al., 2001).

Lange (1989) provided the experimental evidence that aside a longitudinal optical (LO) mode additional vibrations occur in thin amorphous SiO_2 films, including a transverse optical (TO) mode (Lange, 1989). Tian et al. (2010) revealed that the intensity of the transverse optical (TO) band are much weaker compared to the LO peak. They demonstrated the ability of the LO phonon mode to analyze the silanization kinetics of the SiO_2 surfaces and found a linear correlation between the LO mode and the SiO_2 thickness.(Tian et al., 2010) These studies are based on the observations of Berreman (1963), who first reported the effect of the excitation of the LO mode by using oblique incidence with p-polarized light (Berreman, 1963).

4.2   IR techniques

For powedered samples transmission IR spectroscopy is the most frequently used method with KBr pressed disc technique, which is found to be very useful for a routine characterization of clay minerals (Madejova, 2003). Here, a very low sample/KBr ratio of about 1% is used and hard-pressed into a disc. KBr is known to be hygroscopic and, hence, the KBr matrix is not suitable to study clay-water interactions. Therefore, studies on self-supported clay films (SSF) measured in transmission are favored. SSF are prepared from a suspension of the sample, pipeted onto a polyethylene sheet and peeled-off after drying. IR measurements of SSF within a heated cell allow heating and infrared analysis up to 200 °C. However, in order to gain information about the silicate absorption bands in the $1200 - 400$ cm^{-1} region a thin film less than 6 mg/cm² is required, which is rather complicated (Madejova, 2003).

To overcome these restrictions several immersion-based methods for preparation of surface attached films for IR spectroscopy exist. Techniques of film preparation are the layer-by-layer assembly (a combined use of clay particles and a positive charged polyelectrolyte formed at the solid-liquid interface) and the Langmuir-Blodgett (LB) technique formed at the gas-liquid interface. LB films can be obtained using spreading, compression or film transfer techniques and reviewed in (Ras et al., 2007b). However, the thin films of clay minerals are only weakly physisorbed on the surface of the carrier surface and can peel off during heating. Hanson et al. (2003) described an improved method to prepare strongly bonded monolayer films on the native oxide surface of Si

(SiO$_2$/Si) (Hanson et al., 2003). The so-called T-BAG (Tethering by aggregation and growth) technique was initially developed for the deposition of self-assembled monolayers (SAMs) of phosphonic acids but can be adapted for deposition of thin films of clay mineral particles (see chapter 8).

4.2.1 IR experiments under protective atmosphere

IR measurements were performed in an oxygen free atmosphere under N$_2$ purging and analyzed with FTIR transmission spectroscopy. Here, the FTIR spectra were recorded on a spectrometer equipped with a deuterated-triglycine sulfate (DTGS) detector (Bruker Vertex V70, Bruker Optics, Germany). 1024 scans in the 7500 – 400 cm^{-1} spectral range were recorded with a resolution of 4 cm^{-1}.

Therefore, a silicon wafer (thickness 500 µm) of 3 cm × 1 cm, cut parallel to (111), was used as supporting material (Figure 4.3). The wafer was cleaned with piranha solution (1:3 30% H$_2$O$_2$: 18 M H$_2$SO$_4$ for 30 min at 80 °C), thoroughly rinsed with deionized water and dried in a stream of N$_2$. Afterwards, the silicon wafer was immersed in a dispersion of the clay with a solid content of 6 × 10^{-3} %. The dispersion was heated at 105 °C until complete evaporation ($\approx$ 12 h) of the liquid and the clay mineral particles covered both sides of the wafer surface (Hanson et al., 2003; Vega et al., 2012).

In the course of the preparation of the homoionic smectites traces of glycerol were inherited from the dialysis tube. Unfortunately, glycerol is very IR active and bands superimpose with bands of interlayer water. Therefore, the sample was heated to 400 °C to remove the glycerol. Afterwards the sample at the wafer was rehydrated at 53 % r.h. above a saturated Mg(NO$_3$)$_2$ solution. Equilibration was obtained after two weeks.

After equilibration at 53% r.h. the coated wafer was mounted on a heatable sample holder and analyzed with FTIR transmission spectroscopy. The temperature of the sample was increased stepwise from 60 °C to 300 °C and spectra were recorded at 60 °C (see chapter 8).
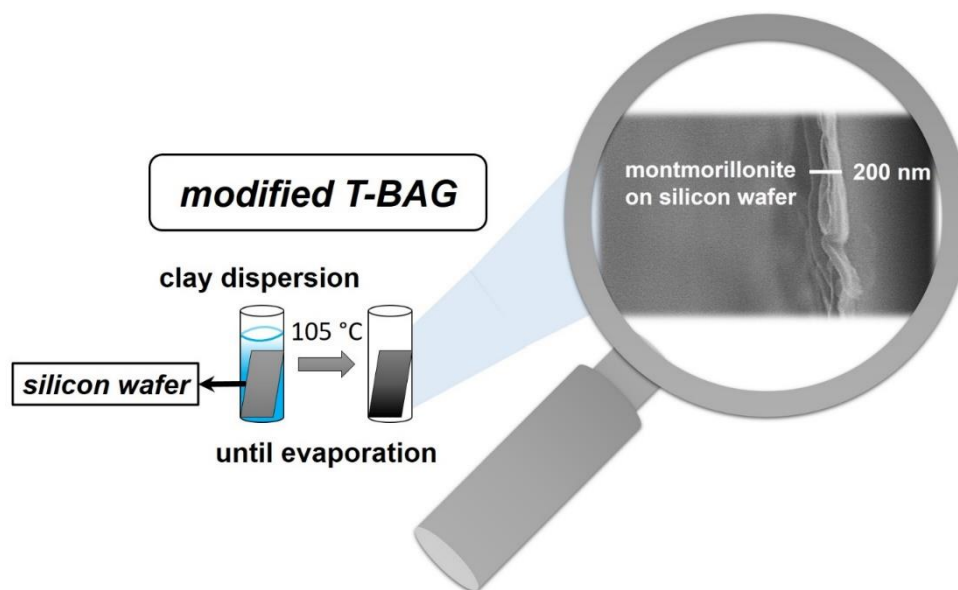
Figure 4.3 Illustration of the modified T-BAG process. Inside the magnifier a scanning electron microscopy image of a silicon wafer coated with a thin layer of about 200 nm montmorillonite is shown.

4.2.2 Environmental IR microbalance cell

The spectra were recorded on a FTIR spectrometer equipped with a deuterated-triglycine sulfate (DTGS) detector (Nicolet™ iS™ 10, Thermo Scientific). FTIR spectra were obtained by coadding 64 scans in the $4000 - 650$ cm^{-1} spectral range with a resolution of 4 cm^{-1}. To control time-based experiments, the FTIR spectrometer was controlled by using a data collection and analysis software (OMNIC Series Software, Thermo Scientific). A 16 cm pathlength gas cell was placed in the sample compartment of the FTIR spectrometer (Figure 4.4). The cell was fitted with two 50 × 3 mm ZnSe windows and sealed with O-rings. The gas cell was connected to a microbalance (C-34 microbalance, Cahn). For all experiments the flow rate was constant at 100 sccm. To regulate the wet and dry N_2 flow and to adjust the relative humidity, respectively, two mass-flow controllers (Type 1179A mass-flo® controller, MKS) were used. The r.h. was monitored online with a humidity sensor (model HMP35A, Vaisala).

The sample was mounted inside of one ZnSe window, which was crossed first by the incident IR beam. The sample film was deposited at the ZnSe window from a sonicated dispersion (1 mg / 1 mL H_2O) and dried at 60 °C (≈ 12 h) in a vacuum oven. Additionally, a 'second' powder sample (≈ 10 mg) was placed in the weighing arm of the microbalance (Figure 4.4). Both, the film and powder sample were subjected to the following treatments: Equilibration of the sample at 85 ± 1% r.h. for 12 h. The mass of

the sample was recorded simultaneously from the microbalance and the spectra were collected every 5 min. After equilibration, the r.h. was decreased stepwise from 85 to 0% (nominal). To ensure equilibration of the sample, the r.h. was kept 2 h at each step. For the adsorption and to examine hysteresis, the r.h. was again increased stepwise from 0 (nominal) to $85 \pm 1\%$ following the same data collection as in the desorption branch. After recording of the water vapor desorption and adsorption isotherm, the sample was dried under dry N_2 purging for 48 h. All spectra were recorded at 25 °C.

The dry mass of the sample was determined by plotting the intensity of δ(H-O-H) against the mass of the sample and extrapolating the plot to zero band intensity (Johnston et al., 1992). The intensity of δ(H-O-H) is directly proportional to the amount of water adsorbed by the 2:1 layer silicate. Integrating the area below the region between 1700 and 1600 cm^{-1}, the water content of the samples was calculated from each FTIR spectrum in dependence of r.h.. The amount of H_2O per Na^+ was calculated using the measured CEC as structural intrinsic property of the 2:1 layer silicates. The CEC measurement uncertainties were set to 2% of the measured values and, therefore, the error bars were calculated for H_2O / Na^+ (see chapter 9).
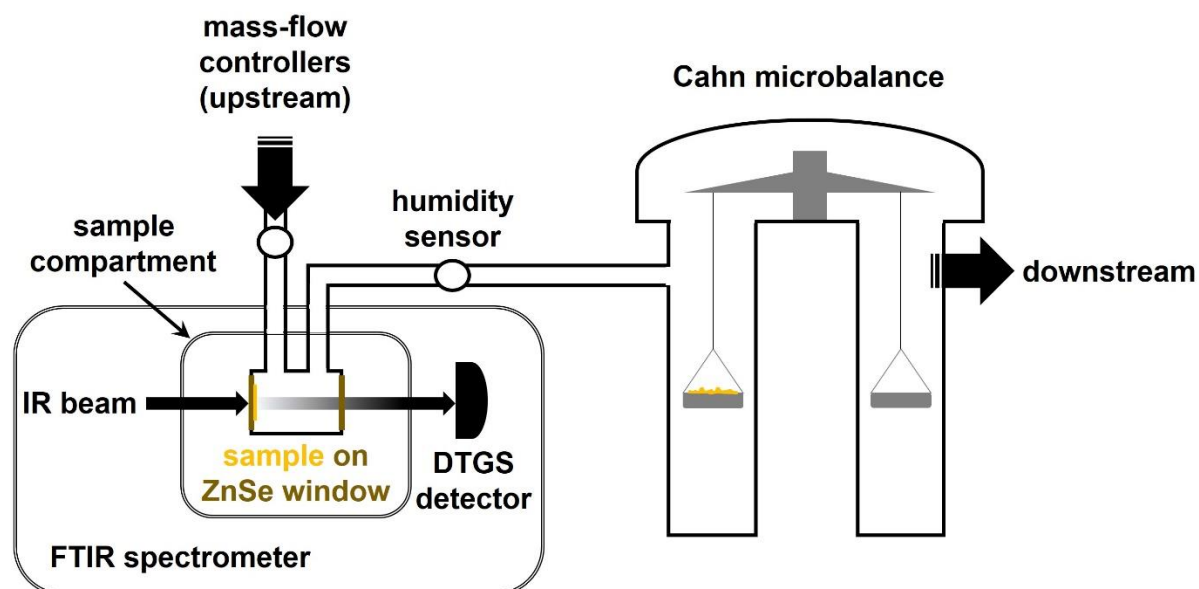
Figure 4.4 Schematic drawing of the FTIR/gravimetric cell showing a 16 cm pathlength gas cell placed in the sample compartment of the FTIR spectrometer, which is connected to a Cahn microbalance. The cell was fitted with two 50 × 3 mm ZnSe windows and sealed with O-rings. Two MKS mass-flow controllers are used to regulate the wet and dry N_2 flow and to adjust the relative humidity, respectively.

5 Materials and methods

5.1 Material origin

The materials were selected with respect to their layer charge, charge location (octahedral vs. tetrahedral charge) and morphology. Four bentonites, a vermiculite and a fine grained illite sample were chosen to study the influence of structural intrinsic properties on the hydration characteristics of 2:1 layer silicates.

Table 5.1 Origin of samples.

name	provenance	supplier
Calcigel®	Bavaria, Germany	former Süd-Chemie AG (acquisition by Clariant AG)
Volclay®	Wyoming, USA	former Süd-Chemie AG (acquisition by Clariant AG)
SAz-1	Arizona, USA	Source Clay Repository of the Clay Mineral Society
SHc-1	California, USA	Source Clay Repository of the Clay Mineral Society
Vermiculite	Russia	Thermax® (Austria)
Illite ('Arginotec® NX')	France	B. + M. Nottenkämper

Smectites are the main component in bentonites, which is basically a rock term. Looking at the formation process of the bentonite deposits of economic interest, including those selected materials in this study, there are some generalizations: (1) they form mainly from alteration of volcaniclastic and/or pyroclastic rocks , (2) they are commonly formed by diagenetic alteration of volcanic glassy ashes or hydrothermal alteration of volcanic glass, favored by fluids that leach alkali elements, whereas the Mg^{2+} concentration controls the growth of the smectite formation (Christidis and Huff, 2009; Galán and Ferrell, 2013).

The blended bentonite Calcigel® have a high dioctahedral smectite content (Delavernhe et al., 2015; Steudel and Emmerich, 2013; Wolters et al., 2009) and was formed by diagenetic alteration of volcanic ash (Aziz et al., 2010; Ulbig, 1994). According to Steudel and Emmerich (2013) Calcigel® contains a Ca^{2+}-rich dioctahedral smectite (25 ± 11%), Mg^{2+}-rich dioctahedral smectite (29 ± 10%), muscovite/illite (muscovite_2M1) (14 ± 1%), kaolinite (4 ± 1%), quartz (6 ± 1%), plagioclase (albite) (3 ± 1%), calcite (3 ± 1%) and dolomite (7 ± 1%).

Volclay® is a blended bentonite and originates from the 'Wyoming bentonites'. This term includes deposits at Wyoming, Montana and South Dakota and have a high dioctahedral smectite content (Wolters et al., 2009). Wyoming bentonites are of cretaceous age and were formed from the diagenetic alteration of volcanic ashes (Moll, 2001). The bulk material shows a slight variation in its mineralogical content. The results from Steudel and Emmerich (2013) showed that Volclay® contains a Na^{+}-rich dioctahedral smectite (60 ± 4%), a Ca^{2+}-rich smectite (20 ± 4%), a muscovite/illite (muscovite_2M1) (3 ± 1%), quartz (4 ± 1%), orthoclase (4 ± 1%), albite (4 ± 1%) and gypsum (4 ± 1%).

SAz-1 and SHc-1 are source clays obtained from the Clay Repository of the Clay Minerals Society. SAz-1, also known as the Cheto bentonite, originates from the County of Apache, Arizona in the Bidahochi formation (Grim and Güven, 1978). The origin of SHCa-1 is in the Mohave Desert, California, in the Red Mountain andesite series and both are of Pliocene age (Moll, 2001). In particular, SAz-1 has a Ca^{2+}-rich montmorillonite content (up to 98 weight percent) and formed by alteration of volcanic ash (Chipera and Bish, 2001). Due to an extensive exchange from stream and lake water by forming the Cheto bentonite, SAz-1 exhibited a high Mg^{2+} content (Murray, 2006a).

The formation process of the type locality of the hectorite, which is one of the main component of SHca-1, is described as a reaction of travertine with lithium- and fluorine-bearing hot water producing a Mg^{2+}-rich bentonite (Hosterman and Patterson, 1992). The bulk material of SHCa-1 contains a significant amount of calcite (43 %), dolomite (3 %) and quarz (1 %) (Chipera and Bish, 2001). Occasionally, analcime can be found in the source clay SHCa-1, which was contributed to forming times, where the

exchange from ashes and spring water was inoperative and, hence, volcanic ashes altered to a zeolitic mineral.

A trioctahedral vermiculite is mainly the product of weathering from biotites by the release of interlayer K^+ (Galán, 2006). Unfortunately, beside the producing country Russia of the selected vermiculite, there are no information about its geological origin. The selected, commercially available vermiculite has a high content of trioctahedral vermiculite (84 %) and additionally contains phlogopite (14 %) and some accessory calcite (Steudel, 2009).

Illites commonly occur in soils and sedimentary rocks. Since there are no information dedicted to the question of the formation of the selected illite, its origin will not be dealt with here. According to Steudel (2009) the mineralogical quantification of 'Arginotec® NX' reveals 75 % dioctahedral illite, 7 % phlogopite, 5 % kaolinite, 5 % feldspars and accessory minerals like anhydrite, apatite, calcite and quarz.

5.2   Purification of natural clays

A chemical pre-treatment to enrich smectites by separation of the fine clay fraction (< 0.2 µm) from the bulk materials was required to reduce the cementing interactions due to carbonates, iron (hydr)oxides and organic materials as described by (Tributh and Lagaly, 1986a, b). Therefore, 300 g of the bulk samples were purified according to (Wolters et al., 2009):

Carbonates were decomposed by an acetic acid-acetate buffer treatment followed by dissolution of mainly iron(hydroxides) and organic matters by a buffered dithionite-citrate solution and adding of hydrogen peroxide, respectively (Mehra and Jackson, 1960; Tributh and Lagaly, 1986a). A detailed description of these procedure is given in (Steudel, 2009; Wolters, 2005).

The smectites were enriched by a sequential fractionation of different clay fractions by gravitational sedimentation according to Stokes equivalent sphere diameter (esd) The sedimentation time was calculated according to Stoke's law involving the water temperature and the grain diameter of interest:

$$t = \frac{18\eta_0}{(\rho - \rho_0) \times g} \times \frac{h}{d^2} \qquad (5.1)$$

With η_0 = viscosity of water, ρ = density of the selected materials, ρ_0 = density of water, g = gravity force, h = settling distance of the particles and d = esd.

After the sedimentation process, the obtained < 2 µm esd dispersion was centrifuged with a Multifuge 3S-R Heraeus/Kendro at a constant temperature of 20 °C and a rotation speed of 4500 rpm for 25 min to obtain a clear supernatant (Tributh and Lagaly, 1986b; Wolters, 2005). The clear supernatant was replaced with fresh 1 M NaCl solution for repeated reaction (10 times) and then with deionized water (5 times) to remove excess ions after exchange treatment (Steudel and Emmerich, 2013). Afterwards, the samples were dialyzed to remove chloride and surplus cations down to a conductivity of 5 µS/cm using cellulose hydrate dialysis tubes (Nadir®, Carl Roth GmbH, Karlsruhe, Germany) in deionized water. The deionized water was changed daily and the dialysis tubes were treated before in boiling deionized water to remove surplus organic molecules.

After the purifying processes, all samples were dried at 60 °C and then gently ground in an agate mill.

The efficiency of the sodium exchanged form was proved by sodium cation exchange capacity (CEC) higher than 95% as described in (Steudel and Emmerich, 2013).

In the following chapters, the notations BX-M0.2Na were used for Na^+-saturated materials with an esd of < 0.2 µm with X = C and V for Calcigel® and Volclay®. SAz-M2Na and SHc-0.2Na were separated from the SAz-1 and SHCa-1, respectively. The resulting material separated from an industrial Vermiculite is VT-2Na. The material separated from Arginotec® NX' is Ilt-0.2Na. SAz-M2Na has an esd of < 2 µm since for this material an enrichment in the < 2 µm fraction was considered to be sufficient to produce a material without impurities. Due to the large grain size of the selected vermiculite, it was not possible to separate the 0.2 µm esd fraction (Steudel et al., 2009). Accordingly, VT-2Na has an esd of < 2 µm.

Potential source of error: Former studies on the decomposition of carbonates in clay minerals indicated that short reaction times might cause an incomplete dissolution. Lowering the pH down to ≈ 4.5 may result in the deterioration of the clay structure. Hydrogen peroxide destroys organic matter effectively, however, in some cases residues of organic matter may remain.

5.3   Mineralogical characterization

5.3.1   X-ray diffraction analysis (XRD)

The mineralogical characterization of all samples was determined by XRD on a random powder of air dry material (top loading) and oriented samples of 10 mg/cm^2 of sample holder coverage stored at 53 % r.h.. XRD patterns were recorded on a D8 diffractometer with Bragg-Brentano geometry equipped with Lynxeye_XE (192 Si strips) detector (Bruker AXS GmbH, Karlsruhe, Germany). Cu radiation (CuKα) was implemented. The powder patterns were recorded with 0.02° 2θ step size from 2 up to 80° 2θ with 3 s per step. The texture samples were recorded between 2 and 35° 2θ with 0.02° 2θ step size and 2 s per step. Both setups with automatic blend (irradiated area 10 mm), divergence slit was set to 2.5 °, air scatter was set to automatic mode, sample holder with 15 rotations per min and LYNXEYE_XE detector with 2.942 ° opening.

To distinguish between dioctahedral and trioctahedral 2:1 layer silicates the d_{060} reflection was used (Moore and Reynolds Jr., 1997). For dioctahedral smectites the d_{060} is observed between 1.48 and 1.50 Å, 1.52-1.53 Å for trioctahedral smectites, 1.541 Å for vermiculite and 1.499 Å for dioctahedral illite (Brindley and Brown, 1984). Patterns of textured samples especially reveal information about the 00l basal reflections. The textured samples were measured air-dried, after treatment with ethylene glycol (EG) and after heating at 375 °C and 550 °C for 3 h. To determine the rationality of basal reflections the coefficients of variation (CV) was calculated from patterns of the oriented samples solvated EG allowing identification of mixed-layer minerals with random interstratification (Bailey, 1982).

The crystalline swelling of smectites is a stepwise expansion of the layer-to-layer distance, leading to the 1W, 2W and 3W hydration states with increasing basal spacings that can be observed by XRD and described in chapter 3.2. Therefore, powdered samples are stored in closed containers above saturated salt solutions in order to equilibrate with a given humidity (Table 5.2). Samples were first equilibrated at 86 % r.h. for at least 48 h and subsequently XRD patterns were recorded at room temperature over the 2-50° 2θ range with with 0.02° 2θ step size (automatic blend and irradiated area 10 mm, divergence slit was set to 2.5 °, air scatter was set to automatic

mode, sample holder with 15 rotation / min and the LYNXEYE_XE detector with 2.942 ° opening).

Then, XRD patterns were recorded at different r.h. values (Table 5.2) following the same sequence (86, 75, 53, 43 and 11 % r.h.) with at least 48 h equilibrium time before data collection. To determine the deviation from rationality of the 00l reflection series, the CV is calculated for the χ_i measurable reflections over the 2-50 ° 2θ CuKα angular range (Ferrage, 2016).

Table 5.2 Salts used for equilibration (Kutzelnigg and Königsheim, 1963).

r.h. [%]	11	43	53	75	86	93
salt	LiCl	K_2CO_3	$Mg(NO_3)_2$	NaCl	KCl	$NH_4H_2\,PO_4$

In addition, the size of the coherent scattering domains (CSD) was calculated by the Scherrer equation:

$$L = \frac{K\lambda}{\beta \cos\theta} \qquad\qquad (5.2)$$

where L is the mean crystallite size (average of the CSD thickness in Å) in direction normal to the diffracting planes. K is the Scherrer constant, β is the full width at half-maximum (FWHM) after subtracting the instrumental line broadening and expressed in radians of 2θ. To compare the crystallite size of the selected 2:1 layer silicates, the use of low-angle (< 10 ° 2θ) reflections was avoided for this quantitative analysis. The (003) reflection in 2W state was selected to eliminate the effect of mixed layering on peak width (Drits et al., 1997).

5.3.2 X-ray fluorescence analysis (XRF)

The chemical composition of the samples were determined by XRF analysis with a MagiXPRO spectrometer (Philips) equipped with a rhodium X-ray tube (stimulation power of 3.2 kW). An air-dry powdered sample was fused with lithium tetraborate (ratio 1:7). The loss on ignition was determined separately at 1000 ºC for 2 h. The amount of Li_2O in SHc-0.2Na was measured separately (see 5.3.4).

Error: For BV-M0.2Na and BC-M0.2Na the mean standard deviation from four different batch experiments was calculated for each element. The total number of measurements per sample was six. The mean standard deviation are shown in Table 5.3. The raw data are given in the appendix.

Table 5.3 Mean standard deviation for the major elements determined in XRF.

element	SiO_2	Al_2O_3	Fe_2O_3	MgO	CaO	Na_2O	K_2O
BV-M0.2Na	0.19	0.24	0.11	0.05	0.02	0.12	0.02
BC-M0.2Na	0.33	0.32	0.12	0.02	0.01	0.07	0.15

Exchange behavior and interlayer composition

5.3.3 Cation exchange capacity (CEC)

To determine the CEC the Cu-triethylentetramine (Cu-trien) method was used (Meier and Kahr, 1999). Prior to this exchange the samples were stored above a saturated $Mg(NO_3)_2$ solution at 53 % r.h. for at least 24 h and analyzed according to (Wolters et al., 2009). CEC measurements were performed at the resulting pH (pH ≈ 7) to measure the total CEC resulting from both permanent charges and variables charges (CEC_T) by dispersing 50 mg of the samples in 10 mL of deionized water and 5 mL of a 0.01 M Cu-trien solution. After 3 h of shaking, the suspensions were centrifuged 10 min at 4500 rpm at ≈ 20 °C. The concentration of the remaining Cu-trien cations in solution was determined by a photometer at λ = 580 nm (Genesys 10 UV, Thermo Electron Corporation) using a calibration series with different concentrations of Cu-trien. All CEC_T measurements were done twice. CEC_T was related to the dry weight of the

completely dehydrated sample calculated with respect to water content determined by simultaneous thermal analysis (STA).

From the structural formula (5.3.6), the permanent cation exchange capacity (CEC_P) resulting from the mean layer charge (ξ in eq/f.u.) and the molar weight of the unit cell (M in g/mol) can be calculated following the equation:

$$CEC_P = \xi / M \times 10^5 \text{ cmol(+)/kg} \qquad\qquad (5.3)$$

Error: The precision of the method was determined to be 2% according to (Kaiser and Specker, 1956). To allow assessment of the accuracy of CEC_T measurements, Calcigel® and Volclay® were always included in the measurements. Repeated *CEC_T* measurements (> 75) of these materials showed a precision of ± 3 cmol(+)/kg (Kaden, 2012; Steudel, 2009).

5.3.4 Determination of exchanged cations by inductively coupled plasma – optical emission spectroscopy (ICP-OES)

The efficiency of the sodium exchange was proved according to (Steudel and Emmerich, 2013). Therefore, the exchangeable cations (Na^+, K^+, Mg^{2+} and Ca^{2+}) were subsequently analyzed in the supernatant solution after Cu-trien treatment by inductively coupled plasma optical emission spectroscopy (ICP-OES; Jobin Yvon JY 38 S, HORIBA Europe GmbH, Oberursel, Germany). Thereby, 5 mL of the supernatant solution were diluted with deionized water in a volume ratio of 1:1, 1:2 or 1:4 depending on the expected ion concentration. To decompose the Cu-trien complex and to stabilize the solutions 20 µL of HNO_3 were added.

In addition, the content of LiO_2 of SHc-0.2Na were determined by ICP-OES. Thereby, the powder was diluted with nitrohydrochloric acid and with a mixture of hydrofluoric and nitric acid, using a microwave and analyzed by ICP-OES.

Error: Elements, which are determined from highly diluted solutions have a correspondingly large error interval.

5.3.5 Layer charge determination (ξ)

The mean layer charge (ξ) was determined by investigation of the layer charge distribution of the sample using the alkylammonium method (Lagaly and Weiss, 1971). Therefore 100 mg of the powder sample were dispersed in 3 mL of n-alkylammonium formiate solution with alkylammonium ions of chain length from $n_c = 4$ to $n_c = 18$ (except $n_c = 17$) stored 72 h at 60 °C. The samples were washed 16 times with ethanol. Afterwards, an oriented preparation on a glass slide was dried at room temperature and stored in a desiccator above P_2O_5 until XRD measurement were done (0.02° 2θ step intervals from 2 to 15° 2θ with 3 s per step). A muscovite standard was used for height correction.

The intercalation of alkylammonium ions in the interlayer shows in dependence of the chain length a defined interlayer arrangement of mono- ($d_{001} \approx 13.6$ Å), bi- ($d_{001} \approx 17.7$ Å) or pseudotrilayer ($d_{001} \approx 21.7$ Å). In case of high-charged vermiculites, a paraffin-type ($d_{001} > 22$ Å) can be observed, too (Lagaly and Weiss, 1970b). Accordingly, with increasing chain length the basal spacings increase (Lagaly and Weiss, 1970a, b, c). The comparison of the area of an alkylammonium ion (A_C) and the equivalent area that is available for an interlayer cation (A_e) provides the basis for the determination of the cation density. In case of a homogeneous charge distribution the cation density and the charge density are identical. In most cases, smectites exhibit a heterogeneous layer charge distribution since the cation density varies from interlayer to interlayer. Thereby, the transition from mono- to bilayer is observed stepwise. ξ was calculated from the layer charge distribution based on the evolution of the basal spacing (Lagaly, 1994).

For VT-2Na, the rapid estimation of the layer charge was determined according to (Olis et al., 1990). The exchange was done with a chain length of either $n_c = 12$ and $n_c = 18$ and ξ was calculated according to:

$$\xi = \frac{d_{001} - 5.52}{32.98} \qquad \text{for } n_c = 12 \quad (5.4)$$

$$\xi = \frac{d_{001} - 8.21}{32.22} \qquad \text{for } n_c = 18 \quad (5.5)$$

Error: The standard deviation was determined to ± 0.1 eq/f.u. (Delavernhe et al., 2015). The samples have to dry carefully, otherwise to high layer charges are determined (Lagaly, 1981).

5.3.6 Structural formula

The results of the XRF analysis and ξ were used to calculate the stoichiometric composition of the dioctahedral smectites according to Köster (1977) and Wolters et al. (2009). This calculation is based on the assumption of 22 negative charges $[O_{10}(OH)_2]$. For Ilt-0.2Na an exchange with alkylammonium was not possible and, hence, the structural formulae was calculated according to (Stevens, 1945). This calculation involves the measured CEC_T.

Error: For BV-M0.2NA, the effect of impurities correction is estimated to range from 54% to 35% tetrahedral charge correlated to a cristobalite (SiO_2) content ranging from 2% to 5%. Discrete mica ($KAl_2(Si_3Al)O_{10}(OH)_2$) in BC-M0.2Na was quantified between 5 and 6% and, thus, a range of tetrahedral charge between 20 and 23% could vary.

5.3.7 Simultaneous thermal analysis (STA)

The occupancy of *cis-* and *trans*-positions within the octahedral sheet was quantified by STA (STA 449C Jupiter connected to a quadrupole mass spectrometer 403C Aëlos, Netzsch) at the dehydroxylation temperature of 600 °C (Wolters and Emmerich, 2007). The dehydroxylation of dioctahedral smectites can be used to determine the *cis-* and *trans-vacant* character (see chapter 2.2). The *cis-* and *trans-vacant* proportions were calculated by fitting the MS curves of evolved water (m/e = 18) and identifying the peak positions using a peak deconvolution software (PeakFit 4.0, Jandel Scientific). After baseline correction (second derivative zero), the area of the peaks in the temperature range between 350 and 900 °C were integrated and its percentages were calculated. The ratio between the calculated areas equals to the ratio between *cis-* and *trans-* vacant layers. According to Wolters and Emmerich (2007), the boundary between both varieties was defined to 600 °C. The limits of the amount of cis- and trans-vacant octahedral sheets in the dioctahedral smectites are shown in Table 5.4.

Table 5.4 Limits of the amount of cis- and trans-vacant octahedral sheets for classification of dioctahedral smectites (Wolters and Emmerich, 2007).

Octahedral structure	cis-vacant (cv)	cis-trans-vacant (cv/tv)	trans-cis-vacant (tv/cv)	trans-vacant (tv)
Percentage area [%] of MS curve of evolved water during dehydroxylation (m/e = 18)	w_{cv} 100-75 w_{tv} 0-25	w_{cv} 74-50 w_{tv} 26-50	w_{cv} 49-25 w_{tv} 51-75	w_{cv} 24-0 w_{tv} 76-100

5.4 Particle size and surface properties

5.4.1 Specific surface area and pore size distribution

Argon adsorption isotherms at 87 K were measured (Quantachrome Autosorb-1-MP instrument). The samples were outgassed at 95 °C for 12 h under a residual pressure of 0.01 Pa. The specific surface area was calculated according to the BET model ($a_{s,BET}$) in the adsorption range from 0.02 to 0.20 p/p_0 (Brunauer et al., 1938). Due to the turbostratic arrangement of the smectites layers the adsorption of argon simultaneously occurs on external and at micropores surfaces in this low-pressure region (Michot and Villiéras, 2013).

Regarding the pore size in the context of physisorption, three classes were identified: macropores (≥ 50 nm), mesopores (2 – 50 nm) and micropores with widths about 2 nm (Sing et al., 1985). The contribution of microporosity was calculated by the non-local density functional theory (NLDFT) with the model Argon at 87K (zeolite/silica model) on the adsorption branch (Olivier, 1995).

Thommes et al. (2015) refined the original IUPAC classifications of physisorption isotherms and associated hysteresis loop and proposed a new classification (Figure 5.1). There are six major types of adsorption isotherms, however, type I and type IV were subgrouped into two types. The reversible type I represents a concave shaped isotherm towards the p/p_0 axis and characterized microporous solids having relatively small external surfaces (Thommes et al., 2015). The distinction of type I(a) and I(b) was motivated by concerns for different pore size distribution. Type I(a) isotherms were described as microporous materials having mainly narrow micropores (of width < 1

nm), whereas type I(b) isotherms were given by materials having wider micropores and narrow mesopores (< 2.5 nm). Among the most prominent types of isotherms is the reversible type II isotherm typical for non-porous or macroporous adsorbents. Point B represents the onset of multilayer adsorption and, consequently, corresponds to the completion of monolayer coverage. In contrast to type II isotherm, type III isotherm exhibits no point B and thus no monolayer formation can be identified. In addition, type III isotherms were commonly found in nonporous or macroporous materials having relatively weak adsorbent-adsorbate interactions compared to adsorbate-adsorbate interactions. Type IV isotherms were subgrouped in two forms: Type IV(a) isotherms with characteristic hysteresis loop associated with capillary condensation and contrary Type IV(b) isotherms were completely reversible. Both types were observed for mesoporous adsorbents (e.g. mesoporous molecular sieves) and exhibit an initial monolayer-multilayer adsorption comparable to type II isotherms. Relatively weak adsorbent-adsobate interactions were found in Type V isotherms originating for water adsorption on hydrophobic microporous and mesoporous adsorbents. Reversible Type VI isotherms represent a layer-by-layer adsorption on a highly uniform nonporous surface, where the step-height displays the capacity for each adsorbed layer (Rouquerol et al., 2012; Sing et al., 1985; Thommes et al., 2015).

Particular interest is focused on the different emphasis of hysteresis. Therefore, different types of hysteresis loop were classified (Figure 5.2). Here, the occurrence of hysteresis is associated with capillary condensation, depending on the pore structure and adsorption mechanism (Thommes et al., 2015). The steep and narrow loop of type H1 was identified as a clear evidence of delayed condensation on the adsorption branch found in materials exhibiting a tight range of uniform mesopores. Type H2 was subgrouped in two types: Type H2(a) can be found in silica gels and was identified by a very steep desorption branch. Both loop of both types can be associated with pore blocking, whereas the size distribution of neck width of type H2(b) is larger. Plate-like particles (e.g. certain clays) exhibit a hysteresis loop of type H3, when an inert gas like argon or nitrogen is used. Type H4 loop has a similar character to that of H3, however, exhibiting a more distinctive uptake at low partial pressures associated with filling microspores, which is representative in zeolites. A new, but rather unusual type H5 can be found in plugged hexagonal templated silicas (Van Der Voort et al., 2002), which contain open and partially blocked mesopores.
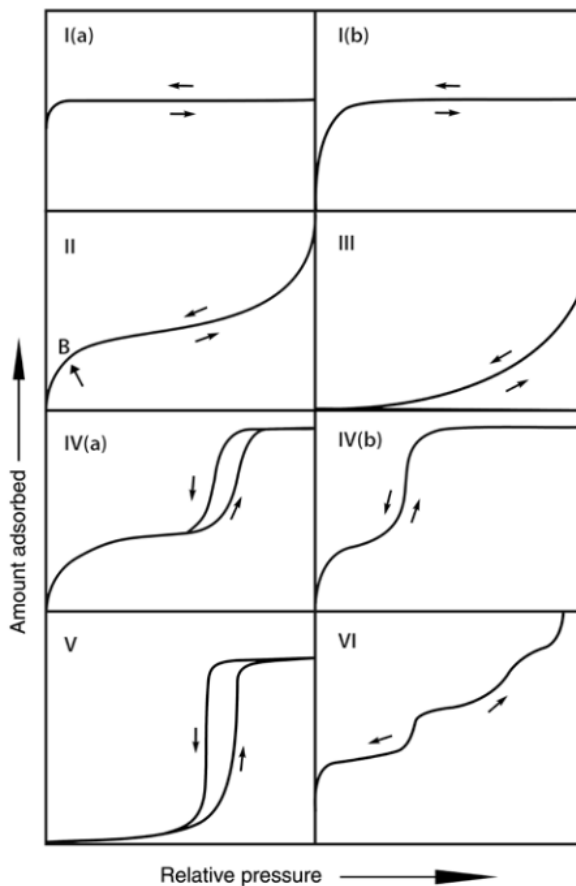
Figure 5.1 Classification of physisorption isotherms, adopted from Thommes et al. (2015).
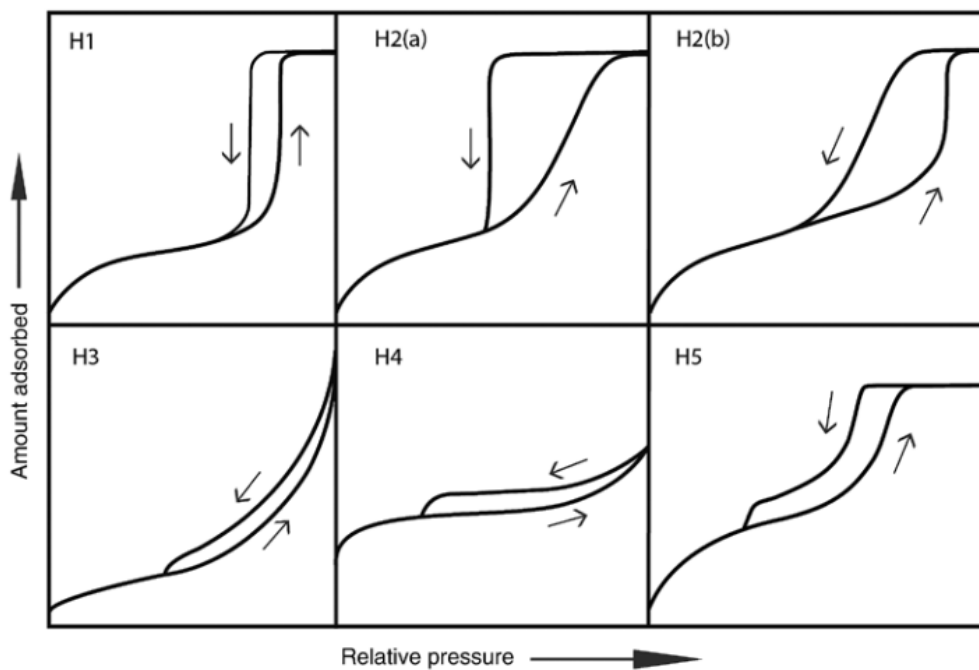
Figure 5.2 Classification of hysteresis loops, adopted from Thommes et al. (2015).

Error: For smectites, the contribution of microporosity due to the overlap of the layers to gas adsorption at low pressures is estimated to range from 10% to 40%. (Le Forestier et al., 2010).

5.4.2 Particle size characterization

The procedure of Delavernhe et al. (2015) was used to study the proportions of the edge sorption sites of the selected 2:1 layer silicates (Delavernhe et al., 2015). As described by these authors, a layer stacking model (n layers per stack of diameter d [nm]) with the specific edge surface area ($a_{s,edge} = 4/(\rho_s \times d) \times 10^6$ [m²/g]) and the specific basal area ($a_{s,basal} = 4/(\rho_s \times h \times n) \times 10^6$ [m²/g]) with h = 0.96 nm and ρ_s = 2700 kg/m³ was considered.

The determination of the mean weighted equivalent diameter (d) of the vermiculite was done with an environmental scanning electron microscope (ESEM; XL 30 FEG Philips, Germany). For a representative overview, the perimeter and basal area were measured from 50 single particles from a random powder. The images were recorded in the gaseous secondary electron detector (GSE detector) mode at a chamber atmosphere of 0.9 Torr and an acceleration voltage of 20 kV.

For smectites, the values for their mean particle size were available from the literature (Bosbach et al., 2000; Cadene et al., 2005; Delavernhe et al., 2015; Poli et al., 2008).

Error estimate: According to (Delavernhe et al., 2015) an over-estimation of about 20 % of the layer stacking was considered.

5.5   Water vapor sorption

The most common technique to study the sorption of water vapor is the examination of water vapor sorption isotherms. In the past, samples were stored above saturated salt solutions in order to equilibrate with a given r.h. (see Table 5.2) to study the adsorption and desorption of water vapor. However, this approach is very time consuming and comprised different uncertainties (e.g. ex-situ weight measurement). To monitor the mass of the solid sample, while increase/decrease the moisture several techniques exist. The water uptake can be determined by either gravimetrical or volumetrical techniques.

5.5.1   Gravimetric water vapor sorption

Water ad- and desorption was determined on a dynamic vapor sorption (DVS) instrument (DVS Vacuum, Surface measurement systems Ltd.), where the relative humidity in the system was controlled by a butterfly valve at downstream while flowing constant water vapor into the system via a mass-flow controller (so-called dynamic mode). These experiments were performed in order to compare our experimental results from the static experiments. One of the main difference to the static experiments is the heatable sample chamber, where the samples can be dried (up to 400 °C) under high vacuum ($\approx 10^{-8}$ Torr $\approx 1.33 \times 10^{-6}$ Pa). Isothermal measurements can be performed in several cycles under a partial pressure ranging from 0.0 up to 0.999 in the temperature range between 20 °C and 70 °C. The recording microbalance has a resolution of 0.1 µg and can detect mass changes up to 150 mg. Each sorption step can be fixed in time or determined by a user defined $\Delta m / \Delta t$ criterion (mass change per time step).

In this study, water vapor sorption isotherms were measured using 10 ± 2 mg powdered sample. The experimental temperature was set to 25 °C. The samples were dried at 95 °C under $\approx 10^{-3}$ Torr ≈ 0.133 Pa for 3h. Several pretests at high vacuum with a turbomolecular pump revealed sample loss in the sample chamber. After the drying, the samples were cooled down to 25 °C for 4h. The dry mass of the sample was related to the mass at the first 0.0 % r.h. stage ($m_{0\,\%\,r.h.}$). Each r.h. step was fixed in time (Table 5.5). The times were selected with respect to reach weight equilibrium since $\Delta m / \Delta t$ criterion was not applicable for clay minerals at high r.h. (for $\Delta m / \Delta t = 0.02$, the time to achieve this criterion was > 6 h).

The CEC$_T$ was used as material intrinsic properties for the visualization of the isotherms. Thereby, the water contents in H_2O per Na^+ were calculated with respect to the measured CEC$_T$. A deviation of the targeted and actually measured r.h. was determined to be ± 1 % r.h..

Table 5.5 Measurements conditions for DVS Vacuum system.

Target r.h. [%]	duration (adsorption) [min]	duration (desorption) [min]	water vapor flow [sccm]
0.0	240	240	0
0.5	30	30	1
5.0	30	30	5
7.3	30	30	5
14.0	30	30	10
20.8	30	30	20
27.5	30	30	20
34.3	30	30	30
41.0	30	60	40
47.8	60	60	40
54.5	60	60	50
61.3	60	60	60
68.0	60	60	70
74.8	60	60	70
81.5	60	60	80
88.3	120	120	80
95.0	240		90

5.5.2 Volumetric water vapor sorption

Additionally, measurements were performed on a volumetric water vapor sorption analyzer (Hydrosorb™-1000, Quantachrome Instruments). The resolution of the instrument is 0.005 mg sorbed water and water vapor sorption isotherms can be obtained in the temperature range from 20 °C to 40 °C. Adsorption isotherms are prepared by comparing volume versus equilibrium relative pressure for a known quantity of an adsorbable gas, such as water vapor (Lowell, 2006). Powders and solid samples can be measured. The system records data points when the pressure changes over a given time period by no more than a user defined value. The pressure changes are defined in terms of mmHg (Torr). The water vapor pressure at 25 °C is 23.776 mmHg (= 100 % r.h.). The pressure tolerance ($p_{tol.}$) is defined as maximum pressure change over the selected period of time. The time in tolerance ($t_{tol.}$) is the selected time over which the pressure tolerance is measured. The term time to achieve equilibrium (t_{EQ}) is the maximum of time allowed for equilibrium (Hydrosorb1000, Operating Manual, 2006).

Here, the samples were outgassed at 95 °C for 24 h under a residual pressure of 0.01 Pa and weighed afterwards. The outgassing conditions were chosen in terms of results of the STA (chapter 5.6) to avoid any irreversible temperature effects regarding the hydration properties of the sample. The pressure tolerance was set to 0.05 mmHg, $t_{tol.}$ was set to 60 s and t_{EQ} was 6 h.

5.6   Determination of hydration by STA

During dynamic thermal analysis samples were subjected to a defined temperature-time-program with either a defined heating rate (dynamic) or a constant temperature (isothermal). During thermal treatment, minerals and rocks undergo several thermal reactions (e.g. dehydration, dehydroxylation, decomposition, oxidation, phase transition and recrystallization) providing diagnostic properties for the identification of mineral phases (Emmerich, 2010; Smykatz-Kloss, 1974b). In general, thermal analysis (TA) comprises a group of methods, which are presented in the following sections considering the current IUPAC Recommendations of the International Confederation for Thermal Analysis and Calorimetry (ICTAC) Nomenclature of thermal analysis (Lever et al., 2014):

Thermogravimetry (TGA): A technique where the change in weight is recorded during a defined temperature-time program in a clearly defined environment.

Differential thermal analysis (DTA): A technique where the temperature difference between a sample and a reference (inert) material is measured. The temperature difference indicates modifications in the heat flow between the sample and furnace. These changes show thermal effects as deviations from the zero line, accordingly, whether a reaction requires heat (endothermic) or releases heat (exothermic).

Differential scanning calorimetry (DSC): The difference between the electrical powers into a sample and a reference material is measured by using the DSC technique. The measurement signal of thermal flow DSC is an electric voltage (thermal voltage) caused by the temperature difference. DSC determines the amount of energy required to compensate temperature differences due to thermal reactions of the sample. In contrast to DTA, DSC allows to determine the type of the reaction (endothermal or exothermal), the reaction heat and the specific heat capacities.

Evolved gas analysis (EGA): A commonly combined technique, which determines the nature and/or amount of gas or vapor.

Simultaneous thermal analysis (STA): STA is a combination of at least two thermal analysis techniques comprising e.g. TGA, DSC and EGA. In particular, STA simply means coupling of at least two thermal analysis

EGA has a high sensitivity to detect small amounts of evolved gases during thermal treatment (Emmerich, 2010). However, the results of TA are subjected to several factors, such as the selection of experimental parameters, sample preparation as well as the instrument arrangement (Emmerich, 2010; Mackenzie and Mitchell, 1962; Rouquerol et al., 2013; Smykatz-Kloss, 1974b). Coupling of devices, by means of STA, enhanced the information of TA results and enabled a comprehensive characterization of 2:1 layer silicates (Emmerich, 2010, 2013; Emmerich et al., 1999; 2009; Steudel and Emmerich, 2013; Wolters and Emmerich, 2007; Wolters et al., 2009). Nevertheless, standardized conditions for STA are still essential for reproducible data. For a more detailed introduction on equipment and experimental factors affecting the results of TA, comprehensive reviews and handbooks are available (Emmerich, 2010, and references herein).

In this study, the thermal reactions were determined with a STA 449 Jupiter from Netzsch linked to a quadrupole mass spectrometer (QMS 403 C, Aeolos, Netzsch). Evolved gases such as H_2O, CO_2 and SO_2 were recorded simultaneously with TG and DSC signals by MS. Here, STA was applied in various ways: (1) to determine the water content after storing the sample at defined r.h., (2) to observe the longtime stability of adsorbed water and (3) additionally used to gather information on the octahedral structure (see 5.3.7). To ensure reproducible starting conditions, an isothermal segment of 10 min at 35 °C preceded the dynamic segment. Unless stated otherwise, the general measurement conditions listed in Table 5.6 (A) were applied in all experiments presented in this thesis.

Table 5.6 Experimental parameters of STA measurements.

	parameter	agent	amount	unit
	crucible	Pt/Rh, with lid		
	reference	empty Pt/Rh crucible with lid		
standard conditions (A)	purging gas	synthetic air	50	mL/L
	protective gas	N$_2$	20	mL/L
	temperature range	isothermal	10' 35	°C
		dynamic	35 - 1100	°C
	heating rate		10	K/min
isothermal long-time measurements (B)	purging gas	N$_2$	50	mL/L
	protective gas	N$_2$	20	mL/L
	temperature range	isothermal	24 h 35	°C
		dynamic	35 - 400	°C
	heating rate		10	K/min
	sample form	powder (smectite, illite)	100	mg
		powder (vermiculite)	75	mg
		(loosely packed, no pressing)		

5.6.1 Thermal reactions of 2:1 layer silicates

An extensive variety of structural modifications in 2:1 layer silicates cause a variability in their thermal behavior. However, profound thermal reactions of non-swelling and swelling 2:1 layer silicates have comparable characteristic stages (Drits et al., 1995; Emmerich, 2010; Köster, 1993). In 2:1 layer silicates, four characteristic reactions occur: dehydration, dehydroxylation, decomposition and recrystallization (Emmerich, 2000, 2010). Depending on the type of the counterion in the interlayer and layer charge, 2:1 layer silicates release adsorbed and interlayer water up to 300 °C. At temperatures above 400 °C, dehydroxylation occurs as endothermic reaction. Depending on the bonding of hydroxyl groups in the octahedral sheet, the dehydroxylation has a different onset temperature. In general, the dehydroxylation temperature increases from Fe-OH to Al-OH to Mg-OH (Emmerich, 2010; Köster and Schwertmann, 1993). Accordingly, Fe-rich dioctahedral smecites like nontronites

dehydroxylate between 450 and 600 °C, Al^{3+}-rich smectites between 500 and 700 °C and trioctahedral species around 750 – 850 °C (Smykatz-Kloss, 1974a). Dehydroxylation is frequently followed by decomposition (endothermal) and recrystallization (exothermal) and can be observed at temperatures > 850 °C. In the case of trioctahedral species, the endothermal decomposition peak is commonly missing due an overlap with the dehydroxylation reaction.

5.6.2 Water content and dry weight

The precise determination of water content is crucial for a wide range of technical and geotechnical applications (Bittelli et al., 2012; Christidis, 2013; Kaufhold et al., 2015; Low et al., 1991; Murray, 2006b; Wagner, 2013). The probably most common static method of TA is the determination of water content and the loss of ignition by gravimetry (Emmerich, 2010). Therefore, samples are heated at a defined temperature 105 °C or 1100 °C for a given time period until weight equilibrium is reached. The mass loss is analyzed afterwards. For engineering scientists, the determination of gravimetric water content is defined in DIN 18121 and DIN-ISO-11465. In most cases, samples are heated at 105 °C for 24 h and analyzed by weighing them before and after heating. However, heating at 105 C will not dehydrate clayey materials or soils completely. The residual water content could be as high as 6 % (Kaden, 2012), which is due to the complexity of water binding mechanisms in 2:1 layer silicates (chapter 2).

Depending on the type of interlayer cation and layer charge, swelling 2:1 layer silicates and even illites release water up to 250 °C (Drits and McCarty, 2007; Środoń and McCarty, 2008). Vermiculites have a similar structure to that of smectites and, hence, the thermal behavior is comparable. In contrast to smectites, vermiculites exhibit two clearly separated dehydration peaks between 100 and 300 °C (Beyer and Graf von Reichenbach, 2002). These authors used a heating rate of 1 K/min and, accordingly, the dehydration peaks of the Na^+-saturated vermiculite shifted towards lower temperatures (50-75 °C and 125-210 °C). Two separated endothermal dehydration peaks are also observed for tetrahedral charged smectites (beidelites and saponites) saturated with bivalent cations (Smykatz-Kloss, 1974a). For Na^+ saturated smectites with increased layer charge a shoulder or even a small separate second dehydration peak can be observed at higher temperatures (Emmerich, 2010).

In the current work, STA was applied to determine the water content after storing the sample at different r.h.. The TG curve displayed the mass loss referred to the mass of the initial sample stored at given r.h.. The mass loss during dehydration (Δm_{DHD}) was calculated considering the weight loss during isothermal segment and the weight loss until in MS-signal (m/z = 18) no evolved water was observed. The corresponding temperature is designated as $T_{DHD,end}$. Δm_{DHD} is equal to the mineralogical water content (w_{min}), which is commonly used to express the water content related to the starting (wet) weight and calculated as follows.

$$w_{min}[\%] = \frac{m_{H_2O}}{m_w} \times 100 \qquad (5.6)$$

$$w_{min} \triangleq \Delta m_{DHD} \qquad (5.7)$$

The water content per dry mass (w_{GT}) is calculated as:

$$w_{GT}[\%] = \frac{m_{H_2O}}{m_d} \times 100 \qquad (5.8)$$

Both values can be converted to each other (equation 6 and 7).

$$\Delta m_{DHD}[\%] = \frac{w_{GT}[\%]}{100 + w_{GT}[\%]} \times 100 \qquad (5.9)$$

$$w_{GT}[\%] = \frac{\Delta m_{DHD}[\%]}{100 - \Delta m_{DHD}[\%]} \times 100 \qquad (5.10)$$

With m_w = weight of the wet sample; m_{H_2O} = weight of the released water and m_d = dry mass. Furthermore, w_{GT} was converted to the amount of H_2O per Na^+ by using the measured CEC_T as structural intrinsic property of the 2:1 layer silicates.

$$H_2O \: / \: Na^+ = \frac{\frac{w_{GT}[\%]}{M(H_2O)[^g/_{mol}]} \times 1000}{CEC_T[^{cmol(+)}/_{kg}]} \qquad (5.11)$$

In addition, w_{GT} as well as $H_2O \: / \: Na^+$ were compared to the values of the water vapor isotherms.

5.6.3 Isothermal long-term experiments

To determine the stability of adsorbed water isothermal long-time measurements were carried out at 35 °C (nominal). In order to avoid the oxidation of organic matter, N_2 was selected as purging and protective gas.

First, samples were stored at 53 % r.h. above a saturated $Mg(NO_3)_2$ solution. Equilibration was obtained after two weeks. After equilibration at 53% r.h. the samples were analyzed with STA. The general measurement conditions listed in Table 5.6 were used to obtain a full dehydration. Afterwards, Δm_{DHD} was calculated as described above. A further sample equilibrated at 53% r.h. was analyzed with STA using the measurement conditions listed in Table 5.6. The weight loss during 24 h isothermal measurements (Δm_{24hN2}) was determined and compared to the mass loss during full dehydration by calculating the percentage of Δm_{DHD}. The isothermal segment was followed by a dynamic segment and the evolved gases such as H_2O (m/z = 18) and CO_2 (m/z = 44) were recorded simultaneously with TG and DSC signals by MS. The corresponding weight loss during dynamic segment as displayed in Table 5.6 is designated as $\Delta m_{24hN2+DHD}$. Note the mass loss during dynamic segment ($\Delta m_{24hN2+DHD}$) was calculated considering $T_{DHD,end}$ until in MS-signal no evolved water was observed.

6 Material characterization

6.1 Mineralogical characterization

6.1.1 Smectites

Na$^+$-saturated samples showed d$_{001}$ peaks ranging from 12.3-12.6 Å dependent on ambient humidity and expanded with ethylene glycol (EG) solvation to 16.9-17.1 Å (Figure 6.1) and collapsed to 9.6-9.79 Å after heating to 550 °C (Table 6.1). BV-M0.2Na, BC-M0.2Na and SAz-M2Na were identified as dioctahedral smectite by a d$_{060}$ at 1.50 Å. SHc-0.2Na is a trioctahedral smectite, which was confirmed by the observed d$_{060}$ peak at 1.52 Å on the XRD pattern of the powdered sample (Figure 6.2).
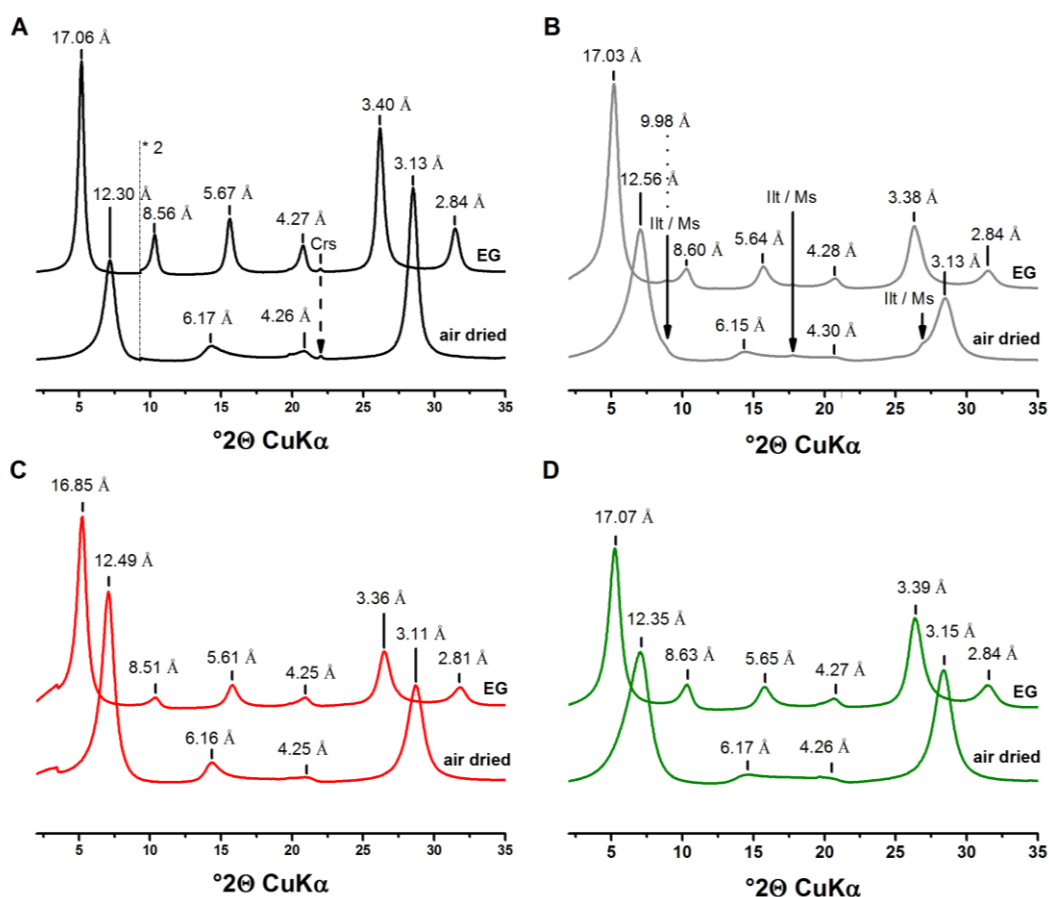
Figure 6.1 XRD pattern of air dried textured samples (A) BV-M0.2Na, (B) BC-M0.2Na, (C) SAz-M2Na and (D) SHc-0.2Na and after ethylene glycol solvation (EG); impurities were identified as Crs = low-cristobalite and Ilt/Ms = Illite/Muscovite.
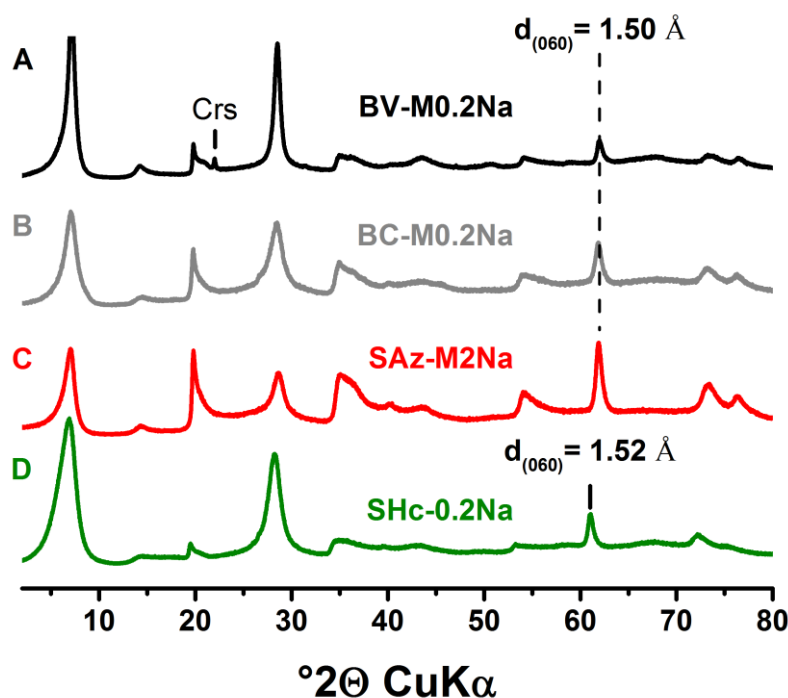
Figure 6.2 XRD pattern of powdered (A) BV-M0.2Na, (B) BC-M0.2Na, (C) SAz-M2Na and (D) SHc-0.2Na.

The oriented preparations revealed some crystalline impurities with Ilt/Ms in BC-M0.2Na most likely residues of muscovite identified in the coarser fractions with peaks d_{001} at 9.98 Å and d_{002} at 4.98 Å insensitive to ethylene glycol solvation and low-cristobalite (Crs) in BV-M0.2Na identified by a peak at 4.04 Å. Quantification of these impurities were done by (Delavernhe et al., 2015). The CV of 0.23-0.65 for all EG saturated samples revealed no interstratifications (Table 6.1). Sample SHc-0.2Na and SAz-M2Na showed no impurities, thus these samples can be regarded as pure clay minerals. Based on the non-exchangeable potassium content of BC-M0.2Na, 5 % of muscovite ($KAl_2(Si_3Al)O_{10}(OH)_2$) was quantified in BC-M0.2Na. 2 % of low-cristobalite was found in BV-M0.2Na.

Table 6.1 Peak positions and basal reflection rationality of XRD patterns.

Sample	d_{001} [Å]			d_{060} [Å]	Basal reflection rationality
	air dried	EG	550 °C	powder	CV
BV-M0.2Na	12.3	17.1	9.6	1.499	0.23
BC-M0.2Na	12.6	17.0	9.7	1.498	0.65
SAz-M2Na	12.5	16.9	9.6	1.498	0.53
SHc-0.2Na	12.4	17.0	9.5	1.517	0.64
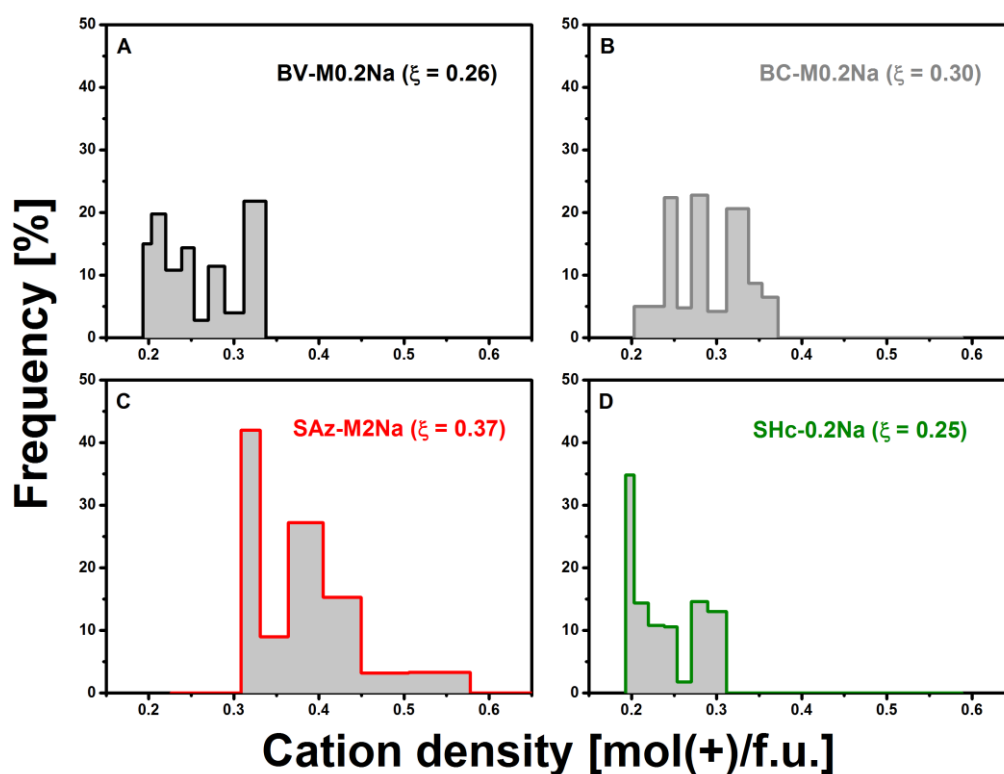
Figure 6.3 Layer charge distribution of (A) BV-M0.2Na, (B) BC-M0.2Na, (C) SAz-M2Na and (D) SHc-0.2Na.

The calculated cation density ranges between 0.19 and 0.34 mol(+)/FU for BV-M0.2Na and between 0.20 and 0.37 mol(+)/f.u. for BC-M0.2Na (Figure 6.3). Both in agreement with previous studies (Delavernhe et al., 2015; Steudel and Emmerich, 2013; Wolters et al., 2009). SAz-2Na and SHc-0.2Na showed both a bimodal distribution with a layer charge ranging from 0.31 to 0.58 mol(+)/f.u. and 0.19 to 0.31 mol(+)/f.u., respectively. A mean layer charge from 0.37 and 0.25 mol(+)/f.u., respectively, was measured in agreement with (Mermut and G., 2001).

A tetrahedral charge (ξ_T) from 38 and 23 % for BV-M0.2Na and BC-M0.2Na, respectively, was obtained (Table 6.3 and 6.4). In case of BV-M0.2Na, the effect of impurity correction (2% cristobalite content) resulted in an increase from 15 to 38% ξ_T. A muscovite content of 5% induced a decrease from 37 to 23% ξ_T for BC-M0.2Na. In contrast SAz-0.2Na and SHc-0.2Na have almost no ξ_T (Table 6.3). The main cation in the octahedral sheet of SHc-0.2Na is Mg^{2+}, which is partly substituted by Li^+ (Table 6.2 and 6.3).

Table 6.2 Chemical composition of the major elements [wt.%] (normalized to ignited weight and 100 %). Chemical position of all elements see Annex I.

Sample	SiO_2 (%)	Al_2O_3 (%)	Fe_2O_3 (%)	Li_2O (%)	MgO (%)	CaO (%)	Na_2O (%)	K_2O (%)
BV-M0.2Na	66.49	23.87	4.15		2.48	0.05	2.91	0.04
BC-M0.2Na	64.55	21.53	6.73		3.47	0.07	2.99	0.66
SAz-M2Na	67.56	19.99	1.79		6.50	0.02	4.08	0.05
SHc-0.2Na	65.86	0.77	0.41	1.29	28.80	0.10	2.59	0.13

Table 6.3 Structural formulae of Na^+-saturated < 0.2 µm and < 2 µm, respectively, smectites after impurities correction [mol/f.u.].

Sample	Tetrahedral cations		Octahedral cations					Interlayer cations			ξ eq/f.u.	Molar mass [g/mol]
	$^{IV}Si^{4+}$	$^{IV}Al^{3+}$	$^{VI}Al^{3+}$	$^{VI}Fe^{3+}$	$^{VI}Mg^{2+}$	Li^+	ΣOc	Ca^{2+}	Na^+	K^+		
BV-M0.2Na	3.90	0.10	1.61	0.19	0.22		2.02		0.26		0.26	372
BC-M0.2Na	3.93	0.07	1.39	0.32	0.33		2.04		0.29	0.01	0.30	376
SAz-M2Na	4.00		1.41	0.08	0.58		2.07		0.37		0.37	372
SHc-0.2Na	4.00		0.06	0.02	2.61	0.32	3.00		0.25		0.25	380

The octahedral sheet of BV-M0.2Na is almost purely *cis-vacant* (see chapter 6.3). With 38 % and 23 % tetrahedral charge of total charge BV-M0.2Na and BC-M0.2Na were classified as low-charged beidelitic montmorillonite, whereas SAz-M2Na was classified as medium-charged montmorillonite. The fitted MS-curves of evolved water (m/z = 18) during dehydroxylation for determining the ratio between the calculated areas for *cis*- and *trans*-vacant layers are displayed in Figure 6.4.

Table 6.4 Classification of dioctahedral smectites.

Sample	Layer charge [eq/f.u.]		Octahedral distribution $w_{tv/cv}$ [%]		Fe [%] of octahedral cations		Tetrahedral charge [%] of total charge		Mineral
BV-M0.2Na	Low	0.26	cv	0/100	-	9	Beidelitic	38	Montmorillonite
BC-M0.2Na	Low	0.30	cv/tv	44/56	Ferrian	16	Beidelitic	23	Montmorillonite
SAz-M2Na	Medium	0.37	cv/tv	70/30	-	-	-	-	Montmorillonite
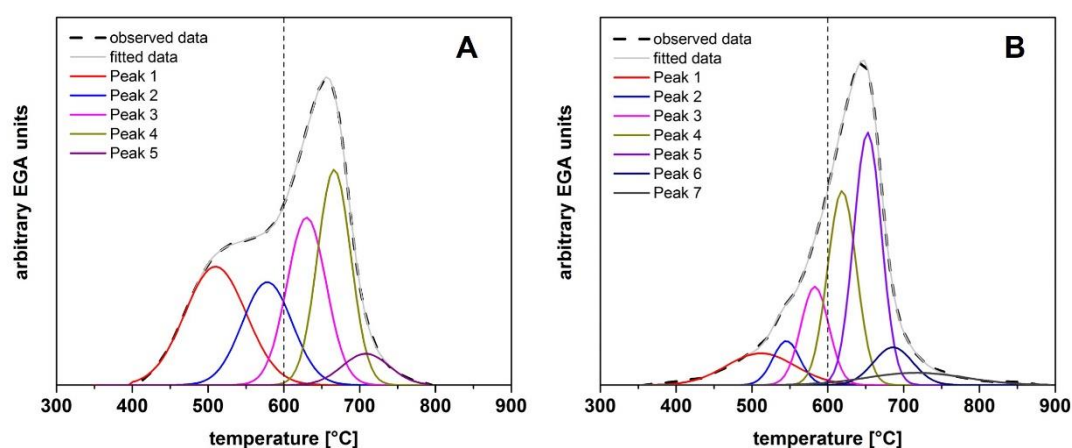
Figure 6.4 MS curves of the evolved water during dehydroxylation of cv/tv smectites: (A) BC-M0.2Na with 44% cv proportions and (B) SAz-M2Na with 70% cv proportions.

Exchange behavior and interlayer composition

The CEC_T of the Na+-exchanged smectites ranging from 76 to 130 cmol(+)/f.u. and a homoionic saturation between 96 and 99% was achieved (Table 6.5).

Table 6.5 CEC_T of Na+-saturated smectites measured at pH ≈ 7, CEC_P is derived from the structural formulae. The CEC measurement uncertainties were set to 2% of the measured values.

Sample	CEC_T [cmol(+)/kg]	CEC_p [cmol(+)/kg]	$\Delta CEC_T - CEC_P$ [cmol(+)/kg]	homoionic saturation [%]
BV-M0.2Na	89 ± 2	70 ± 2	19	98
BC-M0.2Na	90 ± 2	80 ± 2	10	96
SAz-M2Na	130 ± 3	100 ± 2	30	99
SHc-0.2Na	76 ± 2	66 ± 2	10	96

6.1.2 Vermiculite

VT-2Na was classified as a trioctahedral vermiculite and characterized in detail by (Steudel et al., 2009). They quantified 14 % phlogopite and 2 % calcite in VT-2Na. In contrast to smectite samples, VT-2Na required a longer reaction time for the complete exchange with alkylammonium (> 1 month) and, thus, the rapid mean layer charge estimation was applied (Olis et al., 1990). The d_{001} peak observed at 22.8 Å in the pattern of the alkyammonium exchanged sample (chain length n_c = 12) showed a low-charged vermiculite with a layer charge of 0.70 mol(+)/f.u., whereas the basal spacing d_{001} = 32.8 Å for n_c = 18 indicated the presence of high-charged domains (Steudel et al., 2009). A CEC of 159 cmol(+)/kg for VT-2Na was measured. The negative charge is mainly in the tetrahedral sheet due to exchange of Si^{4+} by Al^{3+}. The structural formula of VT-2Na was calculated from the chemical composition adjusted with respect to the impurities named previously.

$$Na_{0.70}(Si_{3.04}Al_{0.96})(Mg_{2.65}Fe_{0.32}Al_{0.03})O_{10}(OH)_2$$
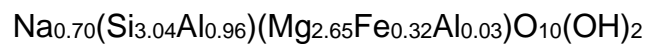
6.1.3 Illite

Ilt-0.2Na was classified as dioctahedral illite by a d_{060} at 1.50 Å (Figure 6.5).
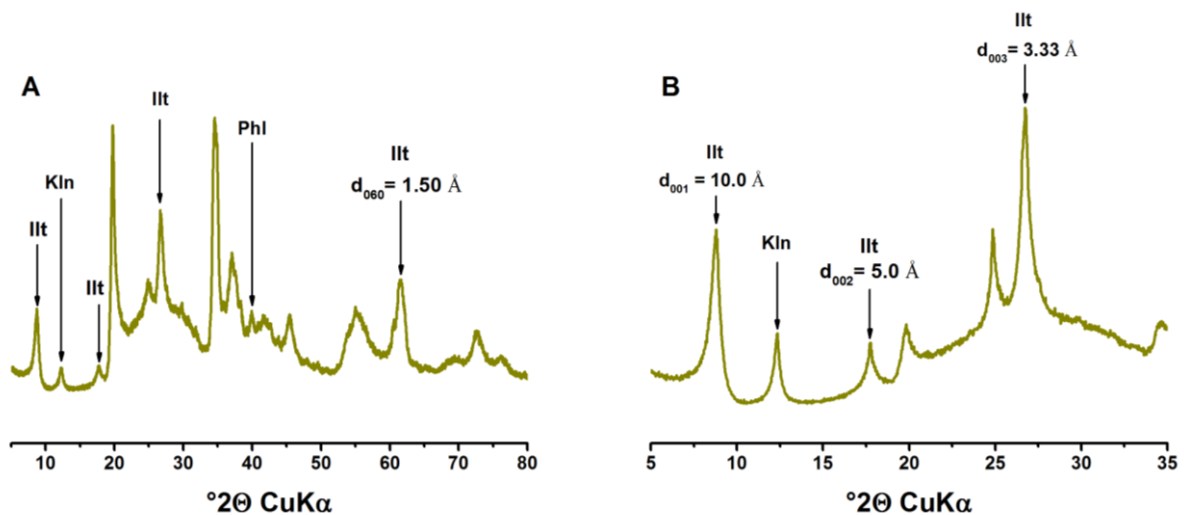
Figure 6.5 XRD pattern of (A) powdered and (B) air dried textured sample of Ilt-0.2Na; impurities were identified as Kln = kaolinite and Phl = phlogopite. Ilt: characteristic illite peaks with increasing 2θ (001), (002), (003) and (060).

Table 6.6 Chemical composition of the major elements [wt.%] (normalized to ignited weight and 100 %).

Sample	SiO_2 (%)	Al_2O_3 (%)	$Fe_2O_3(t)$ (%)	MgO (%)	CaO (%)	Na_2O (%)	K_2O (%)
Ilt-0.2Na	54.95	24.36	9.30	3.78	0.46	0.63	6.52

The structural formula of Ilt-0.2Na was calculated from the chemical composition (Table 6.6) adjusted with respect to the impurities quantified by (Steudel, 2009). A CEC_T of 22 cmol(+)/kg for Ilt-0.2Na was measured. Accordingly, a layer charge of 0.68 mol(+)/f.u. was calculated.

$$Na_{0.09}K_{0.56}Ca_{0.03}(Si_{3.51}Al_{0.49})(Al_{1.30}Fe_{0.49}Mg_{0.21})O_{10}(OH)_2$$
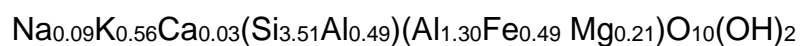
6.2   Particle size characterization

For single particles, the mean weighted equivalent diameter for BV-M0.2Na and BC-M0.2Na was measured to be 277 nm and and 118 nm by Delavernhe et al. (2015).

For VT-2Na, individual particles were easily identified by ESEM and the perimeter and basal area could be measured directly. The particle size distribution of VT-2Na ranged from 0.934 to 2.588 µm equivalent diameter, with a mean weighted equivalent diameter of 1.73 µm (see Figure 6.6).
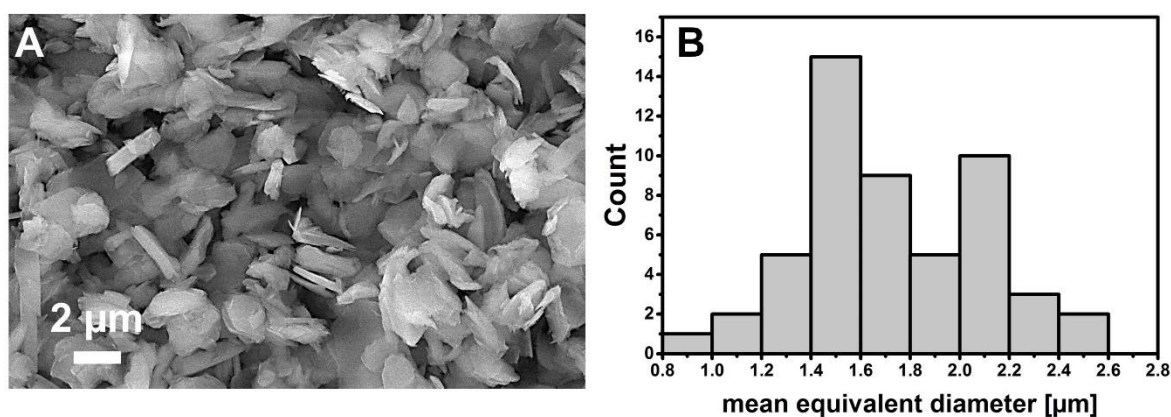
Figure 6.6 (A) Environmental scanning electron microscopy image of VT-2Na and (B) corresponding particle profile.

Considering the layer stacking model from Delavernhe et al. (2015), between 30-50 layers per stack were estimated for BV-M0.2Na. For BC-M0.2Na, SAz-M2Na and SHc-0.2Na, around 6-8 layers per stack were assessed. 20-30 layers per stack were estimated for VT-2Na and 7-9 for Ilt-0.2Na. The resulting $a_{s,edge}$ contribution ranged from 5 to 30 % for the illite and smectite samples. In contrast, VT-2Na has noticeable lower edge site contribution of 2 to 4 % (Table 6.7).
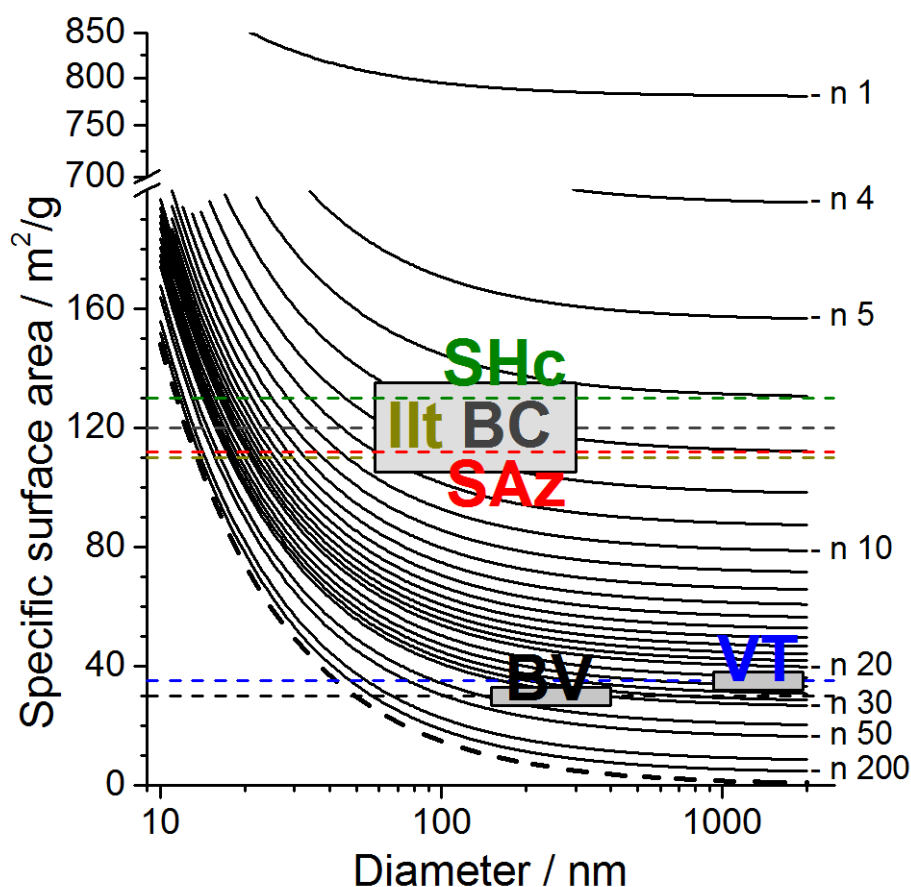
Figure 6.7 Specific surface area of quasi-crystalline layer stacks as a function of diameter, stack of layers, and $a_{s,edge}$ (dashed line) according to Delavernhe et al., 2015. Gray boxes of the selected 2:1 layer silicates with representative area for particle size diameter.

Table 6.7 Ar gas sorption parameters, diameter of single particles, layers per stack estimated by $a_{s,BET}$ (*), edge surface area estimation. (*) Values obtained by Delavernhe et al. (2015), (+) Poli et al. (2008), (-) Bosbach et al. (2004) and (Δ) Steudel (2009).

sample	$a_{s,BET}$	$d^{(a)}$	range of particle diameter	layers per stack n (*)	$a_{s,edge}$
	m²/g	nm	nm		%
BV-M0.2Na	31	277 (*)	150-400 (*)	30-50	20-30
BC-M0.2Na	118	118 (*)	100-300 (*)	6-8	5-15
SAz-M2Na	112	280 (+)	100-300 (+)	6-8	5-15
SHc-0.2Na	130	220 (-)	50-400 (-)	6-8	5-15
VT-2Na	35	1730	1000-2500	20-30	2-4
Ilt-0.2Na	110	n.d.	50-420 (Δ)	7-9	5-30

(a) Equivalent mean weighted diameter calculated from the area.

To support the results from gas adsorption analysis and to determine the stack height of the selected powder particles after equilibration at 85 % r.h., peak-shape analysis of the XRD patterns were done. Differences in peak width resulted from different size of the CSD. For lower number of layer per stack the width of the XRD peaks became broader and were calculated by the Scherrer equation (see chapter 5.3.1). Due to the turbostratic arrangement of the smectites particles, the average CSD thickness of the smectite samples was clearly found below the measured particle size (Table 6.7 and 6.8). In contrast, the layers per stack estimated from the CSD of VT-2Na was above the values calculated from the $a_{s,BET}$, which resulted from its ordered stacking sequences of layers.

Table 6.8 Mean CSD thickness, the basal spacing d_{003} at 2W state with resulting layers per stack of the selected 2:1 layer silicates.

sample	$3 \times d_{003}$ at 85 % r.h.	L	layers per
	Å	Å	stack n
BV-M0.2Na	15.35	80 ± 10	5-6
BC-M0.2Na	15.45	70 ± 10	4-5
SAz-M2Na	15.40	70 ± 10	4-5
SHc-0.2Na	15.48	50 ± 10	3-4
VT-2Na	14.85	500 ± 30	32-36
Ilt-0.2Na (*)	10.00	15 ± 5	1-2

(*) the basal spacing d_{002} at room temperature was used for calculation.

6.3   Thermal reactions
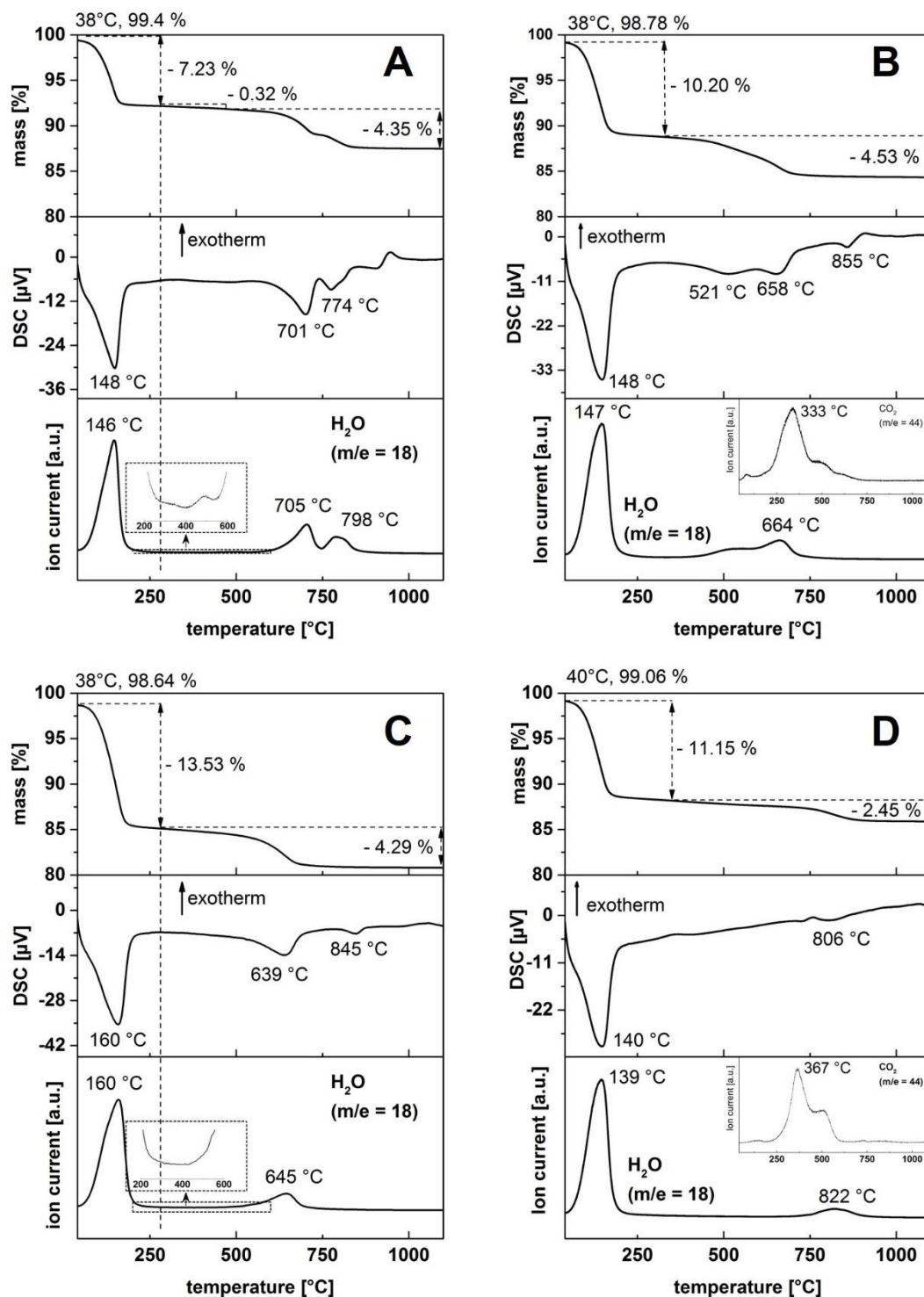
Figure 6.8 TG (top), DSC (middle) and MS curve of evolved water (m/z = 18) (bottom) during STA of (A) BV-M0.2Na, (B) BC-M0.2Na, (C) SAz-2Na and (D) SHC-0.2Na stored at 53 % r.h. (heating rate 10 K/min). Inlet windows inside the MS curve of evolved water illustrate the end of dehydration in (A) and (C) and CO_2 signal (m/z = 44) in (B) and (D).

BV-M0.2Na

The STA results of BV-M0.2Na stored at 53% r.h. shows a full dehydration at 280 °C associated with a mass loss of 7.23% (Figure 6.8 A). Including the mass loss during the isothermal heating Δm_{DHD} was calculated to 7.83% and w_{gt} was calculated to 8.50 %. Dehydroxylation of BV-M0.2Na occurred at 705 °C as endothermic reaction. As usual for homoionic Na^+-exchanged smectites, another endothermic reaction was observed at 774 °C correlated to the shattering of hollow silicate spheres and their sudden release of trapped evolved water (Emmerich, 2000; Emmerich et al., 2017). Based on the CEC_T of 89 cmol(+)/kg the water content resulted in 5.3 H_2O molecules per Na^+ cation.

BC-M0.2Na

Similar to the STA results of BV-M0.2Na, BC-M0.2Na stored at 53% r.h. shows a full dehydration at 280 °C associated with a mass loss of 10.20% (Figure 6.8 B). Including the mass loss during the isothermal heating Δm_{DHD} was calculated to 11.42% and w_{gt} was calculated to 12.89 %. In both samples BV-M0.2Na and BC-M0.2Na an endothermic reaction at 148 °C is associated with the release of adsorbed water. Based on the CEC_T of 90 cmol(+)/kg the water content resulted in 7.95 H_2O molecules per Na^+ cation. Dehydroxylation of BC-M0.2Na occurred at 664 °C as endothermic reaction with a shoulder near 530 °C. Whereas the doublet for dehydroxylation indicated a mixture of *cv* and *tv* octahedral sites in BC-M0.2Na, BV-M0.2Na is almost purely *cis-vacant* (Table 6.4). Decomposition occurred at 855 °C followed by a recrystallization at 906 °C.

SAz-2Na

STA results of SAz-M2Na stored at 53% r.h. shows a full dehydration at 280 °C associated with a strong endothermic reaction at 160 °C and mass loss of 13.53% (Figure 6.8 C). Δm_{DHD} was calculated to 14.89% and w_{gt} was calculated to 17.50 %. Based on a CEC_T of 130 cmol(+)/kg the water content resulted in 7.5 H_2O molecules per Na^+ cation. The decomposition of SAz-M2Na was observed at 845 °C and its *cv/tv* proportions were calculated to be 70/30 (Table 6.4 and Figure 6.4).

SHC-0.2Na

STA results of the trioctahedral SHc-0.2Na stored at 53 % r.h. shows a full hydration at 270 °C and a mass loss of 11.15% (Figure 6.8 D). Including the mass loss during the isothermal heating Δm_{DHD} was calculated to 12.09% and w_{gt} was calculated to 13.75 %. Based on the CEC_T of 76 cmol(+)/kg the water content resulted in 10 H_2O molecules per Na$^+$ cation. Dehydroxylation of SHc-0.2Na was observed by a broad endothermic reaction at 806 °C.
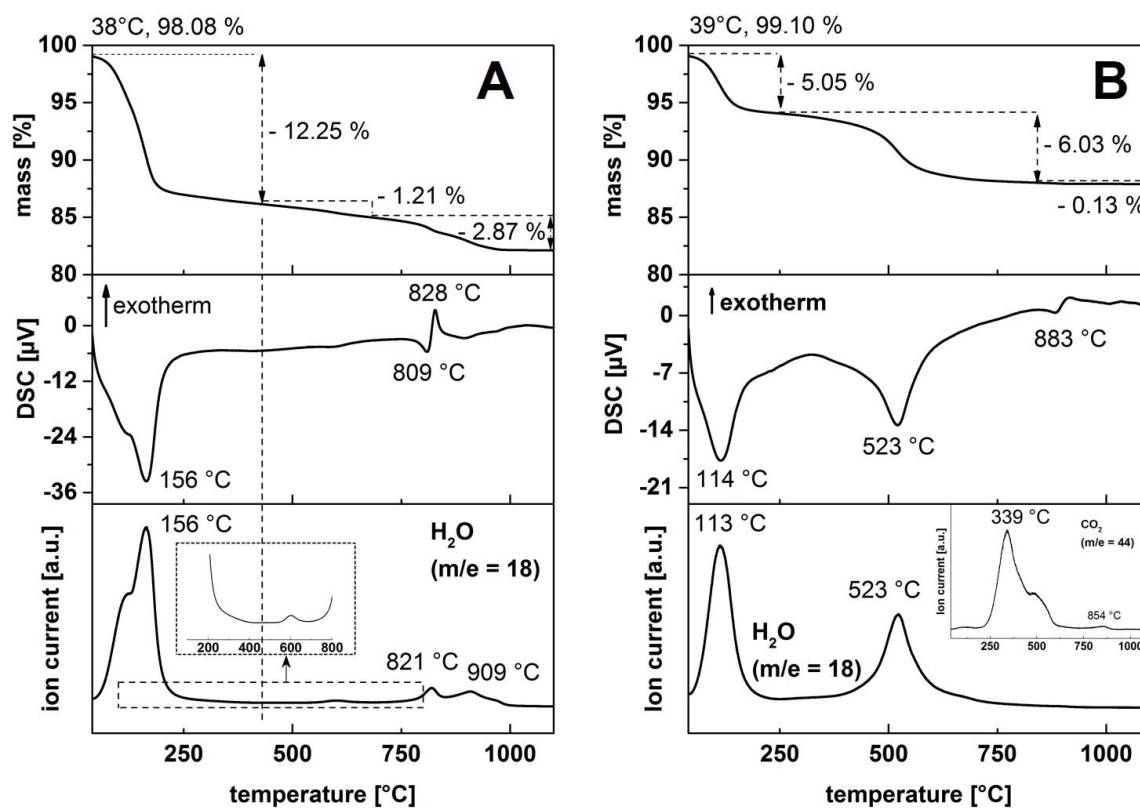
Figure 6.9 TG (top), DSC (middle) and MS curve of evolved water (m/z = 18) (bottom) during STA of (A) VT-2Na and (B) Ilt-0.2Na stored at 53 % r.h. (heating rate 10 K/min). Inlet windows inside the MS curve of evolved water illustrate the end of dehydration in (A) and CO_2 signal (m/z = 44) in (B).

VT-2Na

A full dehydration was observed at 430 °C for VT-2Na (Figure 6.9 A). Dehydroxylation of VT-2Na was observed at 821 °C followed by exothermal recrystallization at 828 °C indicating an iron-rich vermiculite (Figure 6.9 A, middle graph). The MS-curve of H_2O showed a second broad peak between 900 and 1000 °C indicating a similar process as proposed for Na^+-saturated smectites. The first large endothermic reaction at 156 °C is associated with the stepwise release of adsorbed water.

Ilt-0.2Na

Two maxima in the MS curve of water (m/e = 18) were observed at 113 and 523 °C. Both are correlated to endothermic reaction (Figure 6.9 B). The first one at 113 °C can be assigned to the release of adsorbed water. The second one at 523 °C showed the dehydroxylation of the *tv* octahedral sheet. No *cis-vacant* proportion was identified. The MS curve of CO_2 (m/e = 44) showed a maximum at 339 °C with a subsequent stepwise release of CO_2. This reaction was associated with the stepwise decomposition of glycerol, as verified by temperature controlled FTIR measurements (see chapter 4.2.1). Another small peak at 854 °C during CO_2 release was observed. This reaction is assigned to the decomposition of a carbonate. Assuming a pure calcite impurity in Ilt-0.2Na, the mass loss of 0.13% is correlated to 0.06% $CaCO_3$ and, accordingly, cannot be proved by XRD. The decomposition and recrystallization of Ilt-0.2Na occurred at 883 and 915 °C. In addition, the STA results of the initial sample stored at 53% r.h. shows a full dehydration at 250 °C associated with a mass loss of 5.05%. Including the mass loss during the isothermal heating Δm_{DHD} was calculated to 5.95% and w_{gt} was calculated to 6.33 %. Based on the CEC_T of 22 cmol(+)/kg the water content resulted in 16 H_2O molecules per Na^+ cation.

7 Study of hydration by XRD, vapor sorption and thermal analysis

7.1 Abstract

Hydration of 2:1 layer silicates is influenced by many factors such as layer charge, charge location, hydration properties of interlayer cations, surface properties and particle size distribution with resulting surface area. For a better understanding of hydration behavior of clay minerals, swellable and non-swellable 2:1 layer silicates are compared with respect to layer charge, charge location and particle size properties using water vapor sorption experiments, simultaneous thermal analysis (STA) and X-ray diffraction (XRD). XRD patterns were used to determine differences in hydration states for adsorption-desorption isotherms. In order to detect the respective number of H_2O molecules per Na^+ of each r.h. the values were collected on the desorption branch of the water vapor sorption isotherms. At 53 % r.h., the corresponding water contents ranged between 5.9 and 10 H_2O / Na^+ and implied that 1W state can even exist at water contents above 6 H_2O / Na^+. Results obtained by water adsorption gave an overview by mean of a qualitative and quantitative information of water sorption taken up by the 2:1 layer silicates. On the desorption branches of all swellable 2:1 layer silicates, clear changes between 6 and 4 H_2O / Na^+ in the gradient could be assigned. These transitions could not be clearly identified on the adsorption branches of the smectite isotherms. Therefore, kinetic data retrieved from the adsorption isotherms helped to discriminate between different hydration states in 2:1 layer silicates. In addition, the weight loss of the isothermal treatment showed that during 24 h at 35 °C (nominal) under N2 purging none of the samples were completely dehydrated. The residual moisture content for all materials could be assigned to a tightly bound water with a resulting higher releasing temperature. For dioctahedral smectites a trend with increasing layer charge was observed. Increasing the layer charge resulted in a higher amount of residual moisture. For the low-charged SHc-0.2Na, the results implied that a trioctahedral structure leads to a more stable water binding, which was observed as a higher content of residual moisture. A tightly bound water was also observed for the Na^+-exchanged illite sample indicating that the exchangeable cations of Ilt-0.2Na hydrate in the same manner as in the smectites samples.

7.2   Introduction

Most of the technical processes involving smectites are based on reactions that take place in the interlayer (Brigatti et al., 2013). The hydration in the interlayer is controlled by factors such as the hydration of the interlayer cations, the interaction of H_2O molecules with the basal surface and the interlayer cation and the water activity in the clay mineral-water system (Güven, 1992). Understanding of the hydration process at the molecular scale has a high impact on a great diversity of applications and thus for a broad range of communities from chemists, material scientists to geoscientists and engineers.

One of the most important type of clays are bentonites. Bentonites mainly consist of low-charged swellable clay minerals called smectites. Within the smectite group montmorillonites are the most abundant minerals. Montmorillonites, the most heterogeneous phyllosilicates, are built of dioctahedral 2:1 layers (Wolters et al., 2009). Isomorphic substitutions mainly in the octahedral sheet (Al^{3+} substituted by Mg^{2+} and Fe^{3+}/Fe^{2+}) and ancillary in the tetrahedral sheet (Si^{4+} substituted by Al^{3+}) generate a negative layer charge and a huge structural variety. Exchangeable cations such as Na^+ in the interlayer compensate the charge to obtain electroneutrality.

The crystalline swelling of 2:1 layer silicates is commonly described by XRD, where the main focus lies in the evolution of the basal-spacing (d_{001}) value under variable r.h. (Dazas et al., 2014; Ferrage et al., 2011). The reversible swelling mechanism is induced by hydration of the exchangeable and charge-compensating counterions in the interlayer of swellable 2:1 layer silicates leading to discrete water layers which increase in number from one to three (Emmerich et al., 2015). These discrete hydration states are known as mono-hydrated (1W, layer thickness ≈ 11.6-12.9 Å), bi-hydrated (2W, layer thickness ≈ 14.9-15.7 Å) and tri-hydrated (3W, layer thickness ≈ 18-19 Å) (Dazas et al., 2014; Ferrage et al., 2005a). The latter is being less common. Many studies have recognized that these hydration states usually coexist in smectites, even under controlled conditions. Using XRD, such a coexistence is shown by the irrationally of the 00l reflections as well as by peak profile asymmetry at the transition between two hydration states. However, there is a lack in quantitative understanding of stable hydration states in dependence of layer charge together with charge distribution over tetrahedral and octahedral sheets.

The aim of this chapter is to investigate the water vapor de- and adsorption behavior of 2:1 layer silicates using XRD, dynamic thermal analysis, static and dynamic vapor sorption experiments and relate these results to the intrinsic properties (e.g. layer charge, charge location, octahedral composition and particle size) of dioctahedral and trioctahedral 2:1 layer silicates. Additionally, the question has been raised of whether a full dehydration can be observed using only dry nitrogen at ambient conditions. For this purpose, isothermal long-time measurements were carried out at 35 °C (nominal).

A common technique to study the sorption of water vapor is the examination of water vapor sorption isotherms (Bérend et al., 1995; Cases et al., 1992; 1997). In contrast to a non-polar adsorbate such as Ar, the determination of ad- and desorption isotherms are rather complicated since water vapor induce swelling and, accordingly, can only be interpreted with the help of further analysis such as XRD (Ferrage, 2016) or further spectroscopic information (Johnston et al., 1992). In addition, no true $a_{s,BET}$ values can be derived using water vapor adsorption isotherms (Van Olphen, 1970). The first problem of the interpretation of water vapor sorption isotherms is to define an initial state reached after outgassing the sample, prior to its analysis. (Bérend et al., 1995) showed for a dioctahedral smectite (Na^+-, Li^+-, K^+-, Rb^+- and Cs^+-exchanged form) that the initial dry state (outgassing at 110 °C for 24 h and a residual pressure of 0.1 Pa) vary in function of the interlayer cation. Nevertheless, among the most research on clay water ad- and desorption, the amount of adsorbed water is illustrated as mmol H_2O / g - or as mg / g of dried clay (Bérend et al., 1995; Cases et al., 1992; 1997; Dazas et al., 2015; Ferrage et al., 2011). Here, the CEC was used as material intrinsic property for the visualization of the isotherms. Thereby, the water contents in H_2O per Na^+ can be directly correlated to the material properties and probe the water arrangement in the interlayer of swellable 2:1 layer silicates. However, this kind of illustration imply that all exchangeable cations hydrate in the same manner. But, due to non-exchangeable or non-accessible interlayer cations and exchangeable cations at the edges, water content correlates more strongly with the exchangeable cations than with layer charge (Kaufhold, 2006; Kaufhold et al., 2011). This correlation is even more pronounced for small particles with an increased contribution from edge sites to CEC (Emmerich, 2010).

Concerning the calculations of Emmerich et al., 2015 the dehydration temperature increases with the layer charge. Their calculations were based on two similar unit cells

that differ from each other concerning the chemical potential of Na^+. The stoichiometric description of these unit cells given by $[Na_1(Si_{16})(Al_7Mg_1)O_{40}(OH)_8]$ corresponding to a low chemical potential of Na^+, $[Na_2(Si_{16})(Al_6Mg_2)O_{40}(OH)_8]$ corresponding to a high chemical potential of Na^+ (Emmerich et al., 2015). Accordingly, their model systems have a layer charge of 0.25 and 0.5 eq/f.u., respectively. According to their results, a water free surface can be reached by the low-charged model at ambient temperatures with reduced partial pressure of H_2O, while the high-charged model needs higher temperature to fully dehydrate.

The purpose of the present chapter was to investigate the water vapor de- and adsorption behavior of 2:1 layer silicates. First, XRD patterns were used to determine differences in hydration states. Second, the water vapor adsorption isotherms of a trioctahedral vermiculite and a fine-grained illite will be compared to those of the smectite samples. With the help of kinetic data retrieved from the adsorption isotherms a discrimination between different hydration states in 2:1 layer silicates will be discussed. In addition, isothermal long-time measurements were carried out at 35 °C (nominal) to observe the stability of adsorbed water under N_2 purging. Finally, a low-charged dioctahedral smectite sample with highly turbostratic disorder were compared to a vermiculite sample with a homogeneous hydration of the interlayer cation. Thereby, dynamic thermal analysis was applied to determine the water content after storing the samples at defined r.h., thus, the true water content for each sample was determined after full dehydration. Thereby, the stepwise release of interlayer water will be discussed using STA..

7.3   Material and methods

Material

Homoionic Na^+-saturated samples of three dioctahedral smectites, one trioctahedral smectites, a trioctahedral vermiculite and dioctahedral illite were studied and compared with respect to layer charge, charge location (di- vs. trioctahedral), octahedral structure (cis- vs. trans vacant) and geometrical factors (e.g. particle size properties). The materials have been characterized in chapter 6.

Methods

XRD patterns were recorded from powdered homoionic Na^+-saturated samples stored at different r.h. (see chapter 5.3.1). STA was applied to determine the water content after storing the sample at defined r.h. (see chapter 5.6.2). Additionally, measurements were performed on a dynamic vapor sorption (DVS) instrument (5.5.2). Finally, kinetic data retrieved from the adsorption isotherms were used to differentiate the dynamics in 1W and 2W state.

In the second part of this chapter, isothermal long-time measurements were carried out at 35 °C (nominal) to observe the stability of adsorbed water under N_2 purging (5.6.3).

Finally, BV-M0.2Na and VT-2Na were compared in respect to their dehydration behavior.

7.4   Results and discussion

Water content and hydration state

In the following, XRD patterns of BV-M0.2Na and VT-2Na between 2 and 50° 2θ are shown in Figure 7.1 as representative samples to show a highly turbostratic disordered arrangement and a semi-ordered stacking sequence of layers. XRD pattern of BC-M0.2Na, SAz-2Na and SHc-0.2Na in function of the r.h. can be found in the appendix.

For BV-M0.2Na, XRD pattern at 53 % r.h. (d_{001} = 12.4 Å) correspond to 1W and at 75 and 86 % r.h. (d_{001} = 15.15 and 15.45 Å, respectively) to 2W states, whereas d_{001} = 10.8 Å was observed between 0W and 1W state at 11 and 43 % r.h. (Figure 7.1 A). In contrast to VT-2Na, strongly irrational series of basal reflections were observed for the smectite sample (ξ / χ_i) between 0.34 and 0.96). The two strong asymmetrical reflection peaks, observed at ≈ 20 and 35 °2θ CuKα, show the turbostratic disorder in BV-M0.2Na over the whole r.h. range. In addition, the calculated CV of 7.11 at 11 and 43 % r.h. indicated a high deviation from rationality of the 00l reflection series. Interestingly, the CV at 53 % r.h. indicated no random interstratification, whereas the CV at 75 and 86 % r.h. increased to 1.6 and 0.9, respectively (Table 7.1).

On XRD pattern of VT-2Na stored at different r.h. a high rationality of the basal reflections was observed (Figure 7.1 B). The low standard deviation and the CV indicated a homogeneous hydration over the whole humidity range for the vermiculite sample. At 11 % and 43 % r.h., d_{001} was observed between 11.9 and 12.2 Å characteristic for an 1W hydration state (Ferrage, 2016). At 53 % r.h., two peaks at 12.21 and 14.70 Å were observed in the low-angle region < 10 °2θ CuKα indicating the coexistance of 1W and 2W layers. Further increase of the r.h. resulted in an upward shift of all basal reflections and new reflections appeared at 75 and 86 % r.h. (Figure 7.1 B). Here, d_{001} was observed at 14.84 Å characteristic for a 2W hydration state. Accordingly, the transition between 1W and 2W state were observed between 43 and 75 % r.h.. This is consistent with that reported by Lanson et al. (2015) for Na$^+$-saturated Santa Olalla vermiculite. However, these authors used textured samples and showed stable 1W state for r.h. ranging from 10 to 40 % and 2W state dominated from 60 to 100 % r.h. (Lanson et al., 2015).
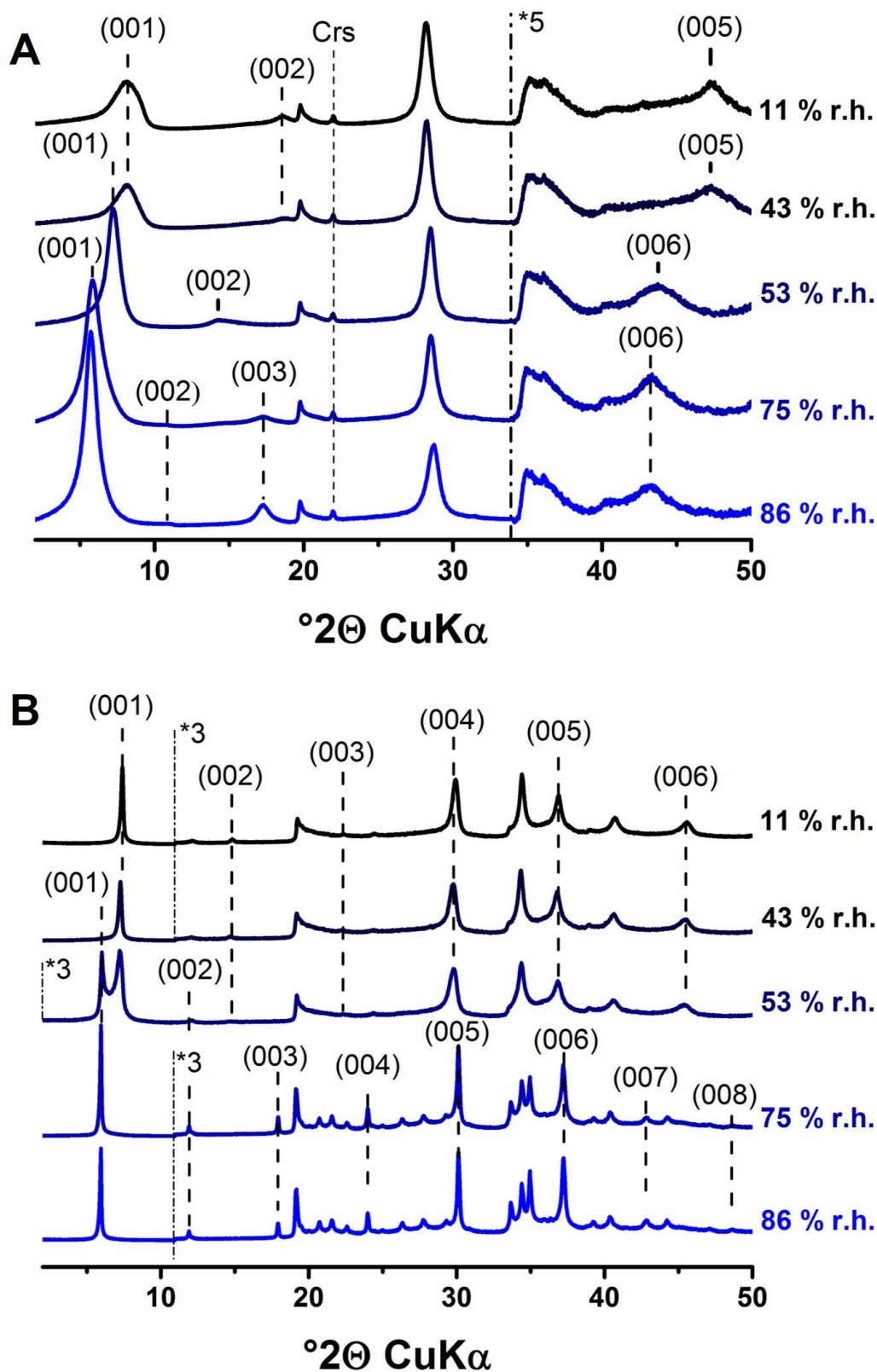
Figure 7.1 XRD patterns of powdered (A) VT-2Na and (B) BV-M0.2Na as a function of r.h.. For VT-Na, high-angle intensities are scaled up by a 3× factor compared to the 2-11 °2θ CuKα angular range. For XRD patterns stored at 53 % r.h. (A) the whole angular range was scaled up by 3× factor. For BV-M0.2Na, high-angle (34-50 °2θ CuKα) intensities are scaled up by a 5× factor. Crs: cristobalite.

Table 7.1 Position and rationality of the evolution of basal reflection series $d_{(00l)}$ as a function of r.h. for VT-2Na and BV-M0.2Na. Note: For calculation of the coefficients of variation (CV) the (001) reflection was omitted as recommended by (Bailey, 1982).

sample	VT-2Na			BV-M0.2Na		
r.h. [%]	$d_{(001)}$ [Å]	ξ / χ_i	CV	$d_{(001)}$ [Å]	ξ / χ_i	CV
11	11.94	0.08 / 6	0.13	10.8	0.58 / 3	7.11
43	12.16	0.10 / 6	0.13	10.8	0.58 / 3	7.11
53	12.21/14.70	0.12 / 6	0.13	12.37	0.96 / 5	0.24
75	14.84	0.14 / 8	0.20	15.15	0.34 / 5	1.62
86	14.84	0.14 / 8	0.20	15.45	0.32 / 5	0.90

Indeed, there is a possible overestimation when solely determining the d_{001}, especially at high basal spacings (Ferrage et al., 2010b). However, in order to compare the respective hydration states with water vapor isotherms the d_{001} was used. Decreasing the r.h. resulted in a decreased basal spacing d_{001}, except for Ilt-0.2Na, which showed no changes in the basal spacings. For the samples equilibrated at 86 % and 75 % r.h., the d_{001} spacings for BV-M0.2Na, BC-M0.2Na, SAz-M2Na and VT-2Na were obained between 15.6 and 14.85 Å corresponding to the 2W hydration state. For SHc-0.2Na equilibrated at 86 % r.h., d_{001} was observed at 15.8 indicating the transion to 3W hydration state. For the samples equilibrated at r.h. ≤ 53 %, the d_{001} spacings for BC-M0.2Na, SAz-M2Na and VT-2Na were obtained between 12.6 and 11.9 Å corresponding to a 1W hydration state.

Water vapor sorption isotherms

In order to detect the respective number of H_2O molecules per Na^+ of each r.h. the values were collected on the desorption branch of the water vapor sorption isotherms (Figure 7.3) and displayed in Table 7.2. It should be noted that the dry mass of the samples was related to the mass at the first 0.0 % r.h. stage ($m_{0 \% r.h.}$).

For all swellable 2:1 layer silicates equilibrated at 86 and 75 % r.h., the basal spacings showed at least a 2W hydration state and a corresponding water content ranged between 17.9 and 6.9 H_2O / Na^+ depending on the 2:1 layer silicate (Table 7.2). For the samples equilibrated 53 % r.h., the d_{001} was correlated to a 1W hydration state and

the correlated water contents were found to range between 5.9 and 10 H_2O / Na^+. A 1W state was also observed at r.h. ≤ 53 %, excluding BV-0.2Na and Ilt-0.2Na.
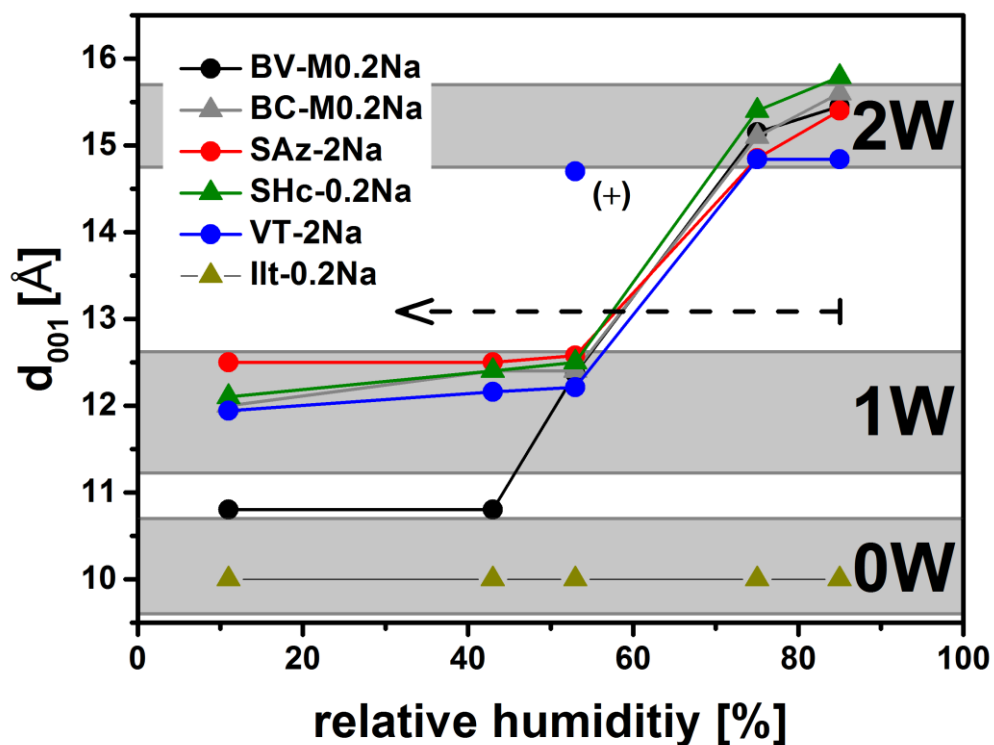
Figure 7.2 Evolution of the basal sapacing d_{001} as a function of the relative humidity. (+) Second observed peak for VT-2Na at 53 % r.h. Arrow with dashed line indicates the direction of the experiment. Limits of 0W, 1W and 2W hydration state were choosed according to Ferrage, 2016.

Table 7.2 Water content H_2O / Na^+ in function of the r.h.. The dry mass of the samples was related to $m_{0 \% r.h.}$.

sample	BV-M0.2Na	BC-M0.2Na	SAz-M2Na	SHc-0.2NA	VT-2Na	Ilt-0.2Na
r.h. [%]	H_2O / Na^+	H_2O / Na^+	H_2O / Na^+	H_2O / Na^+	H_2O / Na^+	H_2O / Na^+
11	1.7	2.3	2.6	2.4	2.5	1.0
43	5.3	7.0	5.6	8.3	5.1	6.1
53	6.5	8.3	6.7	10.0	5.9	8.1
75	10.7	11.9	9.6	14.8	6.9	18.7
86	12.3	14.2	11.2	17.9	7.5	37.5

BV-M0.2Na

Continuous increasing of the r.h. resulted in increasing the number of H_2O per Na^+ (Figure 7.3). The adsorption of water vapor proceeded differently compared to the desorption branch and, hence, hysteresis was observed. Three different slopes could be identified in water adsorption. At low r.h. (from 0 % to 40 %), a nearly linear increase could be observed. The correlated water content ranged from 0 to 2 H_2O / Na^+. A first change of slope in the adsorption branch was observed at 40 % r.h.. Here, the water content changed from 2 to 4.5 H_2O / Na^+. At 60 % r.h., the slope changed significantly and reached a water content of 14 H_2O / Na^+ at 95 % r.h.. On the desorption branch, a first nearly linear decrease of water content was observed from a r.h. of 95 % to 80 % with a water content ranging from 14.5 to 11.5 H_2O / Na^+. At 55 % r.h., the water content decreased significantly to 6.7 H_2O / Na^+. Subsequently, an almost linear decrease of water content was observed again (from 48 % to 14 % with H_2O / Na^+ ranging from ≈ 6 to 4), followed by a drop with a resulting water content of 1 H_2O / Na^+ at ≈ 5 % r.h., where the isotherm closed and followed the same path as on the adsorption branch.

BC-M0.2Na

Between 0 % and 55 % r.h., a first nearly linear increase in water content could be observed, followed by a change in slope at ≈ 60 % r.h. and correlated water content of 6 H2O / Na+. A second change of slope in the adsorption branch was observed at ≈ 80 % r.h.. Here, the water content changed from 6 to 11.5 H2O / Na^+. At 95 % r.h., a highest water content of 16.5 H2O / Na^+ was achieved. On the desorption branch, a first nearly linear decrease of water content was observed from a r.h. of 95 % to ≈ 80 % with a water content ranging from 14.5 to ≈ 13 H_2O / Na^+. A transition point at ≈ 40 % r.h. was observed, followed by a linear decrease of water content (from 40 % to 15 % r.h with H_2O / Na^+ ranging from ≈ 7 to 3). At < 15 % r.h., a drop in water content was observed. The lowest water content was 0 H_2O / Na^+ at 0 % r.h.. and the isotherm was closed at ≈ 5 % r.h..

SAz-M2Na

A significantly larger hysteresis was observed for BV-M0.2Na compared to SAz-M2Na. Between 0 % and 40 % r.h., a first nearly linear increase in water content could be

observed, followed by a change in slope at ≈ 40 % r.h. and correlated water content of 4 H_2O / Na^+. A second change of slope in the adsorption branch was observed at ≈ 60 % r.h.. Here, the water content changed from 4 to 6 H_2O / Na^+. At ≈ 60 % r.h., the gradient changed significantly. At 95 % r.h., a highest water content of 12.7 H_2O / Na^+ was achieved. The desorption branch of the isotherm of SAz-M2Na exhibited a similar shape compared to one of BV-M0.2Na. First, the water content decreased nearly linear down to 6 H_2O / Na^+ at ≈ 50 % r.h.. A transition point at ≈ 50 % r.h. was observed, followed by a linear decrease of water content (from 50 % to 20 % r.h with H_2O / Na^+ ranging from ≈ 6 to 4). At < 20 % r.h., a drop in water content was observed. The lowest water content was 0.9 H_2O / Na^+ at 0 % r.h. (Figure 7.3 C).

SHc-0.2Na

The hysteresis observed on the water vapor sorption isotherm for SHc-0.2Na was similar to those of BC-M0.2Na. A marked change in the gradient at ≈ 5 % r.h. could be observed, followed by an almost linear increase from 5 % to ≈ 60 % r.h. with a corresponding water content from ≈ 1 to 8 H_2O / Na^+. At 95 % r.h., a highest water content of 21 H_2O / Na^+ was achieved. On the desorption branch, a first nearly linear decrease of water content was observed from a r.h. of 95 % to ≈ 80 % with a water content ranging from 21 to ≈ 16.5 H_2O / Na^+. A change in gradient was observed at ≈ 50 % r.h., followed by a linear decrease of water content (from 50 % to 15 % r.h with H_2O / Na^+ ranging from ≈ 9 to 3). At < 15 % r.h., a drop in water content was observed. The lowest water content was 0 H_2O / Na^+ at 0 % r.h.. and the isotherm was closed at ≈ 5 % r.h. (Figure 7.3 D).

VT-2Na

On the adsorption branch of the isotherm of VT-2Na a clear transition could be observed at 14 % r.h. (Figure 7.3 E). Here, the water content changed from 0 to 2.4 H_2O / Na^+, followed by an almost linear increase from 14 to 56 % r.h. and a corresponding water content from 2.4 to 3.7 H_2O / Na^+. At 60 % r.h., the slope changed significantly and reached a water content of 8.1 H_2O / Na^+ at 95 % r.h.. On the desorption branch, a first nearly linear decrease of water content was observed from a r.h. of 95 % to 40 % with a water content ranging from 8.1 to 5 H_2O / Na^+. At 45 % r.h., the water content decreased significantly to 3.5 H_2O / Na^+. Subsequently, an almost linear decrease of water content was observed again (from 35 % to 7 % with H_2O / Na^+

ranging from ≈ 3.5 to 2.3), followed by a drop with a resulting water content of 1 H_2O / Na^+ at ≈ 0 % r.h. (Figure 7.3 E).

Ilt-0.2Na

A significantly smaller hysteresis was observed for the water vapor isotherm of Ilt-0.2Na (Figure 7.3 F). According to the classification of Thommes et al. (2015), a hysteresis loop of type H3 could be assigned. On the adsorption and desorption branch an almost linear increase and decrease, respectively, of water content could observed between 0 and 75 % r.h.. Here, the water content increased up to 6.7% related to the dry mass at 0 % r.h.. Due to the low CEC of Ilt-0.2Na the amount of H_2O / Na^+ reached a value up to 54.

On the desorption branches of all swellable 2:1 layer silicates, clear changes between 6 and 4 H_2O / Na^+ in the gradient could be assigned. These transitions could not be clearly identified on the adsorption branches of the smectite isotherms. However, the results indicated that along these water vapor sorption isotherms from the montmorillonite and hectorite samples at least two hydration states (1W and 2W) with different hydration dynamics could be observed.
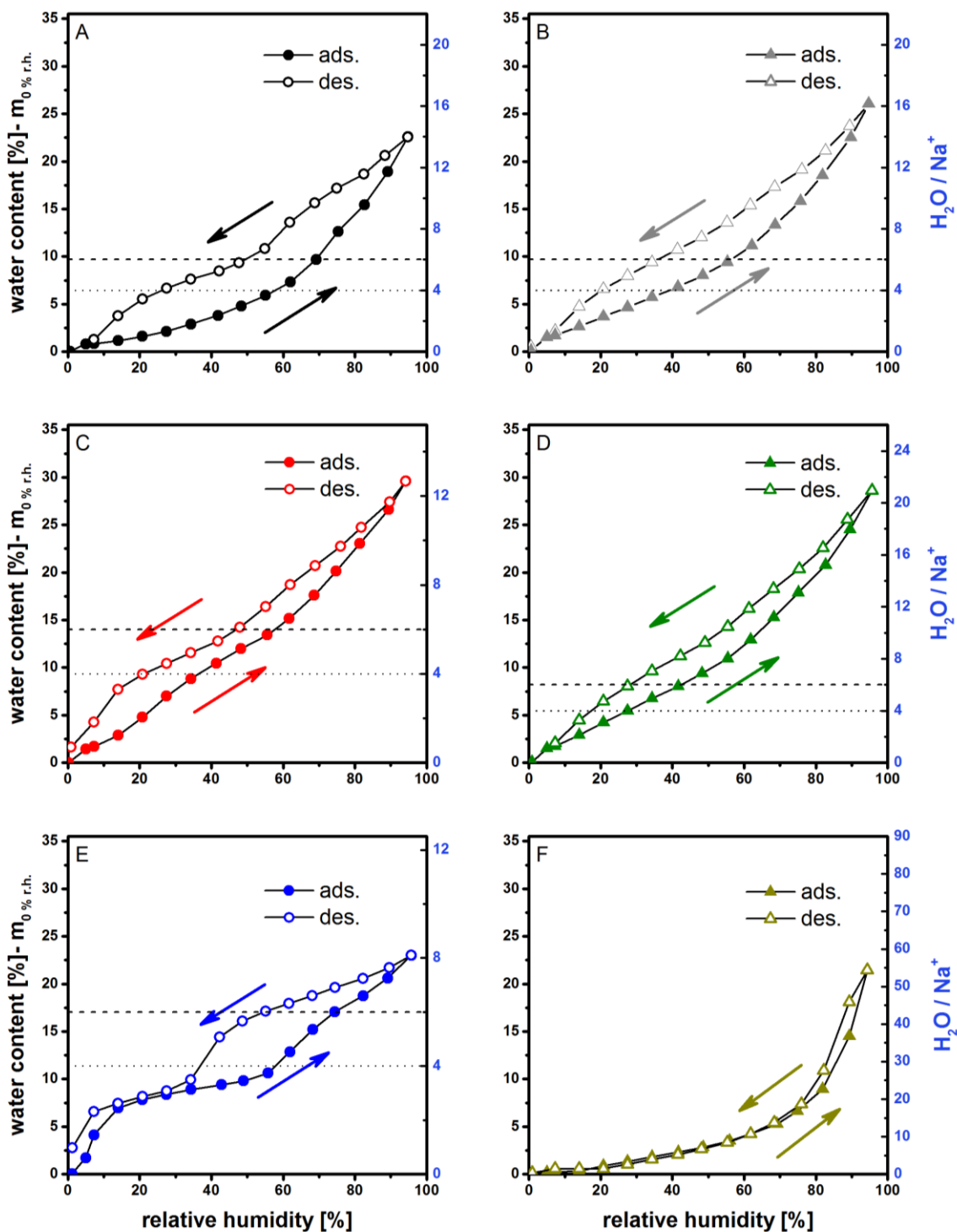
Figure 7.3 Water vapor sorption isotherms from (A) BV-M0.2Na, (B) BC-M0.2Na, (C) SAz-M2Na, (D) SHc-0.2Na, (E) VT-2Na and (F) Ilt-0.2Na at 25 °C. Arrows indicate the direction of the experiment. Dashed lines represent 6 H_2O / Na^+ and dotted lines 4 H_2O / Na^+.

Kinetic data retrieved from the adsorption isotherms

In order to gain a deeper understanding of the differentiation of 1W and 2W hydration state and how their transitions could be identified on the adsorption branches, water vapor sorption isotherms were recorded on a volumetric water vapor sorption analyzer. The time to achieve equilibrium of each r.h. step was observed below t_{EQ} and the equilibrium times Δt and the mass changes per equilibrated times were illustrated in Figure 7.4. The results of BV-M0.2Na and BC-M0.2Na are shown as representative samples of dioctahedral smectites. The recorded water vapor sorption isotherms were in good agreement with those shown in Figure 7.3. despite the influence of different outgassing conditions during the drying process.

In the water vapor adsorption isotherm of BV-M0.2Na, a slightly increasing gradient was observed between 0 and 60 % r.h., followed by an abrupt increase in the gradient (Figure 7.4 A). Here, the correlated water content changed from 4 to 6 H_2O / Na^+.

A similar trend could be observed on the adsorption branch of the water vapor isotherm of BC-M0.2Na (Figure 7.4 B). Here, a marked change in the gradient is obtained at ≈ 60 % r.h. with a corresponding water content of 7 H_2O / Na^+.

The transitions from dry state (vacuum) to 20 % r.h. as well as from 50 to 70 % r.h. were accompanied by an increase in the equilibration times (Figure 7.4 C, upper and middle graph). On the adsorption branch of the water vapor isotherm of VT-2Na a nearly linear range between 20 and 50 % r.h and two transitions could be identified. The transitions were also reflected in an increased gradient (Figure 7.4 C, lower graph). The second transition was accompanied by a change from 4 to 5 H_2O / Na^+.

On the adsorption branch of the water vapor sorption isotherm of Ilt-0.2Na a slightly increasing slope could be observed, too (Figure 7.4 D). The gradient changed significantly at 75 % r.h., which was also observed in the water vapor sorption isotherm in Figure 7.3 E., too.
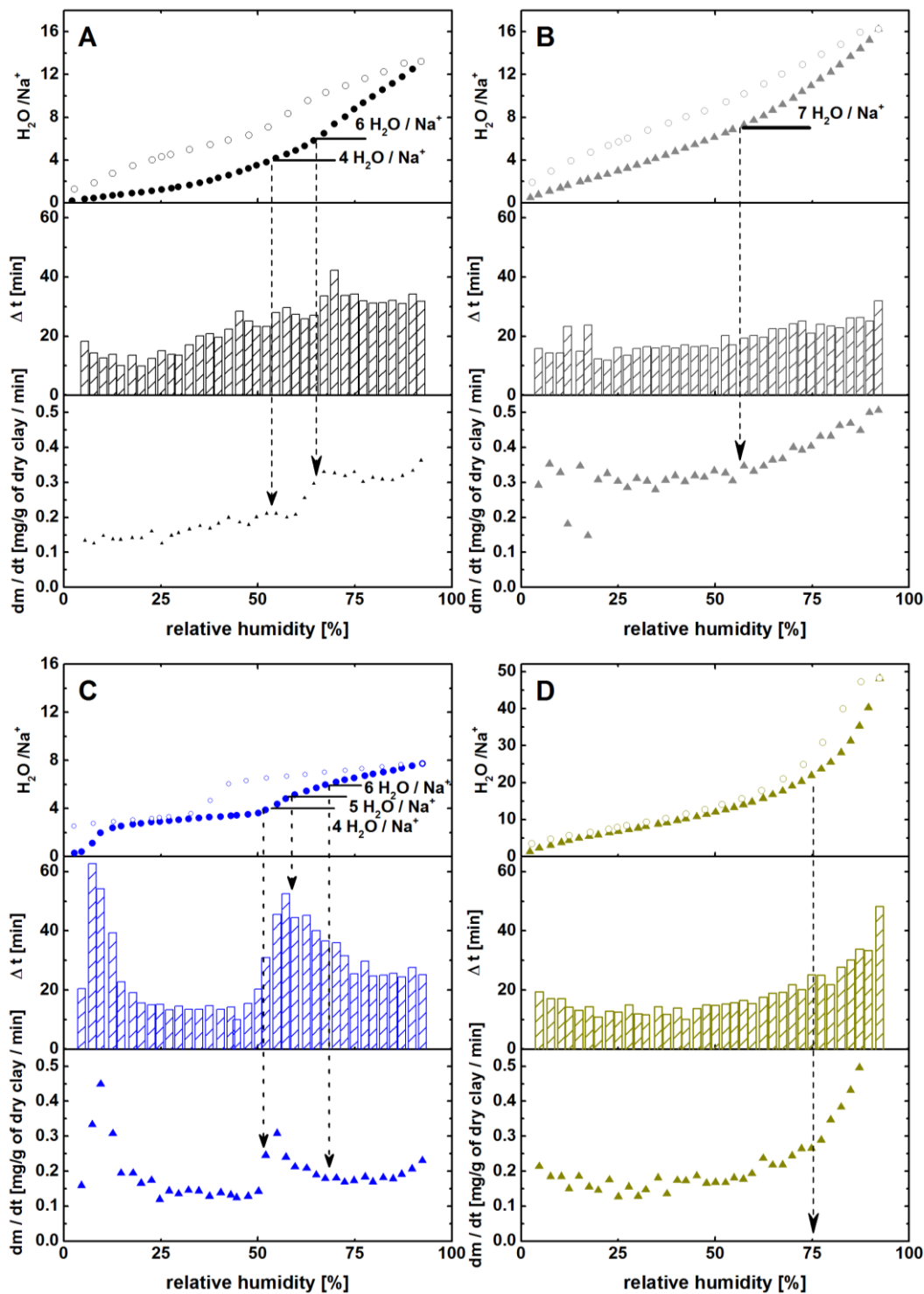
Figure 7.4 upper graph: Water vapor adsorption isotherm at 25 °C; middle: equilibration time; lower: adsorbed mass per time; all in function of the r.h. of (A) BV-M0.2Na, (B) BC-M0.2Na, (C) VT-2Na and (D) Ilt-0.2Na.

The selected natural smectites exhibit a heterogeneous layer charge distribution and, accordingly, different hydration states can coexist even under controlled conditions. Due to this coexistence, ranges in the ad- and desorption of water vapor with a slightly increasing slope were observed.

The high-charged VT-2Na exhibits a specific layer charge and, accordingly, hydration steps with a clear transition between 6 and 4 H_2O / Na^+ could be assigned. In addition, the first increased equilibration times with corresponding gradient at low r.h. showed the transition from 0W to 1W hydration state. The second significant change is reflected as a transition from 1W to 2W state accompanied by a change from 4 to 6 H_2O / Na^+. Hence, the intersection points of the calculated water contents are in accordance with the different hydration states of VT-2Na. These transitions could not clearly identified in the smectite isotherms. However, the results indicated that along these water vapor sorption isotherms from the montmorillonite and hectorite samples at least two hydration states (2W and 1W) with different hydration dynamics could be observed. On the desorption branches of the water vapor isotherms of BV-M0.2Na and SAz-M2Na, a noticeable change in the gradient was observed at 50 % r.h. indicating the transition from 2W to 1W state. For the higher charged SAz-M2Na, the transition from 1W to 2W state shifted to a lower water content of ≈ 3 H_2O / Na^+. On the desorption branch of all smectites and vermiculite isotherms, a marked change in the gradient was observed at < 10 % r.h., indicating the transition from 1W to 0W.

These findings indicated that the correlated water content depends on the properties of the 2:1 layer silicates. Whereas an a closed isotherm was observed at r.h. < 5 % of the low-charged smectites, higher charged SAz-2Na and VT-2Na still contain water after equilibration at 0.0 % r.h. indicating a stronger bound water at a higher layer charge. Despite Ilt-0.2Na, the particle size of the selected materials revealed that the extent of hysteresis also depends on the morphological character since a larger hysteresis was observed for the coarser BV-M0.2Na compared to the other smectite samples.

Isothermal long-time measurements

The STA results of the initial samples stored at 53% r.h. show full dehydration between 250 and 280 °C (Table 7.3). The lowest value obtained for Δm_{DHD} was calculated to 6.02 % for Ilt-0.2Na, whereas the highest was observed for SAz-2Na. The weight loss of the isothermal treatment showed that during 24 h at 35 °C (nominal) under N_2 purging none of the samples were completely dehydrated. Note the actually achieved temperature of the isothermal segment was 38 °C (± 1 °C). The residual moisture ranged between 5.9 % for BC-M0.2Na and 24.7 % for VT-2Na related to Δm_{DHD}. Based on the CEC_T of each sample the residual moisture ranged between in 0.3 and 0.5 H_2O / Na^+ for the dioctahedral smectites. For trioctahedral SHc-0.2Na the residual moisture was calculated to 0.7 H_2O / Na^+. Although Ilt-0.2Na is a non-swellable 2:1 layer silicate, the highest value for the residual moisture after isothermal treatment at 38 ± 1 °C was observed for this material. Based on the low CEC_T of 22 cmol(+)/kg the residual moisture was calculated to 1.8 H_2O / Na^+.
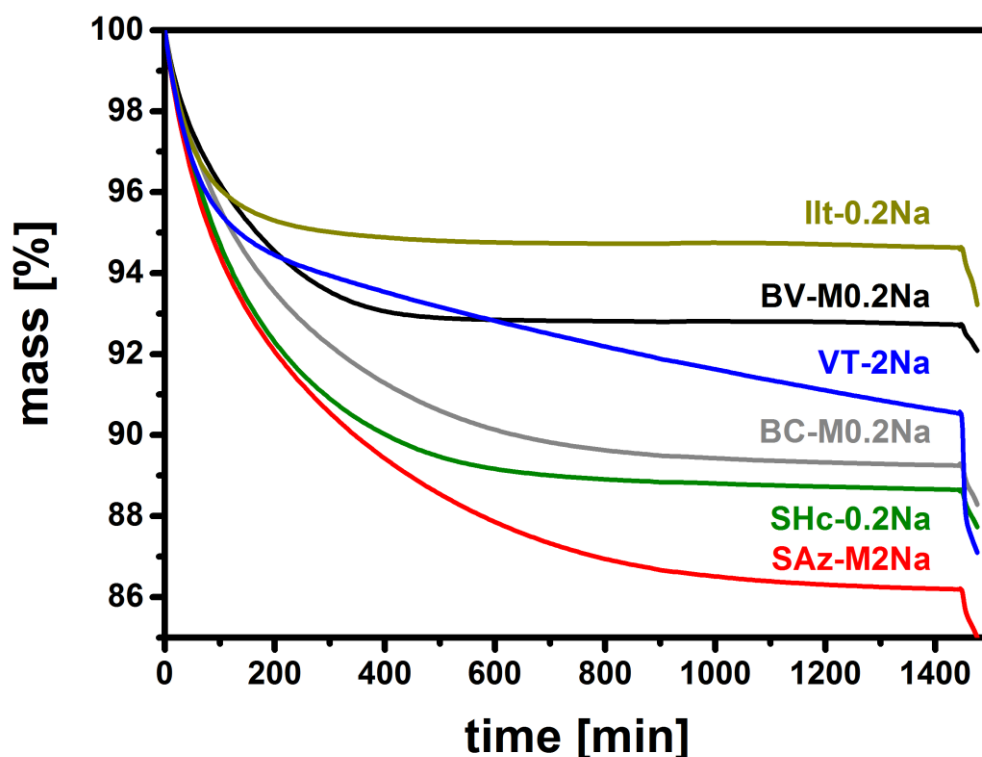
Figure 7.5 Results of longtime experiments showing TG curves of the isothermal (24 h at 38 ± 1 °C, N_2/N_2 50/20 mL/min) and dynamic segment (10 K/min, 40-400 °C) for the samples stored at 53 % r.h.

The isothermal treatment was followed by a dynamic segment (10 K/min) and an associated mass loss ranging between 0.37 and 3.02 % referred to the initial mass stored at 53 % r.h.. In sum, Δm_{24hN2} and $\Delta m_{24hN2+DHD}$ resulted in a nearly complete release of water (between 98.5 and 99.8 % percentage of total dehydration Δm_{DHD}). Additionally, a strong asymmetrical peak designated as $Peak_{H2O}$ with a maximum ranged between 156 and 170 °C was observed in all MS curves of evolved water upon heating to 400 °C (Figure 7.6). $T_{DHD,end}$ of the first run coincided with $T_{DHD,40-400}$ in the MS signal of evolved water of the followed dynamic segment (Figure 7.6).

Table 7.3 STA results of initial samples stored at 53 % r.h.(10 K/min) and results of isothermal treatment (24 h at 38 ± 1 °C).

	1	2	3	4	5	6	7	8	9
sample	$T_{DHD,end}$	Δm_{DHD}	W_{GT}	Δm_{DHD}	Δm_{24hN2}	Δ (2-4)	$\dfrac{\Delta m_{24hN2}}{\Delta m_{DHD}}$	residual moisture Δm_{DHD}	residual moisture
	[°C]	[%]	[%]	H_2O / Na^+	[%]	[%]	[%]	[% of Δm_{DHD}]	H_2O / Na^+
BV-M0.2Na	270	7.76	8.41	5.3	7.27	0.49	93.7	6.3	0.3
BC-M0.2Na	280	11.42	12.89	8.0	10.75	0.67	94.1	5.9	0.5
SAz-M2Na	280	14.89	17.50	7.5	13.81	1.07	92.7	7.3	0.5
SHc-0.2Na	270	12.14	13.82	10.1	11.35	0.79	93.5	6.5	0.7
VT-2Na	280	12.56	14.36	5.0	9.46	3.1	75.3	24.7	1.2
Ilt-0.2Na	250	6.02	6.41	16.2	5.37	0.65	89.2	10.8	1.8

Table 7.4 STA results of dynamic segment (10 K/min; 40-400 °C) for the samples stored at 53 % r.h..

sample	$T_{DHD,40-400}$	$\Delta m_{24hN2+DHD}$	$\Delta m_{24hN2} +$ $\Delta m_{24hN2+DHD}$	$\Delta m_{24hN2} +$ $\Delta m_{24hN2+DHD}$	$Peak_{H2O}$
	[°C]	[%]	[%]	[% of Δm_{DHD}]	[°C]
BV-M0.2Na	270	0.37	7.64	98.5	168
BC-M0.2Na	280	0.64	11.39	99.7	170
SAz-M2Na	280	0.85	14.66	98.5	156
SHc-0.2Na	270	0.62	11.97	98.6	164
VT-2Na	280	3.02	12.48	99.4	153
Ilt-0.2Na	250	0.64	6.01	99.8	169

The residual moisture content for all materials can be assigned to a tightly bound water with a resulting higher releasing temperature. The signals in the MS curves of evolved water clearly showed that this tightly bound water is still present after 24 h drying under N_2 purging. In addition, $T_{DHD,end}$ of the first run coincided with $T_{DHD,40-400}$ showing the reproducibility of determining the true water content with STA.

The MS signal of evolved water during the release of residual water has an asymmetrical form. This tailing signal correspond to the decomposition of organic matter displayed as an evolved CO_2 signal (Figure 7.7). The occurrences of a very low content of organic matter was confirmed by IR spectroscopy and specified as traces of glycerol, which were inherited from the dialysis tube during the preparation of the homoionic samples. Nevertheless, using N_2 as carrier and protective gas during TA, the signals are separated from each other, so that the $\Delta m_{24hN2+DHD}$ is not falsified by organic constituents. Since oxidation of organic constituents could be excluded by the measuring arrangement, the CO_2 signal may result from a pyrolytic reaction, which is also confirmed by the DSC signal (Figure 7.7).

As described in chapter 6, di- and trioctahedral smectites display structural heterogeneities and variation in size. In addition, the selected natural smectites exhibit a heterogeneous layer charge distribution and, accordingly, the results for theoretical models for dioctahedral smectites with only one layer charge (Emmerich et al., 2015) could not directly be transferred. Calculated models covering the full range on the solid solution series of montmorillonite and beidellite from 0.2 to 0.6 eq/f.u. with Na^+-saturated interlayers will enhance the understanding of heterogeneous swelling of smectites that always display a broad structural heterogeneity.

Although the water contents of the residual moisture were very low, a trend with increasing the layer charge can be observed for dioctahedral smectites. However, the residual moisture content of 0.7 H_2O / Na^+ observed for low-charged SHc-0.2Na was higher compared to the values for the other smectite samples. These findings indicated a more stable water binding due to a trioctahedral composition, which will thoroughly explain in chapter 9 using IR spectroscopy.

A tightly bound water was also observed for the Na^+-exchanged illite sample (Figure 7.6 E). The amount of the residual moisture was almost the same as in the smectites samples (Table 7.3) indicating that this residual H_2O has the same character as those of the smectites samples. Ilt-0.2Na is a non-swellable 2:1 layer silicate with a noticeable higher-edge site contribution compared to those of the smectites samples. As a result, water can either interact with its surfaces or may built a hydration shell with the cations at the edges. According to the results of STA, the exchangeable cations of Ilt-0.2Na hydrate in the same manner as in the smectites samples.
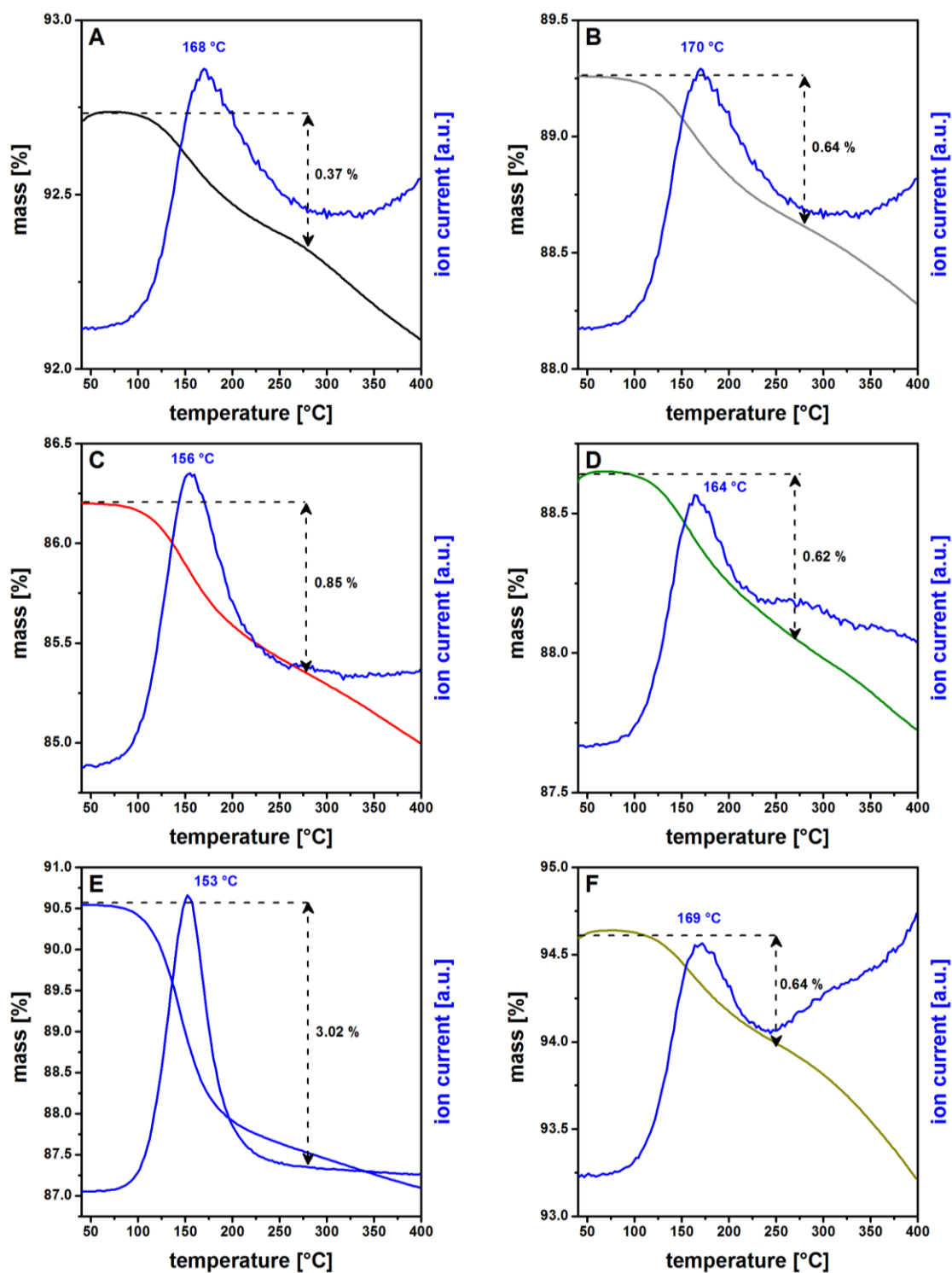
Figure 7.6 TG and MS curves of evolved water (m/e = 18, signal is displayed as blue curve) of the dynamic segment (10 K/min, 40-400 °C, N_2/N_2 50/20 mL/min) for (A) BV-M0.2Na, (B) BC-M0.2Na, (C) SAz-M2Na, (D) SHc-0.2Na, (E) VT-2Na and (F) Ilt-0.2Na.
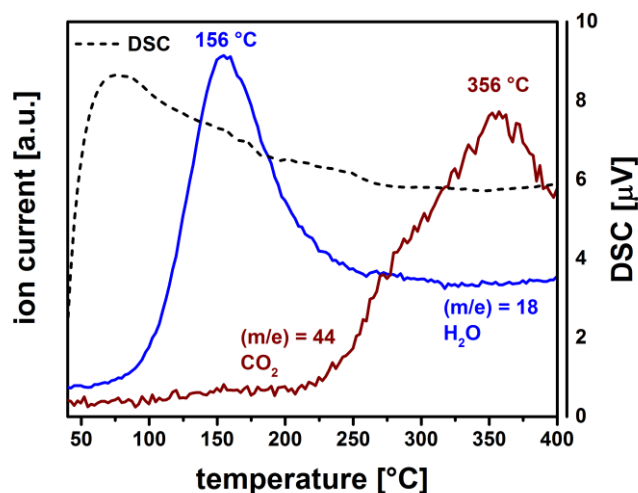
Figure 7.7 DSC and MS curves of evolved water (m/z = 18) and CO_2 (m/z = 44) during the release of tightly bound water of SAz-M2Na.

Stepwise release of adsorbed water by VT-2Na observed by STA

The water adsorption was studied by storing the samples at different r.h (between 11 and 93 % r.h.). An attempt was made to determine the ratio of a weakly bound water and water bound in the hydration shell of the interlayer cation by peak deconvolution from the MS curves of evolved water (m/e = 18) during STA. Unfortunately, this was not possible due to a strong asymmetrical character of the evolved water curves. Even for the vermiculite sample with two clearly separable peaks no reproducible results were obtained. However, the results of STA for BV-M0.2Na and VT-2Na showed that at least two kinds of water were released during dehydration. A tightly bound water and a less stable water with a corresponding lower releasing temperature (Figure 7.9).

A broad dehydration peak for BV-M0.2Na was observed over the whole r.h. range (Figure 7.9 A). Between 11 and 53 % r.h. the dehydration peak shifted from 112 to 135 °C. At 75 and 93 % r.h., a shoulder was observed at 121 and 131 °C (Figure 7.9 A). BV-M0.2Na was used as a representative dioctahedral smectite. The basal-spacing (d_{001}) values between 53 and 93 % r.h. for BV-M0.2Na are larger compared to those of VT-2Na. Together with a lower layer charge and CEC_T, a higher quantity of H_2O / Na^+ was observed at 75 and 93 % r.h. for BV-M0.2Na (Figure 7.8 A).

The corresponding MS curves of water (m/e = 18) showed two peaks at 112 and 152 °C for the VT-2Na stored at 53 % r.h. (Figure 7.9 B). The one with the lower releasing temperature shifted to 115 °C by increasing the r.h. to 93 % r.h., whereas the second remained constant at 156 °C. Since the dehydration peaks of BV-M0.2Na are strongly superimposed, only the example of VT-2Na is shown as the step-like release of adsorbed water during STA.
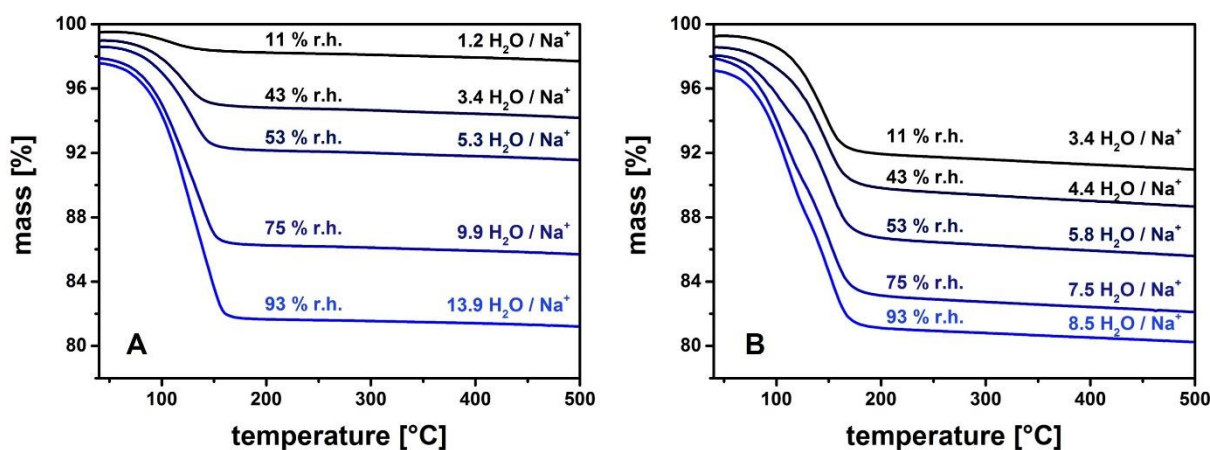
Figure 7.8 TG curves of (A) BV-M0.2Na and (B) VT-2Na stored at different humidities (11, 43, 53, 75 and 93 % r.h.), Δm_{DHD} measured with STA (10 K/min).
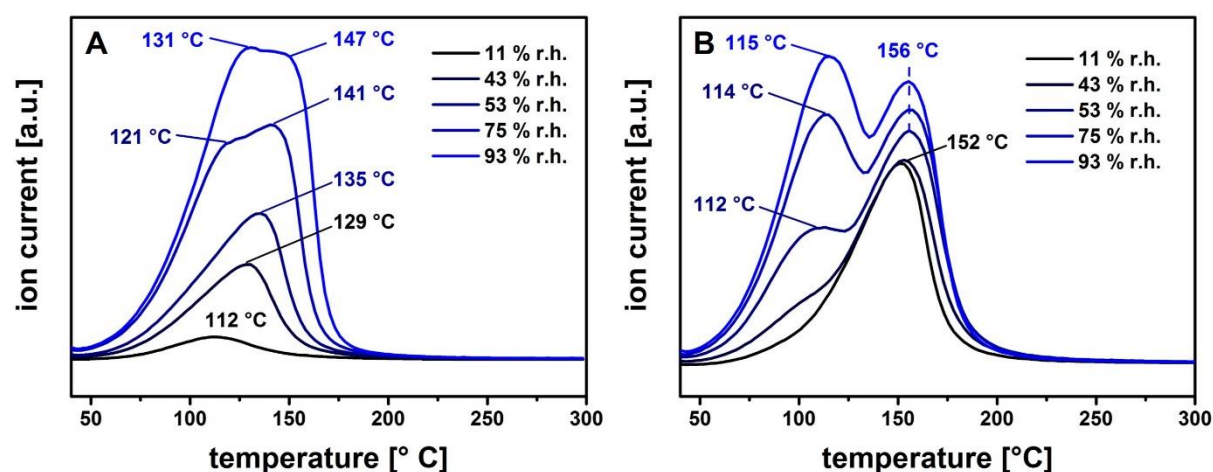
Figure 7.9 MS curves of evolved water (m/e = 18) during thermal treatment (10 K/min) for (A) BV-M0.2Na and (B) VT-2Na stored at different humidities (11, 43, 53, 75 and 93 % r.h.).

For VT-2Na stored at 11, 53 and 93 % r.h., Δm_{DHD} was calculated and plotted on the TG curve for the respective number of H_2O molecules per Na^+ (Figure 7.10). At 11 % r.h., the intersection point at 151 °C of a water content of 3 H_2O / Na^+ was observed at the peak maximum of the MS curve of water (m/e = 18). A shoulder at 100 °C was observed in the MS curve of water, too. For the sample stored at 53 % r.h., the intersection points of 4, 3 and 1 H_2O / Na^+ were found on the corresponding TG curve at 100, 127 and 162 °C. The total water content of 8.5 H_2O / Na^+ for the sample stored at 93 % r.h. was subdivided into 6, 4, 3 and 1 H_2O / Na^+ (Figure 7.10 C, upper graph). The intersection points of the water contents of 4 and 1 H_2O / Na^+ were found at 118 and 160 °C. On both MS curves of H_2O (53 and 93 % r.h.), the observed temperature for 3 H_2O / Na^+ was found between the two observed peaks (Figure 7.9 B and C, each lower graph). In addition, a correlation between the water content of 1 H_2O / Na^+ and the dehydration maximum observed at the higher temperature was found for VT-2Na.
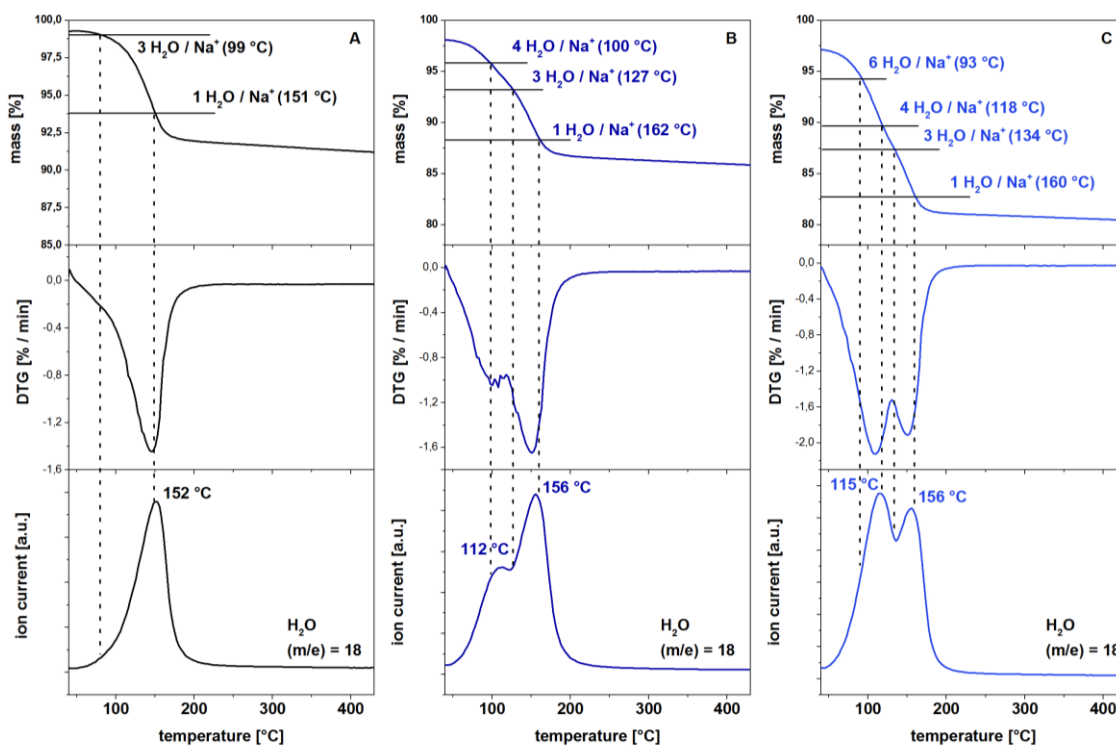
Figure 7.10 TG (top), DSC (middle) and MS curve of evolved water (m/z = 18) (bottom) during TA of VT-2Na stored at (A) 11 % r.h., (B) 53 % r.h and (C) 93 % r.h. (heating rate 10 K/min). Lines in TG curve indicate H_2O molecules per sodium cation.

7.5   Conclusions

The results obtained by water adsorption gave a general overview by mean of a qualitative and quantitative information of water sorption taken up by the 2:1 layer silicates. On XRD patterns for the samples stored at 53 % r.h. a 1W hydration state was observed for all smectite samples. The corresponding water contents ranged between 5.9 and 10 H_2O / Na^+ and implied that 1W state can even exist at water contents above 6 H_2O / Na^+. On the desorption branches of all swellable 2:1 layer silicates, clear changes between 6 and 4 H_2O / Na^+ in the gradient could be assigned. These transitions could not be clearly identified on the adsorption branches of the smectite isotherms. However, the results indicated that along these water vapor sorption isotherms from the montmorillonite and hectorite samples at least two hydration states (1W and 2W) with different hydration dynamics could be observed. Since the gravimetrical water vapor sorption isotherms are kinetically controlled, the equilibration times and their corresponding change in gradient enable a discrimination between different hydration states in 2:1 layer silicates. In the de- and adsorption of water vapor of smectite samples a slightly increasing slope were observed over the whole humidity range. This slight increase in the isotherm can be explained by a heterogeneous layer charge distribution, which enables the coexistence of different hydration states even under controlled conditions.

Isothermal long-time measurements under N_2 purging ($\approx$ 0 % r.h.) showed that for a complete dehydration of the selected 2:1 layer silicates a temperature above 40 °C is required. A tightly bound water after isothermal treatment was observed for all samples. For dioctahedral smectites a trend with increasing layer charge was observed. Increasing the layer charge resulted in a higher amount of residual moisture. For the low-charged SHc-0.2Na, the results implied that a trioctahedral structure leads to a more stable water binding, which was observed as a higher content of residual moisture. In addition, a tightly bound water was also observed for the Na^+-exchanged illite sample indicating that the exchangeable cations of Ilt-0.2Na hydrate in the same manner as in the smectites samples.

8 Unraveling the Coupled Processes of (De-) hydration and Structural Changes in Na⁺-saturated Montmorillonite

Most parts of this chapter is published under the same title 'Unraveling the Coupled Processes of (De-) hydration and Structural Changes in Na⁺-saturated Montmorillonite' (Florian Schnetzer, Peter Thissen, Nicolas Giraudo and Katja Emmerich) in The Journal of Physical Chemistry C 120(28) (2016) 15282-15287. DOI: 10.1021/acs.jpcc.6b04986. Data shown in supplementary information for the original publication are included in this chapter. *Changes were presented in italics.*

8.1 Abstract

The coupled processes of (de-)hydration and structural changes of a well characterized Na⁺-exchanged dioctahedral smectite with a low layer charge (0.26 mol(+)/formula unit) was studied by in situ transmission Fourier Transform Infrared Spectroscopy. Therefore, a sample preparation technique based on the Tethering by aggregation and growth method is extended to clay minerals to obtain a thin film of montmorillonite on a silicon wafer. After equilibration of the sample at 53 % relative humidity infrared measurements were done with a custom-made, heatable sample holder in an oxygen free atmosphere under N_2 purging which allowed subsequent FTIR measurements. Using a very thin film, deviation of the Si-O phonon modes could be simultaneously studied with the vibrational modes of water. The structural changes in the 2:1 layer of the montmorillonite during dehydration can be recognized from the shift of longitudinal optical Si-O phonon mode. The accompanied decrease and shift of the bending vibration of water δ(H-O-H) to lower wavenumbers is correlated to an increase of water-surface attraction. Finally, our experimental results were supported by ab initio thermodynamic simulations that revealed a decrease of the b_0 from 9.18 Å to 8.98 Å.

8.2 Introduction

Clays are commonly used as a barrier material due to their high swelling ability (Bergaya and Lagaly, 2013). In the past, most research focused on the increased basal spacings (d_{00l}) related to hydration (Cases et al., 1992; Ferrage et al., 2010a; 2011). However, few reported an additional change of the b-dimension.(Low et al., 1970) In this paper, a new model of the structural change along the a- and b-axis as a function of dehydration is developed. The long-term structural stability of clay minerals is an important factor for the usage of clay barriers,(Bourg and Tournassat, 2015) and thus, understanding the coupled processes of (de-)hydration mechanism and structural changes is a pre-requisite for control and monitor engineered clayey barriers.

One of the most important type of clays are bentonites. Bentonites mainly consist of low-charged swellable clay minerals called smectites. Within the smectite group montmorillonites are the most abundant minerals. Montmorillonites, the most heterogeneous phyllosilicates, are built of dioctahedral 2:1 layers (Wolters et al., 2009). Isomorphic substitutions mainly in the octahedral sheet (Al^{3+} substituted by Mg^{2+} and Fe^{3+}/Fe^{2+}) and ancillary in the tetrahedral sheet (Si^{4+} substituted by Al^{3+}) generate a negative layer charge and a huge structural variety. Exchangeable cations such as Na^+ in the interlayer compensate the charge to obtain electroneutrality.

The layer charge density and the hydration properties of the exchangeable cations control the swelling behavior of smectites (Bérend et al., 1995; Cases et al., 1992; 1997; Sato et al., 1992). At low moisture content, the crystalline swelling of smectites is a stepwise expansion of the layer-to-layer distance, leading to the well-known 1W, 2W and 3W hydration states with increasing basal spacings (d_{00l}) that can be observed by X-ray diffractometry (XRD) (Dazas et al., 2014; 2013; 2015; Ferrage et al., 2005b; 2007; Glaeser et al., 1967; Méring and Glaeser, 1954; Sato et al., 1992; 1996). Leonard and Weed (1967) and Low et al. (1970) first reported an additional increase of the b-dimension with increasing water content for vermiculite in 1W and 2W and for Na-saturated montmorillonite at water contents up to 2000% (Leonard and Weed, 1967; Low et al., 1970). The expansion of the b-dimensions of the unit cell was observed by XRD (Ravina and Low, 1972). They concluded that the increase in b-dimension is the result of strong interaction between montmorillonite and water, but no details about the coupled mechanism were provided. Later, Heller-Kallai and

Rozenson (1984) and Drits et al., 2005 did not observe the change in b-dimension for cis-vacant montmorillonite during dehydration while heating up to 400 °C. The aim of this study is to elucidate the structural changes in the 2:1 layers of Na^+-exchanged dioctahedral smectite during (de-) hydration by Fourier Transformation Infrared (FTIR) Spectroscopy supported by ab initio thermodynamic simulations.

In the past, many researchers investigated the (de)hydration of smectites by IR spectroscopy using self-supporting clay films (SSF) measured in transmission (Farmer and Russell, 1971; Sposito et al., 1983). The SSF only allow heating and infrared analysis up to 200 °C (Madejova, 2003). For investigations of powders, gels or aqueous suspension of clays and clay minerals reflectance spectroscopy such as the attenuated total reflectance (ATR) were used (Johnston and Premachandra, 2001; Kuligiewicz et al., 2015b; Yan et al., 1996). However, ATR techniques are subjected to the spectral limits of the ATR crystal as well as the ATR spectrum is distorted compared with a transmission spectrum, which has to be corrected (Griffiths, 1983; Griffiths and Pariente, 1988).To overcome these restrictions several immersion-based methods for preparation of surface attached films for IR spectroscopy exist (Ras et al., 2007b). Thereby the thin films of clay minerals are only weakly physisorbed on the surface of the carrier surface and can peel off during heating. Hanson et al. (2003) described an improved method to prepare strongly bonded monolayer films on the native oxide surface of Si (SiO_2/Si) (Hanson et al., 2003). The so-called T-BAG (Tethering by aggregation and growth) technique was initially developed for the deposition of self-assembled monolayers (SAMs) of phosphonic acids but can be adapted for deposition of thin films of clay mineral particles. Thereby, the vibrational modes of water together with the Si-O phonon modes can be studied.

The spectral region of the Si-O bonds is characterized by a broad absorption band at 1000-1250 cm^{-1}. Besides using curve-fitting methods it is hardly possible to distinguish between different Si-O stretching vibrations in the smectite layer. Four v(Si-O) vibration bands are discussed in dioctahedral smectites (Farmer and Russell, 1964). On the basis of early pleochroic studies of Farmer and Russel (1964) the v(Si-O) at 1086 cm^{-1} was assigned to a perpendicular, out-of-plane, v(Si-O) mode (Farmer and Russell, 1964). Johnston and Premachandra (2001) clearly resolved the position of the perpendicular Si-O at 1084 cm^{-1} for a Na^+ exchanged montmorillonite using polarized ATR-FTIR (Johnston and Premachandra, 2001). Yan et al. (1996, 1999) showed that

the O-H bending vibration of interlayer water and the Si-O stretching vibrations at 1046 and 1020 cm^{-1} of the tetrahedral layer are coupled as the layers come closer together. They interpreted that these Si-O stretching vibrations are somehow coupled to the vibrations of interfacial water molecules, but no details about the coupling mechanism were provided (Yan et al., 1996). Recent IR studies on the nature of the interfacial Si-O bonds showed that the detection of the longitudinal optical (LO) phonon mode of thin SiO$_2$ films makes it possible to characterize the newly formed Si-O bonds at the SAM/(SiO$_2$/Si) interface (Tian et al., 2010). Lange (1989) showed the experimental evidence that aside a longitudinal optical (LO) mode additional vibrations occur in thin amorphous SiO$_2$ films, including a transverse optical (TO) mode (Lange, 1989). Tian et al. (2010) revealed that the intensity of the transverse optical (TO) band are much weaker compared to the LO peak. They demonstrated the ability of the LO phonon mode to analyze the silanization kinetics of the SiO$_2$ surfaces and found a linear correlation between the LO mode and the SiO$_2$ thickness (Tian et al., 2010). These studies are based on the observations of Berreman (1963), who first reported the effect of the excitation of the LO mode by using oblique incidence with p-polarized light (Berreman, 1963).

The purpose of the present study is to investigate coupled process (de-)hydration and changes in the 2:1 layer of a Na$^+$-exchanged dioctahedral smectite using in situ IR transmission spectroscopy by adopting the T-BAG preparation. It is expected that deviation of the (Si-O)^{LO} phonon modes reflect the changing dimensions of the tetrahedral and octahedral sheet during dehydration. Since these experiments were carried out for well-defined particles with known orientation, state-of-the art calculations using density functional theory (DFT) could be employed to more precisely study this behavior. With the help of ab initio first-principles calculations, a new model of the structural change in all three dimensions of the structure during the release of interlayer water is developed. The wavenumber shift of δ(H-O-H) can now be correlated to an increase of water-surface attraction. Additionally, the increase of water-surface attractions is displayed in a coupled shift of the longitudinal optical Si-O phonon mode to lower wavenumber. As a result, the dimension of the 2:1 layer decreased along the a- and b-axis as a function of dehydration.

8.3   Material and Methods

BV-M0.2Na was selected for this study. XRD patterns of BV-M0.2Na were recorded as described in chapter 5.3.1. The structural formula was calculated according to chapter 5.3.6 and CEC_T was determined as described in chapter 5.3.3. Simultaneous Thermal Analysis (STA) and the water content after storing the sample at 53% relative humidity (r.h.) was determined as described in chapter 5.7.2.

The T-BAG sample preparation for spectroscopic investigation was described in 4.2.1. The determination of the film layer thickness on the wafer was done with an ESEM XL 30 FEG (Philips, Germany) at several cross-sections of an auxiliary sample. FTIR spectra were obtained as described in chapter 4.2.1. The first-principles calculations were done with the Vienna ab initio simulation program (VASP). This work was done by one of the co-authors (Peter Thissen) and will briefly described here. The total-energy and ground-state structure calculations in the present work were performed using density functional theory (DFT) as implemented in the Vienna ab initio simulation program (VASP) (Kresse and Furthmüller, 1996). The electron– ion interaction is treated within the projector-augmented wave (PAW) method (Kresse and Joubert, 1999). The valence electron wave functions are expanded into plane waves up to a kinetic energy cutoff of 360 eV. This energy cutoff was found to yield converged structural parameters for bulk montmorillonite. The Brillouin zone sampling was performed with a 1 x 1x 1 mesh of Monkhorst–Pack k-points, respectively (Monkhorst and Pack, 1976). The electron–electron exchange and correlation (XC) energy is approximated within the generalized-gradient approximation (GGA), using the XC potential developed by (Perdew et al., 1992). The PW91 functional was found to describe reliably the structure and energetics, especially of hydrogen bonded water molecules (Thierfelder et al., 2006; Thissen et al., 2009; 2012). The optimization of the atomic coordinates and unit cell size / shape for the bulk materials was performed via a conjugate gradients technique which utilizes the total energy and the Hellmann Feynman forces on the atoms and stresses on the unit cell. The Na-exchanged montmorillonite is modeled employing three-dimensional periodic boundary conditions (PBC) (de Leeuw and Purton, 2001).The stoichiometric description of this model is given by $[Na_1(Si_{16})(Al_7Mg_1)O_{40}(OH)_8]$ (Emmerich et al., 2015). We validate our model choice by the calculation of the surface charge density. Consequently, our model system has a surface charge density of 0.172 C / m^2.

8.4 Results and Discussion

Material characterization, water content & hydration state

BV-M0.2Na is characterized in chapter 6.1.1. The STA results of the initial sample stored at 53% r.h. shows a full dehydration at 280 °C associated with a mass loss of 7.23% (Figure 8.1). Including the mass loss during the isothermal heating Δm_{DHD} was calculated to 7.83% and w_{gt} was calculated to 8.50 %. Based on the CEC of 89 cmol(+)/kg the water content resulted in 5.3 H2O molecules per Na$^+$ cation. Continuous heating reduced the number of H_2O molecules per Na$^+$ (see Figure 8.1 and 8.2).
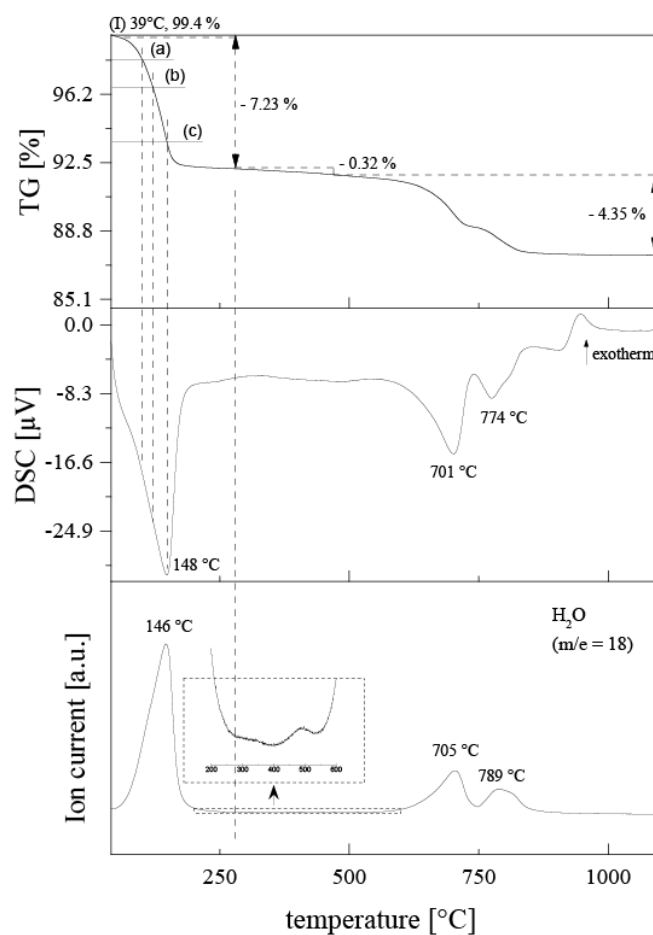
Figure 8.1 STA curves with TG (top) DSC (middle), and MS curve of evolved H_2O (m/z=18) (bottom) for BV-M0.2Na stored at 53% r.h.; Lines in TG curve indicate H_2O molecules per sodium cation (a) 4 H_2O / Na$^+$, (b) 3 H_2O / Na$^+$ and (c) 1 H_2O / Na$^+$.

Determination of layer thickness

The thickness of BV-M0.2Na on an oxidized silicon wafer was determined to a mean value of 185 ± 20 nm from several cross-section captions done by ESEM (Figure 8.2).
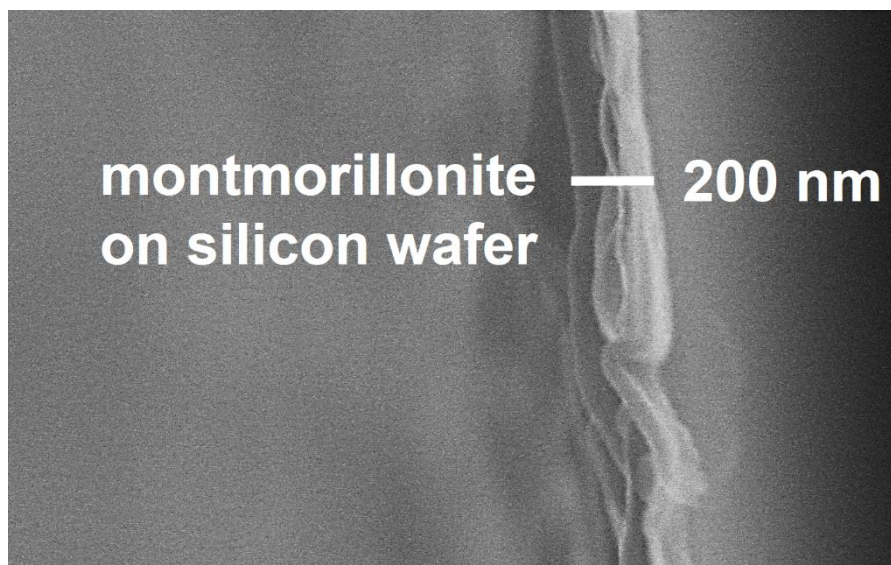
Figure 8.2 Environmental scanning electron microscopy image of a silicon wafer coated with an about 200 nm montmorillonite.

FTIR transmission spectroscopy

The measured water content of 8.50 % with STA can be correlated to the FTIR spectrum of the hydrated sample at 25 °C (Figure 8.3), integrating the area below the region between 3705 cm^{-1} and 3000 cm^{-1}. Accordingly, the water content of the montmorillonite was calculated from each spectrum in dependence of heating temperature (Figure 8.4 and 8.5).
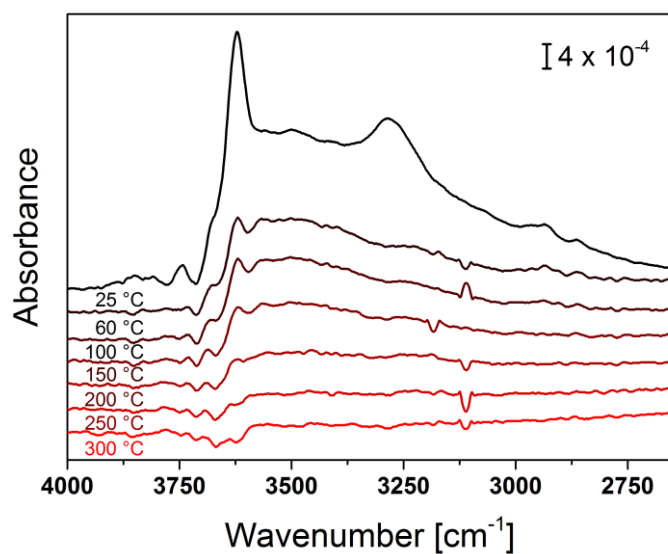
Figure 8.3: Infrared spectra of a silicon wafer coated with a thin layer of montmorillonite as a function of temperature (from 25 °C to 300 °C); all spectra are referenced to the dry sample.
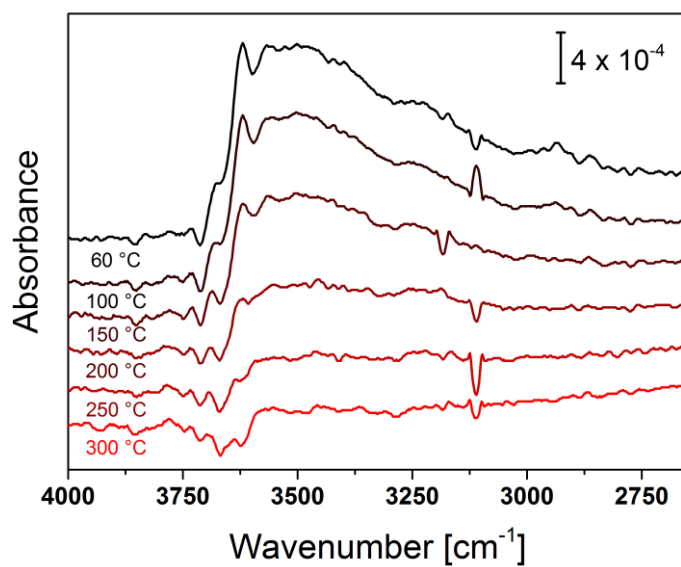
Figure 8.4: Infrared spectra of a silicon wafer coated with a thin layer of montmorillonite as a function of temperature (from 60 °C to 300 °C); all spectra are referenced to the dry sample.
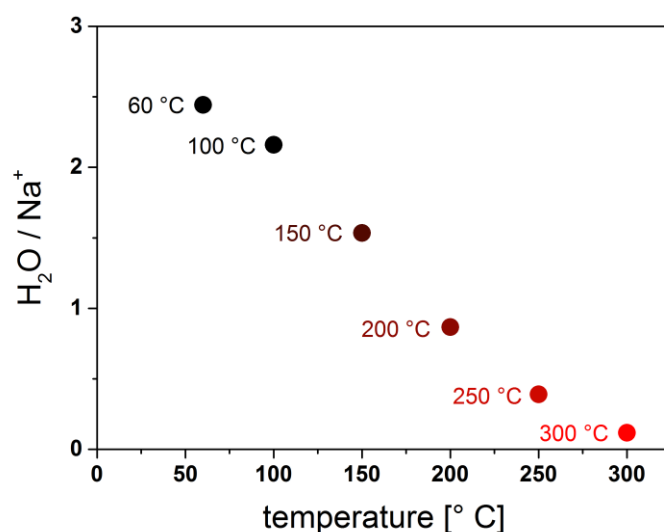
Figure 8.5: Interlayer water content as a function of temperature

At 60 °C, a sharp band at 3620 cm^{-1} and a broad band between 3600 cm^{-1} and 3300 cm^{-1} occur (Figure 8.4, top line). Both correspond to O-H stretching vibrations. At 100 °C and 150 °C, the intensity of the sharp and the broad band decreased, which is related to the decrease in water content (Figure 8.5). After heating at 200 °C and 250 °C, the sharp O-H stretching vibration at 3620 cm^{-1} is hardly visible. At 300 °C, a shift from 3620 cm^{-1} to 3600 cm^{-1} was observed.
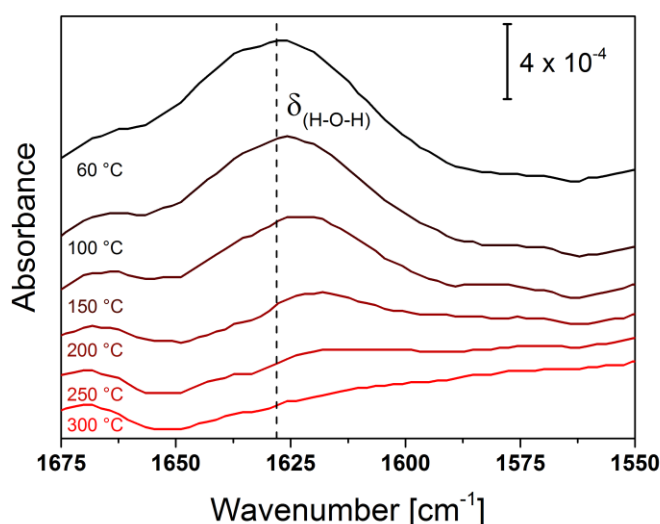
Figure 8.6: Infrared spectra of a silicon wafer coated with a thin layer (about 200 nm) of montmorillonite as a function of temperature (from 60 °C to 300 °C); all spectra are referenced to the dry sample.

The correlated decrease and shifting of the bending vibration of water δ(H-O-H) was observed (Figure 8.6). At 60 °C, δ(H-O-H) appeared at 1628 cm^{-1} (Figure 8.7) and shifted to 1619 cm^{-1} at heating up to 200 °C. Thereafter it remained at a constant wavenumber at 1619 cm^{-1} (Figure 8.7).
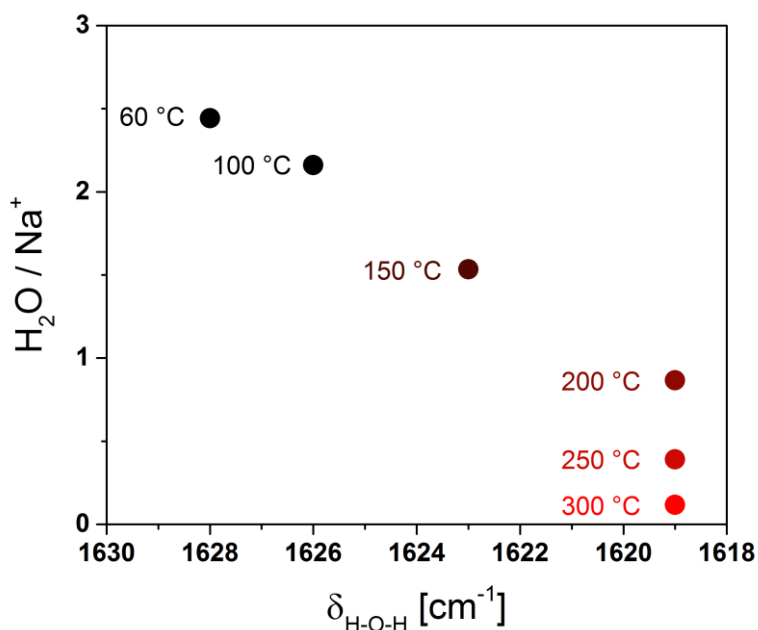
Figure 8.7: Evolution of δ(H-O-H) as a function of temperature.

During dehydration by heating up to 300 °C coupled changes in Si-O stretching vibration (Figure 8.8) and a shift of the (Si-O)^{LO} phonon mode (Figure 8.9) were observed, too. The (Si-O)^{LO} shifted from 1097 cm^{-1} to lower wavenumbers, which clearly revealed that the (Si-O)^{LO} is directly coupled with the release of interlayer water.
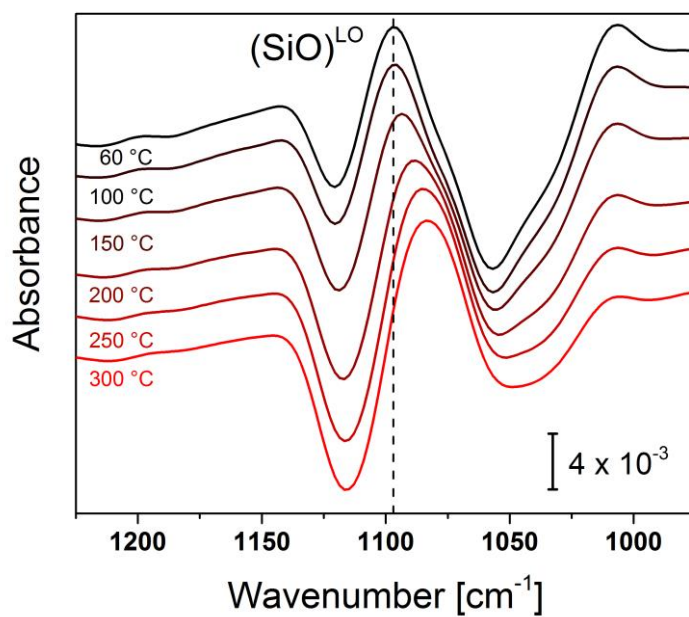
Figure 8.8: Infrared spectra of a silicon wafer coated with an about 200 nm montmorillonite as a function of temperature (from 60 °C to 300 °C); all spectra are referenced to the dry sample.
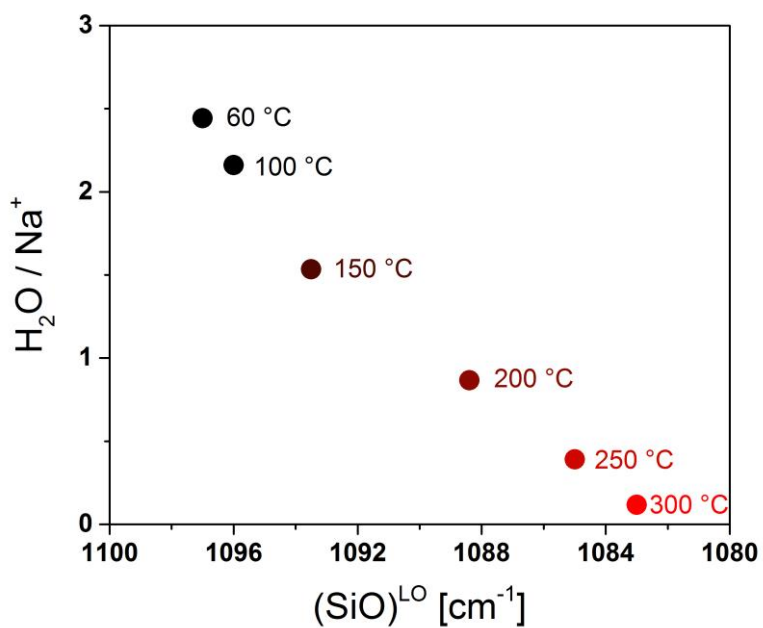
Figure 8.9: Evolution of (Si-O)^{LO} as a function of temperature.
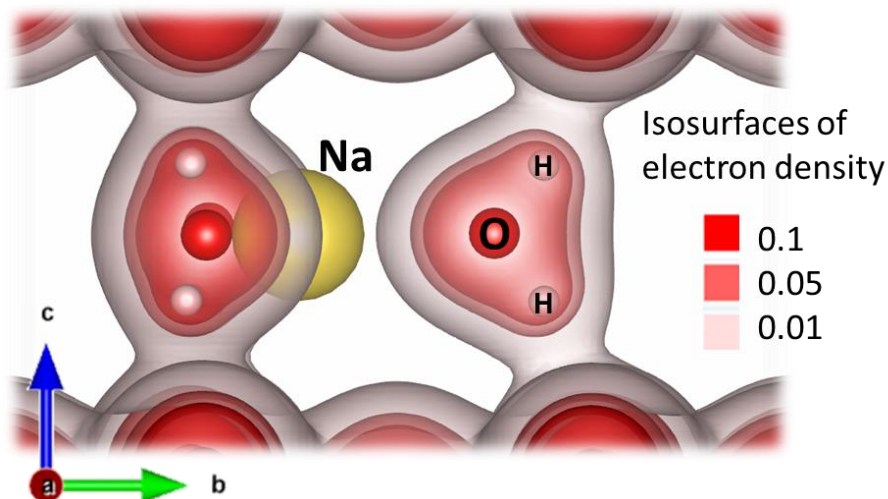
Figure 8.10: Side view on energetically favorable [Na$_1$(Si$_{16}$)(Al$_8$Mg$_2$)O$_{40}$(OH)$_8$] x 3 H$_2$O interface combined with isosurfaces of electron density.

After heating at 60 °C the interlayer Na$^+$ of the montmorillonite BV-M0.2Na was surrounded by 3 water molecules in the 1W hydration state (Figure 8.10). The lattice constants a_0 and b_0 of the dioctahedral smectite for this hydration state were determined to be 5.30 Å and 9.18 Å. The thermodynamic ground state was constructed by solving the Birch–Murnaghan equation of state. The hydration shell of 3 H$_2$O around each Na$^+$ coincides with the surface/water interaction via hydrogen bonds and no water-water interactions exist (Emmerich et al., 2015). Emmerich et al. (2015) showed for a low charged Na$^+$-montmorillonite that the water-surface attraction increases as the amount of water molecules in the interlayer decreases. At lower water contents (< 3 H$_2$O / Na$^+$) no more water-water attraction exist. The wavenumber shift of δ(H-O-H) is correlated to an increase of water-surface attraction, which means that the water molecules are highly polarized in the mono-hydrated state (1W layer) and have a lower O-H bending mode (1628 cm^{-1}) compare to liquid water (1643 cm^{-1}). Furthermore, these conditions lead to strong interactions from interfacial water and the tetrahedral layer, which can be observed as a shift of the (Si-O)^{LO} to lower wavenumbers (Figures 8.8 and 8.9).

In order to gain deeper understanding of the coupled processes of dehydration and Si-O phonon mode evolution we calculated further models with different water content. A more detailed analysis of the corresponding unit cells reveals, however, that the lateral dimension of the 2:1 layers decrease as the water content decreases along the a- and b-axis (the lattice constants a_0 and b_0, for 0 H$_2$O/Na$^+$, were find to be 5.18 Å and 8.98

Å). This is in agreement with our experimental findings from FTIR and previous XRD investigations, where the main focus lies in the evolution of the (060) reflection (Low et al., 1970; Ravina and Low, 1972).

As the findings of the previous FTIR analysis have shown, that the release of interlayer water in BVM0.2-Na affected both: the vibrational modes of water and the longitudinal optical Si-O phonon mode. The changes in the tetrahedral sheet during dehydration can be recognized from the peak (Si-O)^{LO}, which is an order of magnitude higher compare to the vibrational modes of water. The shifting behavior describe the changing lateral dimensions of the 2:1 layer during dehydration. As the water content decreases corresponding layer volume decreases along the a- and b-axis.

8.5 Conclusions

Investigations of the coupled processes of dehydration and Si-O phonon mode evolution have been done by FTIR allowing consideration of all structural changes of the montmorillonite layers during dehydration. With the help of ab initio first-principles calculations, a new model of the structural change in all three dimensions of the tetrahedral and octahedral layer during the release of interlayer water was developed. The observed shift of δ(H-O-H) and (Si-O)^{LO} to lower wavenumbers can now be correlated to an increase of water-surface attraction, which means that the water molecules are highly polarized in the mono-hydrated state (1W layer) and have a lower O-H bending mode (1628 cm^{-1}) compare to liquid water (1643 cm^{-1}). The increase of surface-water attractions with increasing temperature is displayed in a coupled shift of the longitudinal optical Si-O phonon mode to lower wavenumber. As a result, the lateral dimension of the 2:1 layer decrease as the water content decreases, resulting in a volume decrease along the a- and b-axis.

9 Hydration hysteresis of swelling 2:1 layer silicates

Most parts of this chapter is submitted under the title 'Toward a comprehensive understanding of hydration hysteresis of swelling of 2:1 layer silicates' (F. Schnetzer, C. T. Johnston, G. S. Premachandra, R. Schuhmann, P. Thissen, K. Emmerich) to the Journal ACS Earth and Space Chemistry on 21 February 2017.

9.1 Abstract

Several 2:1 layer silicates comprising di- and trioctahedral smectites of different layer charge between 0.2 to 0.4 per formula unit and a trioctahedral vermiculite were studied by an *in-situ* method that allowed FTIR spectra and water vapor sorption isotherms to be obtained simultaneously. Particle size and shape of the selected materials were determined using X-ray diffraction (XRD) and gas adsorption analysis, which provided which gave a detailed picture of the particle size with resulting edge site proportion. The aim of this study was to elucidate the hysteresis mechanism in 2:1 layer silicates during desorption and adsorption of water vapor. Domains in the de- and adsorption of water vapor of the smectite samples with a slightly increasing slope were explained by a heterogeneous layer charge distribution, which enables the coexistence of different hydration states even under controlled conditions. Whereas hysteresis was observed over the entire isothermal range of the smectites, the isotherm of the vermiculite sample only showed hysteresis in the transition from mono- to bi-hydrated state. It was also showed that hysteresis is a function of the layer charge distribution, the achieved water content and the particle size with resulting edge site contribution. Increasing the edge site proportions resulted in an increased hysteresis. The findings from the experimental FTIR/gravimetric analysis showed that the transition from 2W to 1W and backwards is visible using IR spectroscopy. The shifting of δ(H-O-H) was influenced by the layer charge, charge distribution, octahedral substitutions and the layer dimension. Finally, the experimental results were supported by *ab initio* thermodynamic simulations that revealed the different shifting behavior of δ(H-O-H) related to the differences in surface charge density and octahedral compositions.

9.2 Introduction

Smectites and vermiculites are planar hydrous 2:1 layer silicates. They are among the most dominant minerals in many soils and clay deposits. These types of clay minerals impart unique properties due to their intrinsic shrink-swell characteristics (Anderson et al., 2010; Bittelli et al., 2012; Boutareaud et al., 2008; Bradbury et al., 2015; Han et al., 2014; Iwata et al., 1995). At low moisture content, crystalline swelling of 2:1 layer silicates proceeds in a stepwise expansion of the layer-to-layer distance (Beyer and Graf von Reichenbach, 2002; Dazas et al., 2015; Ferrage, 2016; Ferrage et al., 2010a; 2011; Glaeser et al., 1967; Méring and Glaeser, 1954; Sato et al., 1992; 1996). The swelling shows hysteresis and desorption and adsorption of water proceed differently (Bérend et al., 1995; Cases et al., 1992; 1997; Fu et al., 1990; Johnston et al., 1992; Sposito and Prost, 1982; Tambach et al., 2004a). In this chapter, the hysteresis in clay swelling was studied as a function of relative humidity (r.h.) using powder X-Ray diffraction (XRD), gas adsorption analysis and infrared (IR) spectroscopy and related these experimental results to the intrinsic properties (e.g. layer charge, charge location, octahedral composition and particle size) of dioctahedral and trioctahedral 2:1 layer silicates being studied. Beside their widespread importance in soils, clay minerals are also used in many different applications, such as construction materials or barrier materials in waste repositories (Harvey and Lagaly, 2013). For these applications, it is important to control and monitor their swelling behavior and, hence, understanding the molecular mechanism of hysteresis in clay swelling is a pre-requisite.

Vermiculites are swellable 2:1 layer silicates which have a higher net negative layer charge between 0.6 and 0.9 per formula unit (Besson et al., 1974; de la Calle and Suquet, 1988). In addition to higher layer charge, the particles size of vermiculites is greater than that of smectites. Vermiculites are commonly coarse with a particle size > 20 µm and, consequently, vermiculite particles are often large enough for detailed structural studies (Ferrage et al., 2015). Smectites can have a di- or trioctahedral character of the octahedral sheet. The montmorillonite–beidellite series are the most common dioctahedral smectites with a general structural formula of $M^{n+}_{x+y/n}$ $(Si_{4-x}Al_x)$ $(Al,Fe^{3+}_{2-y}\ Mg,Fe^{2+}_y)\ O_{10}(OH)_2$ (Emmerich, 2013; Wolters et al., 2009). Hectorite is a trioctahedral smectite and has an ideal structural formula of $M^{n+}_{z/n}$ (Si_4) $(Mg_{3-z}\ Li^+_z)$ $O_{10}(OH)_2$. Here, x + y and z, respectively, represents the permanent layer charge resulting from substitutions within the tetrahedral and octahedral sheet ranging from

0.2 to 0.6 mol(+) per formula unit (f.u.). M^{n+} represents the charge-compensating counterions in the interlayer of smectites, which is naturally Na^+, K^+, Ca^{2+} or Mg^{2+}. In addition to the permanent layer charge, a variable charge is lying at the edge of the layers associated with amphoteric sites such as Si-OH and Al-OH (Sposito, 1984). These pH dependent edge sites play a significantly role of the stability of aqueous clay suspensions (Tombácz and Szekeres, 2004). Based on the theoretical studies on edge site properties of White and Zelazny (1988), Tournassat et al. (2003) correlated edge site properties with the chemical character of few Na-saturated dioctahedral smectites (Tournassat et al., 2003; White and Zelazny, 1988). Delavernhe et al. (2015) used that approach and showed in a comprehensive characterization that edge site properties also differ within four representative dioctahedral smectites (Delavernhe et al., 2015). The reason for this was primarily the layer dimension, which determines edge site properties. With regards to the swelling hysteresis of 2:1 layer silicates the edge site reactivity has so far received little attention.

The crystalline swelling of 2:1 layer silicates is commonly described by XRD, where the main focus lies in the evolution of the basal-spacing (d_{001}) value under variable r.h. (Dazas et al., 2014; Ferrage et al., 2010a; 2011). The reversible swelling mechanism is induced by hydration of the exchangeable and charge-compensating counterions in the interlayer of swellable 2:1 layer silicates leading to discrete water layers which increase in number from one to three (Emmerich et al., 2015). These discrete hydration states are known as mono-hydrated (1W, layer thickness ≈ 11.6-12.9 Å), bi-hydrated (2W, layer thickness ≈ 14.9-15.7 Å) and tri-hydrated (3W, layer thickness ≈ 18-19 Å) (Dazas et al., 2014; Ferrage et al., 2005a). The latter is being less common. Many studies have recognized that these hydration states usually coexist in smectites, even under controlled conditions (Ferrage et al.,; 2005a; 2005b; 2010a). Using XRD, such a coexistence is shown by the irrationally of the 00l reflections as well as by peak profile asymmetry at the transition between two hydration states (Ferrage et al., 2005b; 2010a; Sato et al., 1992). To quantify the amount of different layer types with different hydration states as a function of r.h., XRD profile modelling procedures were developed and extensively described in (Ferrage, 2016). The effect of layer charge on the interlayer water arrangement in natural dioctahedral smectites (Ferrage et al., 2007) and in synthetic tetrahedral charged trioctahedral smectites (saponites) (Dazas et al., 2010a; 2015) has been studied using XRD profile modelling. From the relative proportions of hydration states upon dehydration, they demonstrated the influence of

layer charge on smectite hydration. They showed that smectite layer-to-layer distance decrease with increasing layer charge because of the enhanced cation-layer electrostatic attraction and the transition from 2W to 1W state shifts to lower water contents. XRD studies of homoionic smectites also showed that the basal spacings are larger when the layer charge is located in the octahedral sheet than when it is in the tetrahedral sheet (Sato et al., 1992) However, questions regarding the orientation of interlayer water molecules cannot be answered by such structural studies (Ferrage et al., 2011). A second swelling regime can be identified. Beyond d_{001} –spacings of 22 Å osmotic swelling occurs, in which a competition of repulsive electrostatic forces and long-range attractive von der Waals (vdW) forces govern the interactions between adjacent layers (Gilbert et al., 2015; Laird, 2006). Recent cryogenic transmission electron microscopy (cryo-TEM) and small-angle X-ray scattering (SAXS) studies on Na^+-saturated montmorillonites showed the importance of long-range vdW forces to the structure of osmotic hydrates (Tester et al., 2016). Although osmotic swelling is beyond the scope of this paper, we will investigate the influence of particle size and layer charge and how vdW forces contribute to the crystalline swelling process.

IR spectroscopy allows to probe the clay-water interface on the molecular scale. The major vibrational bands of H_2O occur in two regions of the mid-infrared (MIR) corresponding to the O-H stretching ν(O-H) and H-O-H bending δ(H-O-H) region (Johnston et al., 1992). Analysis of the ν(O-H) is commonly impeded due an overlap of bands produced by the structural O-H groups and absorbed water (Kuligiewicz et al., 2015a; 2015b). The δ(H-O-H) region, however, is comparatively free from spectral interference. The δ(H-O-H) band is sensitive to the extent of hydrogen bonding between H_2O molecules and, hence, it can be used as a molecular probe for water-clay interactions. In order to relate the vibrational properties of clay-water interactions to water uptake, prior studies have coupled spectroscopic methods with quartz crystal- or gravimetric microbalance measurements (Johnston et al., 1992; Schuttlefield et al., 2007; Tipton et al., 1993; Xu et al., 2000). All these IR studies showed that the vibrational bands of water change as a function of water content and that at water contents lower than 6 H_2O per interlayer cation the H_2O molecules are highly polarized by their proximity to the exchangeable cation. Neutron scattering data (Ferrage et al., 2010a; 2011; Sposito and Prost, 1982) have also shown that the water molecules coordinated to the interlayer cation are in a constrained environment relative to those in bulk water (Johnston et al., 1992). It was also confirmed that the structural O-H

groups of trioctahedral smectites are vibrating almost perpendicular to the basal surface and those of dioctahedral smectites almost horizontally to the basal surface in hydrated state (Ras et al., 2007a; 2007b; Schoonheydt and Johnston, 2013). However, only little is known about the dependence of the interlayer water and its relation to the clay structural intrinsic properties (e.g. layer charge and octahedral composition) of di- and trioctahedral 2:1 layer silicates.

Up to now, the occurrence of hysteresis is commonly associated with capillary condensation, depending on the pore structure and adsorption mechanism (Thommes et al., 2015). For swellable 2:1 layer silicates, the literature suggests different explanations for the origin of the hysteresis (e.g. structural rearrangements (Boek et al., 1995a; Fu et al., 1990; van Olphen, 1965) or phase transitions (Laird and Shang, 1997; Tamura et al., 2000)). Recent studies showed on a molecular scale that the swelling hysteresis has a kinetic origin in terms of a free-energy barrier that separates the layered hydrates (Tambach et al., 2004a; 2004b; 2006). This free-energy barrier is dominated by breaking and formation of hydrogen bonds within water layers (Tambach et al., 2006) However, no study has described the hysteresis in clay swelling as a function of the chemical and morphological parameters of di- and trioctahedral 2:1 layer silicates.

Here, first the particle size of the selected materials will compared using the approach described by Delavernhe et al. (2015). Additionally, the shape of the micrometer-sized particles will be determined by ESEM and XRD. Subsequently, the influence of the intrinsic structural heterogeneity of the 2:1 layers on hydration properties using FTIR with emphasis on the sorbed water band will be investigated. Here, the focus is on the transition from the 2W to 1W and the influence of layer charge and octahedral composition. The deformation mode of water δ(H-O-H) reflects the change from bi- to mono-hydrated state and can, therefore, be used as molecular probe for water-smectite and -vermiculite interactions. Since these experiments allow to collect IR spectra and water vapor sorption isotherms simultaneously, a relationship between gravimetrical sorption and IR data can be made. Additionally, state-of-the-art calculations using density functional theory (DFT) we be nvestigated to support our experimental findings from FTIR. With the help of first-principles calculations, the different shifting behavior of δ(H-O-H) related to the differences in surface charge density and octahedral compositions will be explained.

9.3 Material and methods

The 2:1 layer silicates BV-M0.2Na, SAz-M0.2Na, SHc-0.2Na and VT-2Na were selected for this investigations. XRD patterns of these materials were recorded as described in chapter 5.3.1. Additionally, the CSD of each material was calculated. Particle size characterization was done as described in chapter 5.5.

A fourier transform infrared spectroscopy (FTIR)/gravimetric cell was used and described in chapter 4.2.2.

As well as in chapter 8, the first-principles calculations were done with the Vienna ab initio simulation program (VASP). This work was done by one of the co-authors (Peter Thissen) and will briefly described here. The total-energy and ground-state structure calculations in the present work were performed using DFT as implemented in the Vienna ab initio simulation program (VASP) (Kresse and Furthmüller, 1996). The electron-ion interaction was treated within the projector-augmented wave (PAW) method (Kresse and Joubert, 1999). The valence electron wave functions were expanded into plane waves up to a kinetic energy cutoff of 360 eV. This energy cutoff was found to yield converged structural parameters for bulk calculations. The Brillouin zone sampling was performed with a 1 x 1 x 1 mesh of Monkhorst–Pack k-points, respectively (Monkhorst and Pack, 1976). The electron-electron exchange and correlation (XC) energy was approximated within the generalized-gradient approximation (GGA), using the XC potential developed by Perdew et al (Perdew et al., 1992). The PW91 functional was found to describe reliably the structure and energetics, especially of hydrogen bonded water molecules (Thierfelder et al., 2006; Thissen et al., 2009; 2012). The optimization of the atomic coordinates and unit cell size / shape for the bulk materials was performed via a conjugate gradients technique which utilizes the total energy and the Hellmann Feynman forces on the atoms and stresses on the unit cell. In addition to the k-point density, the convergence in calculations of clay minerals was also dependent on the thickness of the mineral layer. For every atomic configuration we checked convergence by running a series of calculations with different layer thicknesses. The thermodynamic minimum was then constructed by solving the Birch-Murnaghan equation of state.

Table 9.1 Stoichiometric description of the modeled supercells with solely octahedral charges

stoichiometric description	layer charge per formula unit (f.u.)	abbreviation
$[Na_1(Si_{16})(Al_7Mg_1)O_{40}(OH)_8]$	0.25	MMT0.25
$[Na_2(Si_{16})(Al_6Mg_2)O_{40}(OH)_8]$	0.5	MMT0.5
$[Na_1(Si_{16})(Mg_{11}Li_1)O_{40}(OH)_8]$	0.25	HCT0.25

The stoichiometric description of the supercells is given in Table 9.1. MMT0.25 and MMT0.5 is described in (Emmerich et al., 2015). The choice of the two dioctahedral models are validated by the calculation of the surface charge density (0.172 and 0.344 C / m², respectively). The model system for HCT0.25 has a trioctahedral structure and a surface charge density of 0.172 C / m².

9.4   Results and discussion

Mineralogical and chemical characterization

The materials were characterized in chapter 6.1.1. The particle size characterization can be found in chapter 6.2.

Initial hydration state and dry mass

On XRD pattern of BV-M0.2Na and SAz-M2Na stored at ≈ 86 % r.h. d_{001} was observed between 15.3 and 15.5 Å characteristic for a 2W hydration state (Ferrage et al., 2010a; 2011). The d_{001} of SHc-0.2Na was observed at 15.8 Å (Figure 9.1). The 2W state (d_{001} = 14.85 Å) could be observed for VT-2Na, too (Figure 9.2) (Beyer and Graf von Reichenbach, 2002).
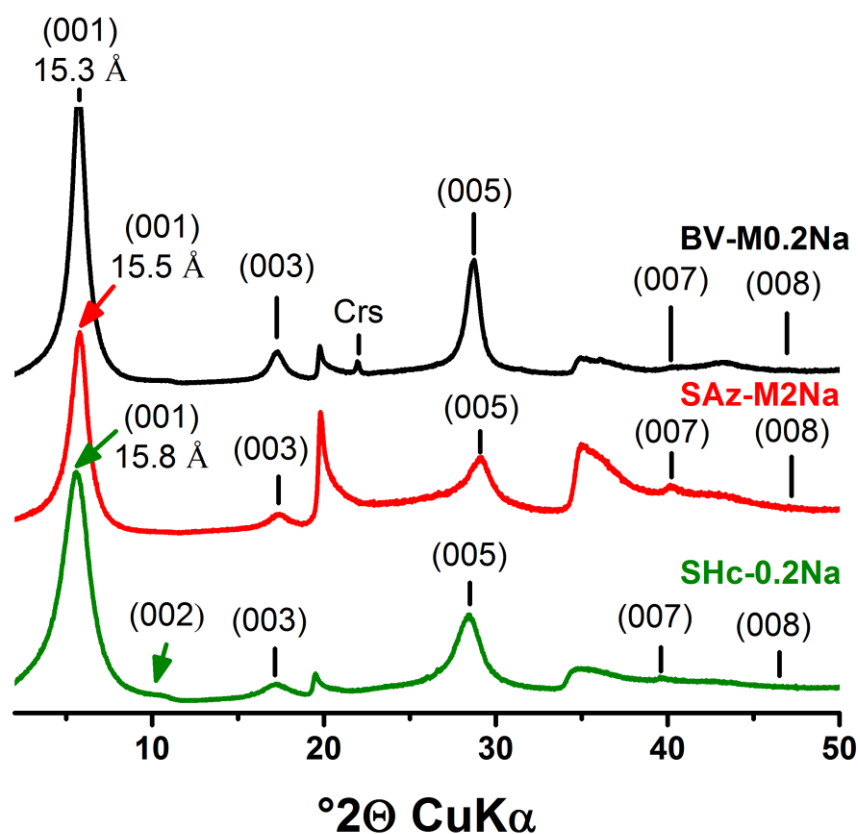
Figure 9.1 XRD patterns of powder samples BV-M0.2Na, SAz-M2Na and SHc-0.2Na stored at 86% r.h. above saturated KCl; Crs = Cristobalite.
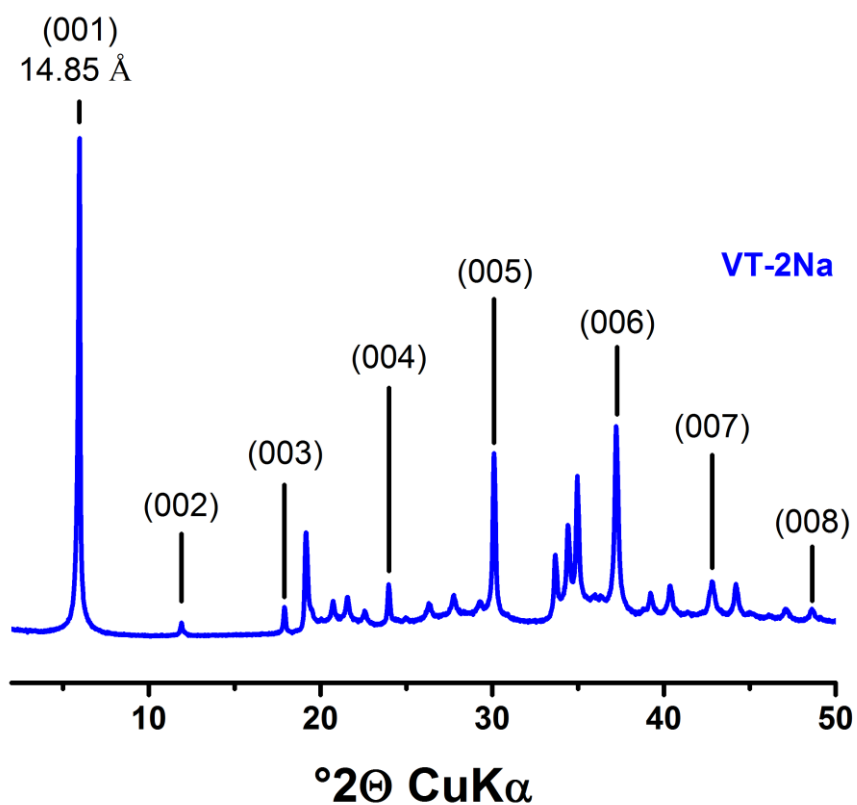
Figure 9.2 XRD patterns of powder sample VT-2Na stored at 86% r.h. above saturated KCl.

The lowest humidity achieved with the FTIR/gravimetric cell was 2 % r.h.. Even at this low r.h. value, the FTIR spectra showed that some H_2O was retained by the sample (Figure 9.3). The dry mass of the sample was obtained by plotting the intensity of δ(H-O-H) band against the gravimetric mass of the sample. Based on the measured CEC, the water content in H_2O per Na^+ was calculated.
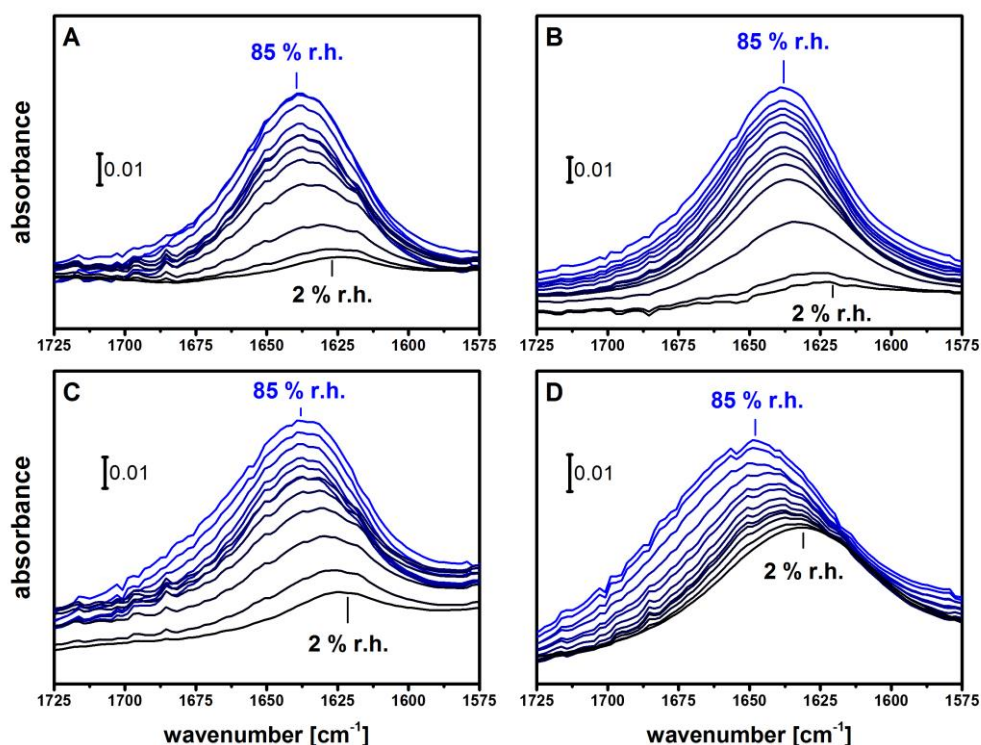
Figure 9.3 Infrared spectra of (A) BV-M0.2Na, (B) SAz-M2Na and (C) SHc-0.2Na and (D) VT-2Na as a function of relative humidity (from 85 to 2 % r.h.); all spectra are referenced to the dry ZnSe window.

Water vapor sorption isotherms

The calculated water content was correlated to each r.h. step (Figure 9.4). Continuous decreasing of the r.h. resulted in reducing the number of H_2O per Na^+ (Figure 9.4). At 86 % r.h., a water content of 12.3 H_2O / Na^+ was calculated for BV-M0.2Na. First, a nearly linear decrease of water content was observed from a r.h. of 85 % to 50 % with a water content ranging from 12.3 to 9.2 H_2O / Na^+. At 43 % r.h., the water content decreased significantly to 7.5 H_2O / Na^+. Subsequently, an almost linear decrease of water content was observed again (from 35 % to 8 % with H_2O / Na^+ ranging from ≈ 7 to 4), followed by a drop with a resulting water content of 3 H_2O / Na^+ at 2 % r.h.. The adsorption of water vapor proceeded differently. Three different slopes could be identified in water adsorption. At low r.h. (from 2 % to 40 %), a nearly linear increase could be observed. The correlated water content ranged from 3 to 4 H_2O / Na^+. A first change of slope in the adsorption branch was observed at 50 % r.h.. Here, the water content changed from 4 to 7 H_2O / Na^+. At 70 % r.h., the slope changed significantly and reached a water content of 10.5 H_2O / Na^+ at 85 % r.h..

The desorption branch of the isotherm of SAz-M2Na exhibited a similar shape compared to one of BV-M0.2Na. At 85 % r.h., a water content of 13 H_2O / Na^+ was calculated for SAz-M2Na. First, the water content decreased nearly linear down to 9 H_2O / Na^+ at 50 % r.h.. A transition point at ≈ 40 % r.h. was observed, followed by a linear decrease of water content (from 33 % to 11 % r.h with H_2O / Na^+ ranging from ≈ 7 to 6). At < 10 % r.h., a drop in water content was observed. The lowest water content was 2 H_2O / Na^+ at 2 % r.h.. The adsorption branch of the water vapor sorption isotherm of SAz-M2Na proceeded differently and, hence, hysteresis could be observed. A significantly larger hysteresis was observed for BV-M0.2Na compared to SAz-M2Na. Between 2 % and 18 % r.h., a first nearly linear increase in water content could be observed, followed by a change in slope at ≈ 20 % r.h. and correlated water content of 4 H_2O / Na^+. A second change of slope in the adsorption branch was observed at 35 % r.h.. Here, the water content changed from 5 to 9 H_2O / Na^+. At ≈ 60 % r.h., the gradient changed significantly. At 84 % r.h., a highest water content of 12.5 H_2O / Na^+ was achieved.

The hysteresis observed on the water vapor sorption isotherm for SHc-0.2Na was similar to those of the two dioctahedral samples. At 85 % r.h., a water content of 12.4 H_2O / Na^+ was calculated for SHc-0.2Na. Only small changes in water content could be observed at high r.h. (between 85 and 70 %). Then, a nearly linear decrease of water content was observed from a r.h. of ≈ 60 % to 40 % with a water content ranging from ≈ 11 to 7 H_2O / Na^+. Subsequently, an almost linear decrease of water content with a changed gradient was observed from ≈ 6 to 3 H_2O / Na^+ between ≈ 40 % and 10 % r.h.. Like the two dioctahedral smectites, on the desorption branch of SHc-0.2Na a drop in water content was observed at < 10 % r.h with a minimum water content of 1 H_2O / Na^+ at 2 % r.h.. In the case of water adsorption, a marked change in the gradient at ≈ 50 % r.h. could be observed. In the beginning the water content increased from ≈ 1 to 5 H_2O / Na^+ (from 3 % to 40 % r.h.) and then from ≈ 6 to 11 H_2O / Na^+.

In contrast, on the desorption branch of the isotherm of VT-2Na two ranges and a clear transition could be identified: from 8 to 6 H_2O / Na^+ and second from 4 to 2 H_2O / Na^+. The transition from these two nearly linear ranges was observed between ≈ 40 % and 30 % r.h.. Up to 25 – 30 % r.h. the adsorption of water vapor followed the same water content as in the desorption branch. From 30 % r.h. the adsorption of water vapor

proceeded differently and, hence, hysteresis was observed. However, the extent of hysteresis is noticeable smaller compared to the smectite samples (Figure 9.4).

According to the theoretical models for dioctahedral smectites with only one layer charge, discrete water layers were formed upon de- and adsorption of water (Emmerich et al., 2015). However, the selected natural smectites exhibit a heterogeneous layer charge distribution and, accordingly, different hydration states can coexist even under controlled conditions. Due to this coexistence, ranges in the de- and adsorption of water vapor with a slightly increasing slope were observed. In contrast, the high-charged VT-2Na exhibits a specific layer charge and, accordingly, hydration steps with a clear transition between 6 and 4 H_2O / Na^+ could be assigned. These transitions could not be clearly identified in the smectite isotherms. However, the results indicated that along these water vapor sorption isotherms from the montmorillonite and hectorite samples at least two hydration states (2W and 1W) with different hydration dynamics could be observed. On the desorption branch, water contents ranging from 13 to 8 H_2O / Na^+ and 8 to 4 H_2O / Na^+ correspond to domains dominated by 2W and 1W states (Figure 9.4 A-C). Both adsorption branches of the low-charged samples (BV-M0.2Na and SHc-0.2Na) showed a noticeable change in the gradient at 50 % r.h. indicating the transition from 1W to 2W state. For the higher charged SAz-M2Na, the transition from 1W to 2W state shifted to a lower water content of 3 H_2O / Na^+. On the desorption branch of all smectite isotherms, a marked change in the gradient was observed at < 10 % r.h., indicating the transition from 1W to 0W. Reaching a water content below 1W state also caused hysteresis at low r.h., which was not observed for VT-2Na. Whereas hysteresis was observed over the entire isothermal range of the smectites, the isotherm of VT-2Na only showed hysteresis in the transition from 1W to 2W (Figure 9.4 D). These findings indicated that hysteresis is a function of the layer charge distribution and the minimum achieved water content. In addition, the particle size of the selected materials revealed that the extent of hysteresis also depends on the morphological character since a larger hysteresis was observed for the coarser BV-M0.2Na compared to the other smectite samples. As a result, increasing the edge site proportion resulted in an increased hysteresis.
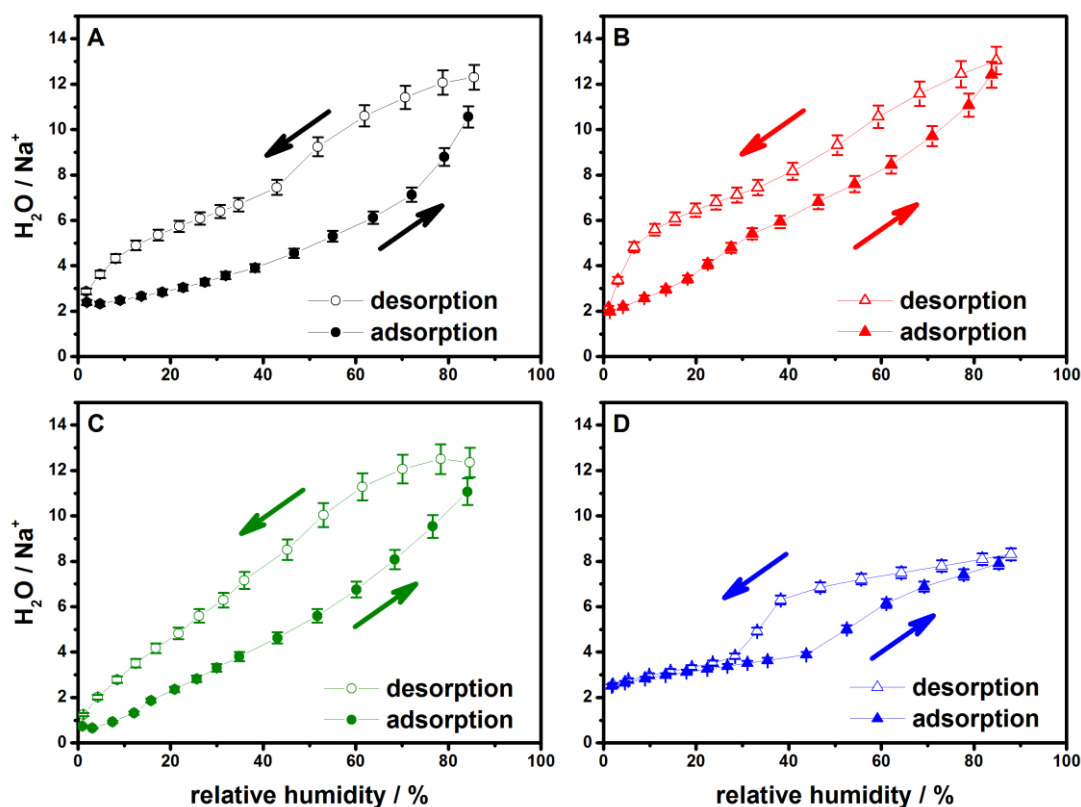
Figure 9.4 Water vapor sorption isotherm from (A) BV-M0.2Na, (B) SAz-M2Na, (C) SHc-0.2Na and (D) VT-2Na at 25 °C. The precision of the humidity sensor was determined to be ± 1 % r.h. and, therefore, to be neglected. Arrows indicating the direction of the experiment.

Infrared Spectroscopy

To examine the relationship between the desorption and adsorption isotherms and the spectroscopic data, all isotherms were compared to the corresponding IR data. For each data point shown on Figure 9.4, a corresponding FTIR spectrum was obtained using the FTIR/gravimetric cell described in chapter 4.2.2. The position of the δ(H-O-H) band was plotted in Figure 9.5 as a function of water content. The wavenumber from δ(H-O-H) provides information on the chemical structure of H_2O. The shifting of δ(H-O-H) to lower wavenumber indicated an ordered arrangement of the H_2O molecules at water contents < 4 H_2O / Na^+. For simplicity, the term 'ice-like' water was introduced because of their similarity in structure to water molecules in bulk ice (Hagen and Tielens, 1982; Richmond, 2002). The FTIR results showed that the shift of δ(H-O-H) by means of a change from 'liquid-like' water to an 'ice-like' water was also

influenced by the layer charge, charge location and octahedral substitutions (Figure 9.5).

This part is organized as follows: First, two montmorillonite samples with a different layer charge and approximately the same charge distribution were compared. Second, with regards to its (de)hydration behavior the exceptional position of vermiculite with a higher layer charge and specific charge distribution compared to the other studied samples will be discussed. Finally, comparing a di- and trioctahedral sample with about the same layer charge.
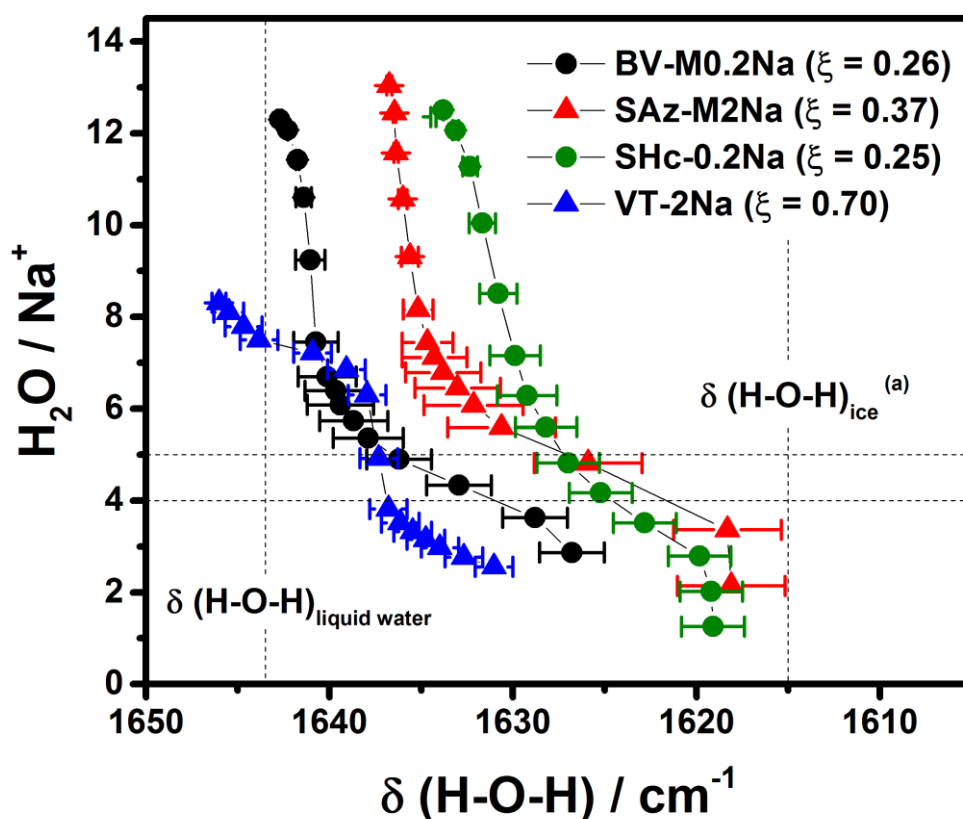
Figure 9.5 Evolution of δ(H-O-H) as a function of water content. (a) IR frequency for polycrystalline ice at 140 K [75]. An error bar (σ^2_x) for the band position of δ(H-O-H) was observed for each sample. σ^2_x was based on the highest possible variation upon desorption and adsorption of water vapor during the experiment.

Influence of layer charge

SAz-M2Na and BV-M0.2Na are dioctahedral smectites with a different layer charge. Compared to SAz-M2Na, δ(H-O-H) of the low-charged BV-M0.2Na was observed at higher wavenumbers along the water vapor sorption isotherm. Starting the experiment in the 2W state δ(H-O-H) was similar to liquid water for BV-M0.2Na (Figure 9.5). For BV-M0.2Na, δ(H-O-H) appeared at wavenumbers > 1640 cm^{-1} at water contents > 6 H_2O / Na^+ and shifted to 1627 cm^{-1} by lowering the water content down to 2 H_2O / Na^+. By adsorbing of water vapor, δ(H-O-H) followed the same wavenumber steps with σ^2_x ± 2 cm^{-1}. A similar trend could be observed for SAz-M2Na, however, the wavenumber for δ(H-O-H) was 6 cm^{-1} lower for water contents > 6 H_2O / Na^+ compared to BV-M0.2Na. At water contents < 6 H_2O / Na^+, δ(H-O-H) shifted to 1618 cm^{-1}. σ^2_x for SAz-M2Na was observed to be ± 3 cm^{-1} (Figure 9.5).

These results indicated that increasing the layer charge from 0.26 to 0.37 per f.u. resulted in a highly ordered arrangement of H_2O molecules, which could be observed as a lower wavenumber position of δ(H-O-H) (Figure 9.5). The effect of the wavenumber position of δ(H-O-H) could also be derived from Figure 9.6 A and B. Figure 9.6 A shows a side view rotated 30 degrees around [001] of MMT0.25 and depict a 1W state with 4 H_2O / Na^+. Three water molecules have a bond angle between 107.5 and 108.3 ° showing the strongly polarized character in 1W state. The fourth water molecule exhibits a lower bond angle of 105.5 °, which indicates the start of reorientation. For MMT0.25, there are no water-water interactions at this stage of the hydration (Figure 9.6 A), while at 4 H_2O / Na^+ for MMT0.5 water interacts with the basal surface as well with other adjacent water molecules by forming hydrogen bonds (Figure 9.6 B). The picture clearly shows that for the higher charged model MMT0.5 at 4 H_2O / Na^+ the interlayer cation to cation distances are reduced to 6.26 Å compared to the MMT0.25 model with 8.98 Å (Figure 9.6 A and B). As a consequence, the interlayer cations are forced to move out of the mid-plane (Figure 9.6 B) since the hydration of the Na^+ and its high hydration enthalpy is for water molecules the most attractive interaction. As a result, the water molecules are in a constrained environment relative to those of MMT0.25 at 4 H_2O / Na^+ and, hence, a lower wavenumber position of δ(H-O-H) was observed for the higher layer charge.

Na⁺-saturated vermiculite

The shifting of δ(H-O-H) from VT-2Na followed the same form as its water vapor sorption isotherm (Figure 9.4 and 9.5). At a water content between 8 and 6 H_2O / Na^+, a gradual shift from 1646 cm^{-1} to 1638 cm^{-1} was observed for δ(H-O-H), followed by a sharp drop in water content from 6 to 4 H_2O / Na^+. Between 3 and 4 H_2O / Na^+, δ(H-O-H) shifted from 1637 cm^{-1} to 1631 cm^{-1}. $σ^2_x$ for VT-2Na was observed to be ± 1 cm^{-1}. The transition of these two stages was found on the intersection point of SAz-M2Na and SHc-0.2Na.

The comparison of BV-M0.2Na and SAz-M2Na clearly showed that increasing the layer charge from 0.25 to 0.37 per f.u. resulted in an ordered arrangement of water molecules. VT-2Na exhibits an even larger layer charge as SAz-M2Na, but a higher wavenumber of δ(H-O-H) was observed. These results indicated that increasing the layer charge firstly resulted in an ordered arrangement of H_2O molecules. However, further increasing of layer charge turned into a seemingly disordering. This can be explained by an additional disorder, which the increased amount of Na^+ bring into the water layer by forming the hydration shell. Due to the increased layer charge, the interlayer cations with their hydration shell moving out of the mid-plane (see Figure 9.6 B). In addition, the cation to cation distances constantly decreased by increasing the layer charge. Considering the interlayer cations as small point defects in the water layers, the interaction of water molecules behaves different compared to the formation in an electric double layer model. The electronic structure calculations of MMT0.25 and MMT0.5 showed that the water layers corresponding to a high chemical potential of Na^+ approaches the value of bulk water, which is in accordance with our experimental findings. Thus, these findings indicated that the highest ordered arrangement of H_2O molecules lies somewhere between 0.37 and 0.70 per f.u..

Influence of octahedral substitutions

The shift of δ(H-O-H) of the low-charged trioctahedral SHc-0.2Na followed the same shape as the two dioctahedral smectite samples and intersected at ≈ 5 H_2O / Na^+ with the line of SAz-M2Na (Figure 9.5). Higher wavenumbers were observed above the point of intersection, and lower wavenumber below a water content of 5 H_2O / Na^+. δ(H-O-H) shifted from 1632 cm^{-1} (12 H_2O / Na^+) to 1619 cm^{-1}, which was comparable to the shift of δ(H-O-H) from higher-charged SAz-M2Na (1636 to 1618 cm^{-1}). In the

previous chapter, it was showed that at low water contents (< 3 H_2O / Na^+) the hydration shell around each Na^+ coincides with the surface/water interaction via hydrogen bonds and no water-water interactions exist for a low charged dioctahedral montmorillonite. The same can be observed for a trioctahedral hectorite. At a water content of 4 H_2O / Na^+, δ(H-O-H) from SHc-0.2Na was observed at 1625 cm^{-1}, while δ(H-O-H) from BV-M0.2Na was observed at 1630 cm^{-1} (Figure 9.5). These findings implied that a trioctahedral structure leads to stronger interactions from interlayer water and the tetrahedral sheet compared to a dioctahedral composition. The calculation of HCT0.25 confirmed this result. Figure 9.6 C shows an energetically favorable model of HCT0.25 and represents a 1W state with 4 H_2O / Na^+. The water molecules have an average bond angle of 107.5 ° and, accordingly, even larger compared to those of MMT0.25. As a result, a lower wavenumber position of δ(H-O-H) was observed for SHc-0.2Na. Finally, the calculation of the model HCT0.25 confirmed that the structural O-H groups of trioctahedral hectorite are vibrating almost perpendicular to the planar surface (Figure 9.6).

It was showed that the layer dimension determines the edge site properties. Di- and trioctahedral smectites display structural heterogeneities and variation in size. The particle size of VT-2Na is much larger, which was confirmed by the average CSD thickness and, accordingly, the coarser material had a noticeable lower edge site contribution. As proposed in earlier studies on osmotic hydrates (Tester et al., 2016), the smaller basal spacings in 2W and 1W state for VT-2Na result from a larger number of layers per stack and, hence, a higher contribution of long-range vdW forces. Domains in the de- and adsorption of water vapor of the smectite samples with a slightly increasing slope were explained by a heterogeneous layer charge distribution, which enables the coexistence of different hydration states even under controlled conditions. It was also showed that hysteresis is a function of the layer charge distribution, the achieved water content and the particle size with resulting edge site contribution. Increasing the edge site proportions resulted in an increased hysteresis. The findings from the experimental FTIR/gravimetric analysis showed that the transition from 2W to 1W and backwards is visible using IR spectroscopy. The transition (forward and backward) from bi- to mono-hydrated state is dominated by breaking and formation of hydrogen bonds within water layers. The shift of δ(H-O-H) to lower wavenumbers was correlated to an increase of water-surface attraction. This shifting of δ(H-O-H) was also influenced by the layer charge, charge distribution,

octahedral substitutions and the layer dimension. As the layer charge increases from 0.26 to 0.37 per f.u., the wavenumber of δ(H-O-H) decreases, corresponding increased interactions from interlayer water and the surface of the tetrahedral sheet. The same increased water-surface attractions were observed for Li^+ for Mg^{2+} substitutions in the octahedral sheet compared to Mg^{2+} for Al^{3+} substitutions. Increasing the layer charge above 0.5 per f.u. resulted in a disordered interlayer water arrangement similar to those of bulk water and, accordingly, a higher wavenumber of δ(H-O-H) for VT-2Na was observed. This effect was explained by considering the Na^+ as small point defects in the water layers. The hydration of the Na^+ and its high hydration enthalpy is for water molecules the most attractive interaction. As a consequence, the cations are forced to move out of the mid-plane, which resulted in a decreased cation to cation distance from 8.98 Å to 6.26 Å.

Nevertheless, there is a lack in quantitative understanding of stable hydration states in dependence of layer charge covering the full range from 0.125 to 0.5 mol(+)/f.u. together with charge distribution over tetrahedral and octahedral sheets. A quantitative description is the next step of the ongoing project that will enhance the understanding of heterogeneous swelling of smectites.
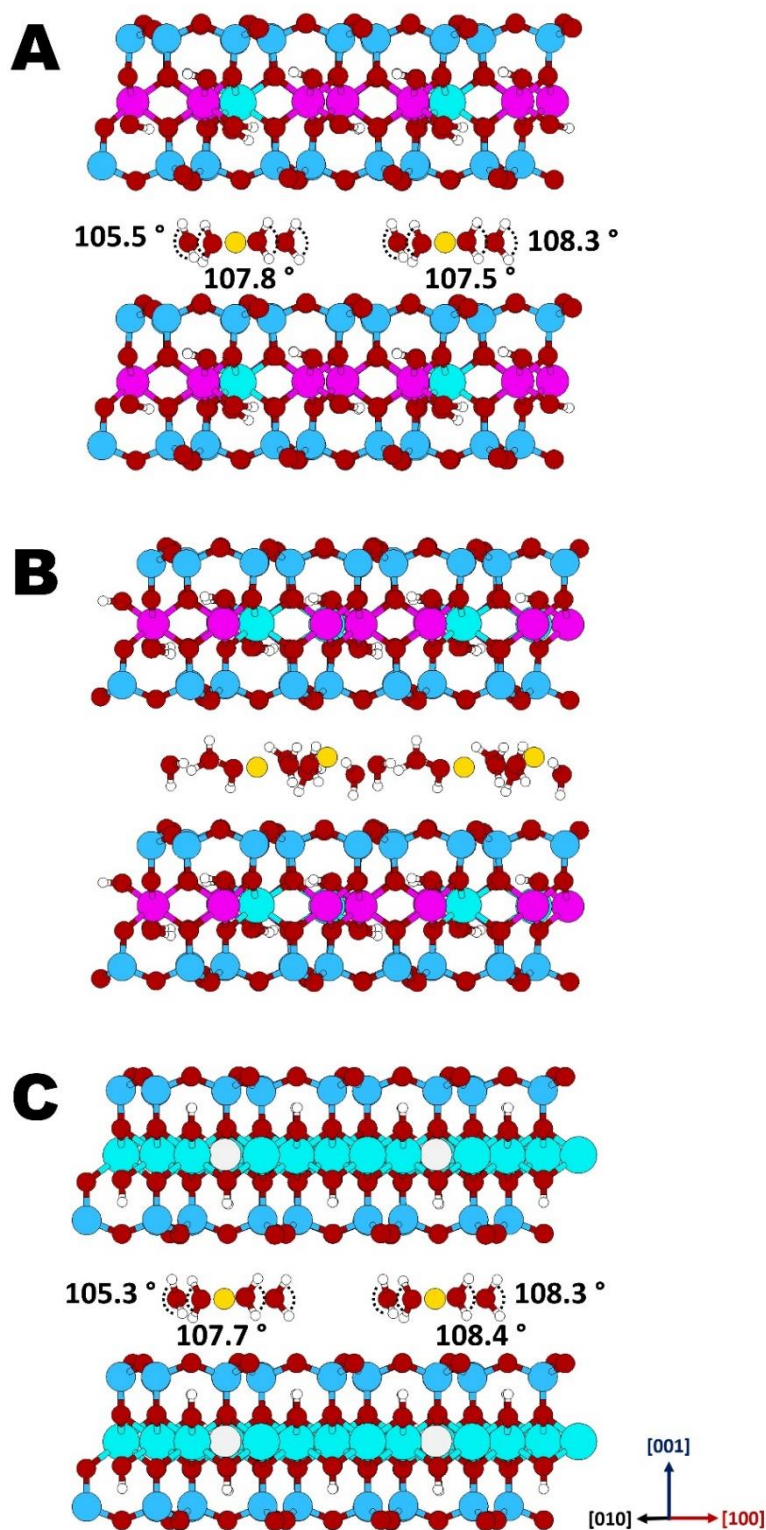
Figure 9.6 Side view rotated 30 degrees around [001] on energetically favorable
(A) $[Na_1(Si_{16})(Al_7Mg_1)O_{40}(OH)_8]$ x 4 H_2O -; (B) $[Na_2(Si_{16})(Al_6Mg_2)O_{40}(OH)_8]$ x 8 H_2O - and
(C) $[Na_1(Si_{16})(Mg_{11}Li_1)O_{40}(OH)_8]$ x 4 H_2O interface. Blue spheres represent Si, red spheres
represent O of the MMT0.25, MMT0.5 and HCT0.25 and white spheres represent H. (A+B)
the Mg-defect is represented by a cyan sphere inside the dioctahedral sheet, pink spheres
represent Al. (C) The Li-defect is represented by a white sphere inside the trioctahedral
sheet and Na is represented as yellow sphere.

9.5   Conclusions

The purpose of this study was to investigate the influence of the structural heterogeneity of the silicate layers on hydration properties using FTIR with emphasis on the sorbed H_2O bands. In the first part of this manuscript the layer dimension and stacking was determined, which clarified the differences in edge site proportions of the selected 2:1 layer silicates. In all samples, hysteresis occurred in water vapor sorption isotherms. Whereas hysteresis was observed over the entire isothermal range of the smectites, the isotherm of VT-2Na only showed hysteresis in the transition from 1W to 2W state. Hysteresis is a function of the layer charge distribution and the achieved water content. The particle size of the selected materials revealed that the extent of hysteresis also depends on the morphological character. Increasing the edge site contribution resulted in an increased hysteresis.

Hysteresis had a smaller effect on the band positions of δ(H-O-H) expressed in a small error bar compared to gravimetrical water vapor sorption isotherms, which are kinetically controlled. δ(H-O-H) reflected the change from 1W to 2W state and can, therefore, be used as molecular probe for water-smectite and water-vermiculite interactions. With the help of first-principles calculations, the different shifting behavior of δ(H-O-H) related to the differences in surface charge density and octahedral compositions were explained. At low water contents (< 4 H_2O / Na^+), interlayer water and the tetrahedral sheet form strong bindings via hydrogen bonds, which was observed as a shifting of δ(H-O-H) to lower wavenumbers. At a layer charge of 0.37 per f.u., strong interactions were clearly more distinct since a larger shift for δ(H-O-H) from SAz-M2Na compared to BV-M0.2Na was observed. The low-charged trioctahedral SHc-0.2Na had an equivalent shift as SAz-M2Na, which indicates that Li^+ for Mg^{2+} substitutions in the octahedral sheet compared to Mg^{2+} for Al^{3+} substitutions leads to strong interactions from interlayer water and the tetrahedral sheet. An interlayer water arrangement similar to those of bulk water was found for VT-2Na since the increased layer charge is followed by an additional disorder considering the Na^+ as small point defects in the water layers. As a result, the water arrangement in 2:1 layer silicates depends on many factors such as the structural intrinsic properties (e.g. layer charge, charge distribution and octahedral composition) and the layer dimension with resulting edge site proportions.

10 Conclusion – Perspectives

The ability to probe complex mineral interfaces on an atomic scale has led to detailed insights into how water reacts with surfaces of 2:1 layer silicates. In the present work, the combined use of theoretical and experimental methods allowed to elucidate the coupled processes of (de-)hydration and changes in the 2:1 layer as well as a fundamental understanding on the process of swelling hysteresis. In the first case, investigations of the coupled processes of dehydration and Si-O phonon mode evolution have been done by FTIR allowing consideration of all structural changes of the montmorillonite layers during dehydration. With the help of first-principles calculations, a new model of the structural change in all three dimensions of the tetrahedral and octahedral layer during the release of interlayer water was developed. The observed shift of δ(H-O-H) and (Si-O)^{LO} to lower wavenumbers can now be correlated to an increase of water-surface attraction, which means that the water molecules are highly polarized in the mono-hydrated state (1W layer) and have a lower O-H bending mode (1628 cm^{-1}) compare to liquid water (1643 cm^{-1}). The increase of surface-water attractions with increasing temperature was displayed in a coupled shift of the longitudinal optical Si-O phonon mode to lower wavenumber. As a result, the lateral dimension of the 2:1 layer decrease as the water content decreases, resulting in a volume decrease along the a- and b-axis. The term first-principles indicates that the used calculations do not rely on empirical or fitted parameters. In this sense, these calculations are applicable for a wide range of realistic conditions such as realistic environmental situations of varying chemical conditions, temperatures and pressures.

Particular interest was focused on the different emphasis of hysteresis. Thereby, an understanding of hydration hysteresis of swelling 2:1 layer silicates was only possible through a comprehensive material characterization including all heterogeneities (e.g. shape of the selected materials, particle size with resulting edge site proportion). It was shown that the layer dimension determines the edge site properties and hysteresis is a function of the layer charge distribution and the achieved water content. The particle size of the selected materials revealed that the extent of hysteresis also depends on the morphological character. Increasing the edge site contribution resulted in an increased hysteresis.

As a result, the fundamental understanding derived from this work is of broad interest to the environmental science community since the comprehensive view of distinct intrinsic structural properties of 2:1 layer silicates on the process of heterogeneous swelling have not been considered previously. In particular, bentonites are commonly used as a barrier material due to their high swelling ability. Thus, understanding the molecular mechanism of hysteresis in clay swelling is a pre-requisite for controlling and monitoring engineered clayey barriers.

Na⁺-rich bentonites as barrier material for radioactive waste

To store safely the amount of high-level radioactive waste (HLRW) is a major challenge for the whole world. Most repository concepts consist of a multi-barrier system that includes an engineered barrier. Thereby, bentonites are the foreseen materials for usage as a geotechnical barrier between the metal canister containing the radioactive waste and the host rock. The decisive feature of bentonites is their low hydraulic conductivity, high self-sealing ability and stability (Sellin and Leupin, 2013). However, still open questions remain with respect to distinguish between more and less suitable bentonites for storage of HLRW (Kaufhold and Dohrmann, 2016). Indeed, the usage of a bentonite which has been investigated extensively means less uncertainty. Within this thesis bentonites such as the blended Calcigel® and Volclay® were selected and already been thoroughly investigated (Delavernhe et al., 2015; Emmerich, 2000; Wolters and Emmerich, 2007). The Na⁺-saturated BV-M0.2Na showed a complete reversible swelling even after dehydration at 300 °C, which demonstrated that the swelling capacity was not loosed upon heating. Not to lose the swellability is one of the key issues of bentonite as a geotechnical barrier in HLRW repositories. However, from an engineering point of view, additional structural aspects must be considered, e.g. dependence of the hydraulic conductivity and swelling pressure on the dry density.

T-BAG preparation for future applications

In this work, T-BAG was applied on clays for the first time. Thin films of 200 nm of the pure smectite sample were prepared on the silicon wafers and scanning electron microscopy confirmed that T-BAG is perfectly reproducible for the use of clay minerals in future. The determination of the longitudinal optical Si-O phonon mode (Si-O)^{LO} was firstly used for 2:1 layer silicates. The work demonstrated the ability of the LO phonon mode to analyze coupled processes of dehydration and changes in the 2:1 layer of a

Na$^+$-exchanged dioctahedral smectite using *in situ* IR transmission spectroscopy. In this investigations, the coated wafer was mounted on a heatable sample holder in an oxygen free atmosphere under N$_2$ purging and analyzed with FTIR transmission spectroscopy. The temperature of the sample was increased from room temperature to 300 °C to determine the stepwise release from interlayer water. However, using this approach higher temperatures (> 1000 °C) can be achieved. Preliminary results in the temperature range between 500 and 800 °C showed that beside the $(SiO)^{LO}$ further vibrational bands such as the loss of the $\delta(M^{x+}N^{y+}\text{-}OH)$ occurred. This results indicated that this method is suitable to detect only small changes in the clay structure. The exact temperature of the loss of the structural hydroxyl group can be observed. Consequently, a new analytical tool to determine the dehydroxylation behavior of 2:1 layer silicates was provided.

Water content

The precise determination of water content is crucial for a wide range of technical and geotechnical applications. In most cases, samples are heated at 105 °C for 24 h and analyzed by weighing them before and after heating. However, heating at 105 °C will not dehydrate clayey materials or soils completely. The residual water content could be as high as 6 % (Kaden, 2012). In this work, isothermal long-time measurements under N$_2$ purging ($\approx$ 0 % r.h.) showed that a complete dehydration of the selected 2:1 layer silicates was not achieved under ambient conditions. The largest residual moisture was measured in the vermiculite sample. However, preliminary results showed that a temperature of 80 °C and N$_2$ purging over 24 h is required to fully dehydrate the vermiculite sample.

11 References

(1998) IEEE Standard Definitions of Terms for Radio Wave Propagation. IEEE Std 211-1997, i.

Acik, M., Lee, G., Mattevi, C., Chhowalla, M., Cho, K. and Chabal, Y.J. (2010) Unusual infrared-absorption mechanism in thermally reduced graphene oxide. Nature Materials 9, 840-845.

Anderson, R.L., Ratcliffe, I., Greenwell, H.C., Williams, P.A., Cliffe, S. and Coveney, P.V. (2010) Clay swelling - A challenge in the oilfield. Earth-Sci. Rev. 98, 201-216.

Argüelles, A., Leoni, M., Blanco, J.A. and Marcos, C. (2010) Semi-ordered crystalline structure of the Santa Olalla vermiculite inferred from X-ray powder diffraction. American Mineralogist 95, 126-134.

Aziz, H.A., Böhme, M., Rocholl, A., Prieto, J., Wijbrans, J.R., Bachtadse, V. and Ulbig, A. (2010) Integrated stratigraphy and 40Ar/39Ar chronology of the early to middle Miocene Upper Freshwater Molasse in western Bavaria (Germany). International Journal of Earth Sciences 99, 1859-1886.

Bailey, S.W. (1982) Niomenclature for regular interstratifications. Am. Mineral. 67, 394-398.

Bailey, S.W., Frank-Kamenetskii, V.A., Goldsztaub, S., Kato, A., Pabst, A., Schulz, H., Taylor, H.F.W., Fleischer, M. and Wilson, A.J.C. (1977) Report of the International Mineralogical Association (IMA)-International Union of Crystallography (IUCr) Joint Committee on Nomenclature. Acta Crystallographica Section A 33, 681-684.

Benedict, W.S., Gailar, N. and Plyler, E.K. (1956) Rotation-Vibration Spectra of Deuterated Water Vapor. The Journal of Chemical Physics 24, 1139-1165.

Bérend, I., Cases, J.M., Francois, M., Uriot, J.P., Michot, L.J., Masion, A. and Thomas, F. (1995) Mechanism of adsorption and desorption of water vapor by homoionic montmorillonite: 2. The Li^+, Na^+, K^+, Rb^+ and Cs^+-exchanged forms. Clays Clay Miner. 43, 324-336.

Bergaya, F. and Lagaly, G. (2013) Chapter 1 - Introduction to Clay Science: Techniques and Applications, in: Faïza, B., Gerhard, L. (Eds.), Developments in Clay Science. Elsevier, pp. 1-7.

Berreman, D.W. (1963) Infrared Absorption at Longitudinal Optic Frequency in Cubic Crystal Films. Phys Rev 130, 2193-2198.

Besson, G. and Drits, V.A. (1997a) Refined Relationships between Chemical Composition of Dioctahedral Fine-Grained Mica Minerals and Their Infrared Spectra within the OH Stretching Region. Part I: Identification of the OH Stretching Bands. Clays Clay Miner. 45, 158-169.

Besson, G. and Drits, V.A. (1997b) Refined Relationships between Chemical Composition of Dioctahedral Fine-Grained Micaceous Minerals and Their Infrared Spectra within the OH Stretching Region. Part II: The Main Factors Affecting OH Vibrations and Quantitative Analysis. Clays Clay Miner. 45, 170-183.

Besson, G., Mifsud, A., Tchoubar, C. and Mering, J. (1974) Order and Disorder Relations in the Distribution of the Substitutions in Smectites, Illites and Vermiculites. Clays and Clay Minerals 22, 379-384.

Beyer, J. and Graf von Reichenbach, H. (2002) An extended revision of the interlaxer structures of one- and two-layer hydrates of Na-Vermiculite. Clay Minerals 37, 157-168.

Bittelli, M., Valentino, R., Salvatorelli, F. and Rossi Pisa, P. (2012) Monitoring soil-water and displacement conditions leading to landslide occurrence in partially saturated clays. Geomorphology 173–174, 161-173.

Boek, E.S., Coveney, P.V. and Skipper, N.T. (1995a) Molecular Modeling of Clay Hydration: A Study of Hysteresis Loops in the Swelling Curves of Sodium Montmorillonites. Langmuir 11, 4629-4631.

Boek, E.S., Coveney, P.V. and Skipper, N.T. (1995b) Monte Carlo Molecular Modeling Studies of Hydrated Li-, Na-, and K-Smectites: Understanding the Role of Potassium as a Clay Swelling Inhibitor. Journal of the American Chemical Society 117, 12608-12617.

Bonaccorsi, E., Merlino, S. and Taylor, H.F.W. (2004) The crystal structure of jennite, $Ca9Si6O18(OH)(6)$center dot $8H(2)O$. Cement and Concrete Research 34, 1481-1488.

Bosbach, D., Charlet, L., Bickmore, B. and Hochella, M.F.J. (2000) The dissolution of hectorite: In-situ, real-time observations using atomic force microscopy. American Mineralogist 85, 1209-1216.

Bourg, I.C., Bourg, A.C.M. and Sposito, G. (2003) Modeling diffusion and adsorption in compacted bentonite: A critical review. Journal of Contaminant Hydrology 61, 293-302.

Bourg, I.C. and Tournassat, C. (2015) Chapter 6 - Self-Diffusion of Water and Ions in Clay Barriers, in: Christophe Tournassat, C.I.S.I.C.B., Faφza, B. (Eds.), Developments in Clay Science. Elsevier, pp. 189-226.

Boutareaud, S., Calugaru, D.-G., Han, R., Fabbri, O., Mizoguchi, K., Tsutsumi, A. and Shimamoto, T. (2008) Clay-clast aggregates: A new textural evidence for seismic fault sliding? Geophysical Research Letters 35, n/a-n/a.

Bradbury, K.K., Davis, C.R., Shervais, J.W., Janecke, S.U. and Evans, J.P. (2015) Composition, Alteration, and Texture of Fault-Related Rocks from Safod Core and Surface Outcrop Analogs: Evidence for Deformation Processes and Fluid-Rock Interactions. Pure and Applied Geophysics 172, 1053-1078.

Bradbury, M.H. and Baeyens, B. (2003) Porewater chemistry in compacted re-saturated MX-80 bentonite. Journal of Contaminant Hydrology 61, 329-338.

Brigatti, M.F., Galán, E. and Theng, B.K.G. (2013) Chapter 2 - Structure and Mineralogy of Clay Minerals, in: Faïza, B., Gerhard, L. (Eds.), Developments in Clay Science. Elsevier, pp. 21-81.

Brigatti, M.F. and Guggenheim, S. (2002) Mica crystal chemistry and the influence of pressure, temperature, and solid solution on atomistic models, in: Mottana, A., Sassi, F.P., Thompson, J.B., Guggenheim, S. (Eds.), Micas: Crystal Chemistry and Metamorphic Petrology. Reviews in Mineralogy and Geochemistry. Mineralogical Society of America, Washington D.C., pp. 1-97.

Brindley, G.W. and Brown, G. (1984) Crystal structures of clay minerals and their X-Ray identifikation. Mineralogical Society Monograph No. 5, 41 Queen's Gate, London SW7 5HR.

Brunauer, S., Emmett, P.H. and Teller, E. (1938) Adsorption of Gases in Multimolecular Layers. Journal of the American Chemical Society 60, 309-319.

Cadene, A., Durand-Vidal, S., Turq, P. and Brendle, J. (2005) Study of individual Na-montmorillonite particles size, morphology, and apparent charge. Journal of Colloid and Interface Science 285, 719-730.

Cases, J.M., Bérend, I., Besson, G., Francois, M., Uriot, J.P., Thomas, F. and Poirier, J.E. (1992) Mechanism of adsorption and desorption of water vapor by homoionic montmorillonite. 1. The sodium-exchanged form. Langmuir 8, 2730-2739.

Cases, J.M., Berend, I., Francois, M., Uriot, J.P., Michot, L.J. and Thomas, F. (1997) Mechanism of adsorption and desorption of water vapor by homoionic montmorillonite; 3, The Mg^{2+}, Ca^{2+} and Ba^{2+} exchanged forms. Clays and Clay Minerals 45, 8-22.

Caurie, M. (2011) Bound water: its definition, estimation and characteristics. International Journal of Food Science & Technology 46, 930-934.

Chabal, Y.J., Weldon, M.K. and Queeney, K. (2001) Ultra-thin Oxides and Initial Silicon Oxidation, in: Chabal, Y.J. (Ed.), Fundamental Aspects of Silicon Oxidation. Springer Series in Material Science, p. 143.

Chang, F.-R.C., Skipper, N.T. and Sposito, G. (1995) Computer Simulation of Interlayer Molecular Structure in Sodium Montmorillonite Hydrates. Langmuir 11, 2734-2741.

Chipera, S.J. and Bish, D.L. (2001) Baseline studies of the clay minerals society source clays: Powder X-ray diffraction analyses. Clays Clay Miner. 49, 398-409.

Christidis, G.E. (2013) Chapter 4.1 - Assessment of Industrial Clays, in: Faïza, B., Gerhard, L. (Eds.), Developments in Clay Science. Elsevier, pp. 425-449.

Christidis, G.E. and Huff, W.D. (2009) Geological Aspects and Genesis of Bentonites. Elements 5, 93-98.

Dazas, B., Ferrage, E., Delville, A. and Lanson, B. (2014) Interlayer structure model of tri-hydrated low-charge smectite by X-ray diffraction and Monte Carlo modeling in the Grand Canonical ensemble. Am. Mineral. 99, 1724-1735.

Dazas, B., Lanson, B., Breu, J., Robert, J.-L., Pelletier, M. and Ferrage, E. (2013) Smectite fluorination and its impact on interlayer water content and structure: A way to fine tune the hydrophilicity of clay surfaces? Microporous Mesoporous Mater. 181, 233-247.

Dazas, B., Lanson, B., Delville, A., Robert, J.-L., Komarneni, S., Michot, L.J. and Ferrage, E. (2015) Influence of Tetrahedral Layer Charge on the Organization of Interlayer Water and Ions in Synthetic Na-saturated Smectites. J. Phys. Chem. C.

de la Calle, C. and Suquet, H. (1988) Vermiculites, in: Bailey, S.W. (Ed.), Hydrous Phyllosilicates (Exclusive of Micas). Mineralogical Society of America, Washington D.C., pp. 455-496.

De la Calle, C., Suquet, H. and Pons, C.-H. (1988) Stacking order in a 14.30-Å Mg-vermiculite. Clays and Clay Minerals 36, 481-490.

de Leeuw, N.H. and Purton, J.A. (2001) Density-functional theory calculations of the interaction of protons and water with low-coordinated surface sites of calcium oxide. Phys Rev. B 63, 195417.

Delavernhe, L., Steudel, A., Darbha, G.K., Schäfer, T., Schuhmann, R., Wöll, C., Geckeis, H. and Emmerich, K. (2015) Influence of mineralogical and morphological properties on the cation exchange behavior of dioctahedral smectites. Colloids Surf., A 481, 591-599.

Drits, V., Srodon, J. and Eberl, D. (1997) XRD measurement of mean crystallite thickness of illite and illite/smectite: Reappraisal of the Kubler index and the Scherrer equation. Clays and Clay Minerals 45, 461-475.

Drits, V.A. (2003) Structural and chemical heterogeinity of layer silicates and clay minerals. Clay Miner. 38, 403-432.

Drits, V.A., Besson, G. and Muller, F. (1995) An improved model for structural transformations of heat-treated aluminous dioctahedral 2:1 layer silicates. Clays and Clay Minerals 43, 718-731.

Drits, V.A. and McCarty, D.K. (2007) The nature of structure-bonded H_2O in illite and leucophyllite from dehydration and dehydroxylation experiments. Clays and Clay Minerals 55, 45-58.

Drits, V.A., Weber, F., Salyn, A.L. and Tsipursky, S.I. (1993) X-ray identification of one-layer illite varieties; Application to the study of illite around uranium deposits of Canada. Clays and Clay Minerals 41, 389-398.

Eisenberg, D. and Kauzmann, W. (1969) The structure and properties of water. Oxford University Press, London.

Emmerich, K. (2000) PhD thesis: Die geotechnische Bedeutung des Dehydroxylierungsverhaltens quellfähiger Tonminerale, Institut für Geotechnik (IGT). ETH Zürich, vdf Hochschulverlag AG an der ETH Zürich, p. 143.

Emmerich, K. (2010) Thermal analysis for characterization and processing of industrial minerals, in: Christidis, G.E. (Ed.), Advances in the Characterization of Industrial Minerals. EMU Notes in Mineralogy, pp. 129-170.

Emmerich, K. (2013) Chapter 2.13 - Full Characterization of Smectites, in: Faïza, B., Gerhard, L. (Eds.), Developments in Clay Science. Elsevier, pp. 381-404.

Emmerich, K., Kahr, G. and Madsen, F.T. (1999) Dehydroxylation behavior of heat-treated and steam-treated homoionic cis-vacant montmorillonites. Clays and Clay Minerals 47, 591-604.

Emmerich, K., Koeniger, F., Kaden, H. and Thissen, P. (2015) Microscopic structure and properties of discrete water layer in Na-exchanged montmorillonite. J. Colloid. Interf. Sci. 448, 24-31.

Emmerich, K., Steudel, A. and Merz, D. (2017) Dehydroxylation of dioctahedral smectites in water vapor atmosphere. Applied Clay Science 137, 1-5.

Emmerich, K., Wolters, F., Kahr, G. and Lagaly, G. (2009) Clay Profiling: The Classification of Montmorillonites. Clays and Clay Minerals 57, 104-114.

Farmer, V.C. (1968) Infrared spectroscopy in clay mineral studies. Clay Minerals 7, 373-387.

Farmer, V.C. (1974) The layer silicates, in: Farmer, V.C. (Ed.), The infrared spectra of minerals. Mineralogical Society, London.

Farmer, V.C. and Russell, J.D. (1964) The infra-red spectra of layer silicates. Spectrochimica Acta 20, 1149-1173.

Farmer, V.C. and Russell, J.D. (1971) Interlayer complexes in layer silicates. The structure of water in lamellar ionic solutions. Trans. Faraday Soc. 67, 2737-2749.

Ferrage, E. (2016) Investigation of the interlayer organization of water and ions in smectite from the combined use of diffraction experiments and molecular simulations. A review of methodology, applications, and perspectives. Clays and Clay Minerals 64, 348-373.

Ferrage, E., Hubert, F., Tertre, E., Delville, A., Michot, L.J. and Levitz, P. (2015) Modeling the arrangement of particles in natural swelling-clay porous media using three-dimensional packing of elliptic disks. Physical Review E 91.

Ferrage, E., Lanson, B., Malikova, N., Plancon, A., Sakharov, B.A. and Drits, V.A. (2005a) New insights on the distribution of interlayer water in bi-hydrated smectite from X-ray diffraction profile modeling of 00l reflections. Chemistry of Materials 17, 3499-3512.

Ferrage, E., Lanson, B., Michot, L.J. and Robert, J. (2010a) Hydration Properties and Interlayer Organization of Water and Ions in Synthetic Na-Smectite with Tetrahedral Layer Charge. Part 1. Results from X-ray Diffraction Profile Modeling. J. Phys. Chem. C 114, 4515-4526.

Ferrage, E., Lanson, B., Sakharov, B.A. and Drits, V.A. (2005b) Investigation of smectite hydration properties by modeling experimental X-ray diffraction patterns: Part I. Montmorillonite hydration properties. Am. Mineral. 90, 1358-1374.

Ferrage, E., Lanson, B., Sakharov, B.A., Geoffroy, N., Jacquot, E. and Drits, V.A. (2007) Investigation of dioctahedral smectite hydration properties by modeling of X-ray diffraction profiles: Influence of layer charge and charge location. Am. Mineral. 92, 1731-1743.

Ferrage, E., Sakharov, B.A., Michot, L.J., Delville, A., Bauer, A., Lanson, B., Grangeon, S., Frapper, G., Jimenez-Ruiz, M. and Cuello, G.J. (2011) Hydration Properties and Interlayer Organization of Water and Ions in Synthetic Na-Smectite with Tetrahedral Layer Charge. Part 2. Toward a Precise Coupling between Molecular Simulations and Diffraction Data. J. Phys. Chem. C 115, 1867-1881.

Ferrage, E., Sakharov, B.A., Michot, L.J., Lanson, B., Delville, A. and Cuello, G.J. (2010b) Water organization in Na-saponite: An experimental validation of numerical data. Geochimica Et Cosmochimica Acta 74, A289-A289.

Feyereisen, M.W., Feller, D. and Dixon, D.A. (1996) Hydrogen Bond Energy of the Water Dimer. The Journal of Physical Chemistry 100, 2993-2997.

Friedrich, F., Gasharova, B., Mathis, Y.L., Nuesch, R. and Weidler, P.G. (2006) Far-infrared spectroscopy of interlayer vibrations of Cu(II), Mg(II), Zn(II), and Al(III) intercalated muscovite. Applied Spectroscopy 60, 723-728.

Fu, M.H., Zhang, Z.Z. and Low, P.F. (1990) Changes in the properties of a montmorillonite-water system during the adsorption and desorption of water; hysteresis. Clays Clay Miner. 38, 485-492.

Galán, E. (2006) Chapter 14 Genesis of Clay Minerals, in: Faïza Bergaya, B.K.G.T., Gerhard, L. (Eds.), Developments in Clay Science. Elsevier, pp. 1129-1162.

Galán, E. and Ferrell, R.E. (2013) Chapter 3 - Genesis of Clay Minerals, in: Faïza, B., Gerhard, L. (Eds.), Developments in Clay Science. Elsevier, pp. 83-126.

Gates, W.P. (2005) Infrared spectroscopy and the chemistry of dioctahedral smectites, in: Kloprogge, T. (Ed.), Vibrational Spectroscopy of Layer Silicates and Hydroxides. CMS Workshop Lectures. The Clay Minerals Society, Aurora, pp. 125-168.

Gates, W.P., Slade, P.G., Manceau, A. and Lanson, B. (2002) Site Occupancies by iron in nontronites. Clays and Clay Minerals 50, 223-239.

Gilbert, B., Comolli, L.R., Tinnacher, R.M., Kunz, M. and Banfield, J.F. (2015) Formation and Restacking of Disordered Smectite Osmotic Hydrates. Clays and Clay Minerals 63, 432-442.

Glaeser, R., Mantine, I. and Méring, J. (1967) Observations sur la beidellite, Bulletin du Groupe Français des Argiles, pp. 125-130.

Gottwald, W. and Wachter, G. (1997) IR-Spektroskopie für Anwender. Wiley-VCH, Weinheim.

Grathoff, G. and Moore, D.M. (1996) Illite polytype quantification using wildfire© calculated x-ray diffraction patterns. Clays and Clay Minerals 44, 835-842.

Griffiths, P.R. (1983) Fourier transform infrared spectrometry. Science 222, 297-302.

Griffiths, P.R. (2006) Introduction to Vibrational Spectroscopy, Handbook of Vibrational Spectroscopy. John Wiley & Sons, Ltd.

Griffiths, P.R. and Pariente, G.L. (1988) Fourier transform infrared spectrometry: A tool for modern agricultural research, Beecher, G. R., pp. 223-246.

Grim, R.E. and Güven, N. (1978) Chapter 3 Geological Features and Mineralogical Studies of Major Bentonite Occurrences, in: Grim, R.E., Güven, N. (Eds.), Developments in Sedimentology. Elsevier, pp. 13-160.

Gualtieri, A.F., Ferrari, S., Leoni, M., Grathoff, G., Hugo, R., Shatnawi, M., Paglia, G. and Billinge, S. (2008) Structural characterization of the clay mineral illite-1M. Journal of Applied Crystallography 41, 402-415.

Guinier, A., Bokij, G.B., Boll-Dornberger, K., Cowley, J.M., Durovic, S., Jagodzinski, H., Krishna, P., de Wolff, P.M., Zvyagin, B.B., Cox, D.E., Goodman, P., Hahn, T., Kuchitsu, K. and Abrahams, S.C. (1984) Nomenclature of polytype structures. Report of the International Union of Crystallography Ad hoc Committee on the Nomenclature of Disordered, Modulated and Polytype Structures. Acta Crystallographica Section A 40, 399-404.

Güven, N. (1992) Molecular aspects of clay-water interactions, in: Güven, N., Pollastro, R.M. (Eds.), Clay–Water Interface and its Rheological Implications. The Clay Minerals Society, Boulder, pp. 1-80.

Hagen, W. and Tielens, A.G.G.M. (1982) The librational region in the spectrum of amorphous solid water and ice Ic between 10 and 140 K. Spectrochimica Acta Part A: Molecular Spectroscopy 38, 1089-1094.

Han, R., Hirose, T., Jeong, G.Y., Ando, J.-i. and Mukoyoshi, H. (2014) Frictional melting of clayey gouge during seismic fault slip: Experimental observation and implications. Geophysical Research Letters 41, 5457-5466.

Hanson, E.L., Schwartz, J., Nickel, B., Koch, N. and Danisman, M.F. (2003) Bonding self-assembled, compact organophosphonate monolayers to the native oxide surface of silicon. J. Am. Chem. Soc. 125, 16074-16080.

Harvey, C.C. and Lagaly, G. (2013) Chapter 4.2 - Industrial Applications, in: Faïza, B., Gerhard, L. (Eds.), Developments in Clay Science. Elsevier, pp. 451-490.

Head-Gordon, T. and Johnson, M.E. (2006) Tetrahedral structure or chains for liquid water. Proceedings of the National Academy of Sciences of the United States of America 103, 7973-7977.

Herrmann, H. and Bucksch, H. (2014) bound water, Dictionary Geotechnical Engineering/Wörterbuch GeoTechnik: English-German/Englisch-Deutsch. Springer Berlin Heidelberg, Berlin, Heidelberg, pp. 156-156.

Hosterman, J.W. and Patterson, S.H. (1992) Bentonite and fuller's earth resources of the United States. U.S. Geological Survey Bulletin 1522, 45.

Huheey, J.E. (1983) Inorganic chemistry : principles of structure and reactivity. Harper International, Cambridge, Md. London.

Iwata, S., Tabuchi, T. and Warkentin, B.P. (1995) Soil-water interactions: mechanisms and applications, Second Edition ed. Marcel Dekker, Inc, New York.

Johnston, C.T. (1996) Sorption of Organic Compounds on Clay Minerals: A surface functional group approach, in: Sawhney, B. (Ed.), Organic Pollutants in the Environment. Clay Minerals Society, pp. 1-44.

Johnston, C.T. (2010) Probing the nanoscale architecture of clay minerals. Clay Minerals 45, 245-279.

Johnston, C.T. and Premachandra, G.S. (2001) Polarized ATR-FTIR Study of Smectite in Aqueous Suspension. Langmuir 17, 3712-3718.

Johnston, C.T., Premachandra, G.S., Szabo, T., Lok, J. and Schoonheydt, R.A. (2012) Interaction of Biological Molecules with Clay Minerals: A Combined Spectroscopic and Sorption Study of Lysozyme on Saponite. Langmuir 28, 611-619.

Johnston, C.T., Sposito, G. and Erickson, C. (1992) Vibrational probe studies of water interactions with montmorillonite. Clays Clay Miner. 40, 722-730.

Kaden, H. (2012) Determination of frequency dependent complex dielectric permittivity and modeling of dielectric properties of clay-water mixtures containing swellable and non-swellable clay minerals at low water contents, Fakultät für Bauingenieur-, Geo- und Umweltwissenschaften. Universität Fridericiana zu Karlsruhe (TH), Karlsruhe, p. 335.

Kaiser, H. and Specker, H. (1956) Bewertung und Vergleich von Analyseverfahren. Z. Anal. Chem. Rev. 149, 46-66.

Kalinichev, A.G. and Kirkpatrick, R.J. (2002) Molecular dynamics modeling of chloride binding to the surfaces of calcium hydroxide, hydrated calcium aluminate, and calcium silicate phases. Chemistry of Materials 14, 3539-3549.

Kaufhold, S. (2006) Comparison of methods for the determination of the layer charge density (LCD) of montmorillonites. Applied Clay Science 34, 14-21.

Kaufhold, S. and Dohrmann, R. (2016) Distinguishing between more and less suitable bentonites for storage of high-level radioactive waste. Clay Minerals 51, 289-302.

Kaufhold, S., Dohrmann, R., Klinkenberg, M. and Noell, U. (2015) Electrical conductivity of bentonites. Applied Clay Science 114, 375-385.

Kaufhold, S., Dohrmann, R., Stucki, J.W. and Anastacio, A.S. (2011) Layer charge density of smectites - closing the gap between the structural formula method and the alkylammonium method. Clays and Clay Minerals 59, 200-211.

Komadel, P. (1999) Structure and Chemical Characteristics of Modified Clays, in: Misaelides, P., Macášek, F., Pinnavaia, T.J., Colella, C. (Eds.), Natural Microporous Materials in Environmental Technology. Springer Netherlands, pp. 3-18.

Komadel, P. (2003) Chemically modified smectites. Clay Minerals 38, 127-138.

Komadel, P. and Madejová, J. (2013) Chapter 10.1 - Acid Activation of Clay Minerals, in: Faïza, B., Gerhard, L. (Eds.), Developments in Clay Science. Elsevier, pp. 385-409.

Korb, J.P., McDonald, P.J., Monteilhet, L., Kalinichev, A.G. and Kirkpatrick, R.J. (2007) Comparison of proton field-cycling relaxometry and molecular dynamics simulations for proton-water surface dynamics in cement-based materials. Cement and Concrete Research 37, 348-350.

Köster, H.M. (1993) Dreischichtminerale oder 2:1 Schichtsilikate, in: Jasmund, K., G., L. (Eds.), Tonminerale und Tone Steinkopff Verlag, Darmstadt, pp. 42-58.

Köster, H.M. and Schwertmann, U. (1993) Zweischichtminerale, in: Jasmund, K. (Ed.), Tonminerale und Tone. Steinkopf Verlag, pp. 33-58.

Kozaki, T., Liu, J. and Sato, S. (2008) Diffusion mechanism of sodium ions in compacted montmorillonite under different NaCl concentration. Physics and Chemistry of the Earth 33, 957-961.

Kremer, F. and Schönhals, A. (2003) Broadband dielectric measurement techniques, in: Kremer, F., Schönhals, A. (Eds.), Broadband dielectric spectroscopy. Springer, pp. 35-56.

Kresse, G. and Furthmüller, J. (1996) Efficiency of ab-initio total energy calculations for metals and semiconductors using a plane-wave basis set. Comp. Mater. Sci. 6, 15-50.

Kresse, G. and Joubert, D. (1999) From ultrasoft pseudopotentials to the projector augmented-wave method. Phys. Rev. B 59, 1758-1775.

Kuligiewicz, A., Derkowski, A., Emmerich, K., Christidis, G.E., Tsiantos, C., Gionis, V. and Chryssikos, G.D. (2015a) Measuring the layer charge of dioctahedral smectite by O-D vibrational spectroscopy. Clays and Clay Minerals 63, 443-456.

Kuligiewicz, A., Derkowski, A., Szczerba, M., Gionis, V. and Chryssikos, G.D. (2015b) Revisiting the infrared spectrum of the water-smectite interface. Clays Clay Miner. 63, 15-29.

Kutzelnigg, A. and Königsheim, F. (1963) Die Einstellung der relativen Feuchte mit Hilfe von gesättigten Salzlösungen. Materials and Corrosion 14, 181-186.

Lagaly, G. (1981) Characterization of clays by organic-compounds. Clay Miner. 16, 1-21.

Lagaly, G. (1994) Layer charge determination by alkylammonium ions, in: Mermut, A. (Ed.), CMS work. Lect. The Clay Minerals Soc., Boulder, Colorado, pp. 1-46.

Lagaly, G. and Dékány, I. (2013) Chapter 8 - Colloid Clay Science, in: Faïza, B., Gerhard, L. (Eds.), Developments in Clay Science. Elsevier, pp. 243-345.

Lagaly, G. and Weiss, A. (1970a) Anordnung und Orientierung kationischer Tenside auf ebenen Silicatoberflächen Teil I: Darstellung der n-Alkylammoniumderivate von

glimmerartigen Schichtsilicaten. Kolloid-Zeitschrift und Zeitschrift für Polymere 237, 266-273.

Lagaly, G. and Weiss, A. (1970b) Anordnung und Orientierung kationischer Tenside auf Silicatoberflächen II. Paraffinähnliche Strukturen bei den n-Alkylammonium-Schichtsilicaten mit hoher Schichtladung (Glimmer). Kolloid-Zeitschrift und Zeitschrift für Polymere 237, 364-368.

Lagaly, G. and Weiss, A. (1970c) Anordnung und Orientierung kationischer Tenside auf Silicatoberflächen III. Paraffinartige strukturen bein-alkylammonium-schichtsilicaten mit mittlerer schichtladung (vermiculite). Kolloid-Zeitschrift und Zeitschrift für Polymere 238, 485-493.

Lagaly, G. and Weiss, A. (1971) Anordnung und Orientierung kationischer Tenside auf ebenen Silicatoberflächen. IV. Anordnung von n-Alkylammoniumionen bei niedrig geladenen Schichtsilicaten. Kolloid-Z. Z. Polym. 243, 48-55.

Laird, D.A. (2006) Influence of layer charge on swelling of smectites. Applied Clay Science 34, 74-87.

Laird, D.A. and Shang, C. (1997) Relationship Between Cation Exchange Selectivity and Crystalline Swelling in Expanding 2:1 Phyllosilicates. Clays and Clay Minerals 45, 681-689.

Lange, P. (1989) Evidence for disorder-induced vibrational mode coupling in thin amorphous SiO_2 films. J. Appl. Phys. 66, 201-204.

Lanson, B., Ferrage, E., Hubert, F., Pret, D., Mareschal, L., Turpault, M.P. and Ranger, J. (2015) Experimental aluminization of vermiculite interlayers: An X-ray diffraction perspective on crystal chemistry and structural mechanisms. Geoderma 249, 28-39.

Le Forestier, L., Muller, F., Villieras, F. and Pelletier, M. (2010) Textural and hydration properties of a synthetic montmorillonite compared with a natural Na-exchanged clay analogue. Applied Clay Science 48, 18-25.

Leonard, R.A. and Weed, S.B. (1967) Influence of Exchange Ions on the b-Dimensions of Dioctahedral Vermiculite. Clays Clay Miner. 15, 149-161.

Lever, T., Haines, P., Rouquerol, J., Charsley, E.L., Van Eckeren, P. and Burlett, D.J. (2014) ICTAC nomenclature of thermal analysis (IUPAC Recommendations 2014). Pure and Applied Chemistry 86, 545-553.

Low, P.F., Mitchell, J.K., Sposito, G. and Olphen, H.v. (1991) Clay-Water Interface and its Rheological Implications.

Low, P.F., Ravina, I. and White, J.L. (1970) Changes in b dimension of Na-montmorillonite with interlayer swelling. Nature 226, 445-446.

Lowell, S. (2006) Apparatus and method for water sorption measurement. Google Patents.

Mackenzie, R.C. and Mitchell, B.D. (1962) DIFFERENTIAL THERMAL ANALYSIS. Analyst 87, 420-&.

Madejova, J. (2003) FTIR techniques in clay mineral studies. Vib. Spectrosc. 31, 1-10.

Madejová, J., Bujdák, J., Janek, M. and Komadel, P. (1998) Comparative FT-IR study of structural modifications during acid treatment of dioctahedral smectites and hectorite. Spectrochim. Acta, Part A 54, 1397-1406.

Madejová, J., Janek, M., Komadel, P., Herbert, H.J. and Moog, H.C. (2002) FTIR analyses of water in MX-80 bentonite compacted from high salinary salt solution systems. App. Clay Sci. 20, 255-271.

Madejova, J., Keckes, J., Palkova, H. and Komadel, P. (2002) Identification of components in smectite/kaolinite mixtures. Clay Minerals 37, 377-388.

Madejova, J. and Komadel, P. (2001) Baseline studies of The Clay Minerals Society Source Clays: Infrared methods. Clays Clay Miner. 49, 410-432.

Madejova, J., Komadel, P. and Cicel, B. (1994) Infrared study of octahedral site populations in smectites. Clay Miner. 29, 319-326.

Mehra, O.P. and Jackson, M.L. (1960) Iron oxide removal from soils and clays by a dithionite-citrate-system buffered with sodium bicarbonate, in: Swineford, A. (Ed.), 7th National Conference on Clays and Clay Minerals. Pergamon Press, Washington, D.C., pp. 317-327.

Meier, L.P. and Kahr, G. (1999) Determination of the cation exchange capacity (CEC) of clay minerals using the complexes of copper(II) ion with triethylenetetramine and tetraethylenepentamine. Clays Clay Miner. 47, 393-397.

Méring, J. and Glaeser, R. (1954) Sur le rôle de la valence des cations exchangeables dans la montmorillonite, Bull. Soc. Fr. Mineral. Cristallogr., pp. 519-530.

Mermut, A. and G., L. (2001) Baseline studies of the clay minerals society source clays: layer-charge determination and charge characteristics of those minerals containing 2:1 layers. Clays and Clay Minerals 49, 393-397.

Michot, L.J. and Villiéras, F. (2013) Chapter 2.10 - Surface Area and Porosity, in: Faïza, B., Gerhard, L. (Eds.), Developments in Clay Science. Elsevier, pp. 319-332.

Moll, W.F. (2001) Baseline studies of the clay minerals society source clays: Geological origin. Clays and Clay Minerals 49, 374-380.

Monkhorst, H.J. and Pack, J.D. (1976) Special points for Brillouin-zone integrations. Phys. Rev. B 13, 5188-5192.

Moore, D.M. and Reynolds Jr., R.C. (1997) X-Ray Diffraction and the Identifiaction and analysis of Clay Minerals. Oxford University Press, Oxford.

Murray, H.H. (2006a) Chapter 3 Geology and Location of Major Industrial Clay Deposits, in: Haydn, H.M. (Ed.), Developments in Clay Science. Elsevier, pp. 33-65.

Murray, H.H. (2006b) Chapter 6 Bentonite Applications, in: Haydn, H.M. (Ed.), Developments in Clay Science. Elsevier, pp. 111-130.

Nieto, F., Mellini, M. and Abad, I. (2010) Teh role of H_3O^+ in the crystal structure of illite. Clays and Clay Minerals 58, 238-246.

Nilsson, A. and Pettersson, L.G.M. (2011) Perspective on the structure of liquid water. Chemical Physics 389, 1-34.

Olis, A.C., Malla, P.B. and Douglas, L.A. (1990) The rapid estimation of the layer charges of 2:1 expanding clays from a single alkylammonium ion expansion. Clay Miner. 25, 39-50.

Olivier, J.P. (1995) Modeling physical adsorption on porous and nonporous solids using density functional theory. Journal of Porous Materials 2, 9-17.

Pellenq, R.J.M., Lequeux, N. and van Damme, H. (2008) Engineering the bonding scheme in C-S-H: The iono-covalent framework. Cement and Concrete Research 38, 159-174.

Perdew, J.P., Chevary, J.A., Vosko, S.H., Jackson, K.A., Pederson, M.R., Singh, D.J. and Fiolhais, C. (1992) Atoms, molecules, solids, and surfaces: Applications of the generalized gradient approximation for exchange and correlation. Phys. Rev. B 46, 6671-6687.

Persson, I. (2010) Hydrated metal ions in aqueous solution: How regular are their structures? Pure and Applied Chemistry 82, 1901-1917.

Petit, S. (2006) Chapter 12.6 Fourier Transform Infrared Spectroscopy, in: Faïza Bergaya, B.K.G.T., Gerhard, L. (Eds.), Developments in Clay Science. Elsevier, pp. 909-918.

Petit, S., Caillaud, J., Righi, D., Madejová, J., Elsass, F. and Köster, H.M. (2002) Characterization and crystal chemistry of an Fe-rich montmorillonite from Ölberg, Germany. Clay Miner. 37, 283-297.

Petit, S. and Madejova, J. (2013) Chapter 2.7 - Fourier Transform Infrared Spectroscopy, in: Faïza, B., Gerhard, L. (Eds.), Developments in Clay Science. Elsevier, pp. 213-231.

Poinsignon, C., Cases, J.M. and Fripiat, J.J. (1978) Electrical polarization of water molecules adsorbed by smectites. An infrared study. Journal of Physical Chemistry 82, 1855-1860.

Poli, A.L., Batista, T., Schmitt, C.C., Gessner, F. and Neumann, M.G. (2008) Effect of sonication on the particle size of montmorillonite clays. Journal of Colloid and Interface Science 325, 386-390.

Prost, R. (1975) Interactions between adsorbed water molecules and the structure of clay minerals: Hydration mechanism of smectites, Int. Clay Conf. Clay Minerals Society, Mexico City, pp. 351-359.

Queeney, K.T., Weldon, M.K., Chabal, Y.J. and Raghavachari, K. (2003) The microscopic origin of optical phonon evolution during water oxidation of Si(100). The Journal of Chemical Physics 119, 2307-2313.

Ras, R.H.A., Schoonheydt, R.A. and Johnston, C.T. (2007a) Relation between s-Polarized and p-Polarized Internal Reflection Spectra: Application for the Spectral Resolution of Perpendicular Vibrational Modes. The Journal of Physical Chemistry A 111, 8787-8791.

Ras, R.H.A., Umemura, Y., Johnston, C.T., Yamagishi, A. and Schoonheydt, R.A. (2007b) Ultrathin hybrid films of clay minerals. Phys. Chem. Chem. Phys. 9, 918-932.

Ravina, I. and Low, P.F. (1972) Relation between Swelling, Water Properties and b-Dimension in Montmorillonite-Water Systems. Clays Clay Miner. 20, 109-123.

Richardson, I.G. (2004) Tobermorite/jennite- and tobermorite/calcium hydroxide-based models for the structure of C-S-H: applicability to hardened pastes of tricalcium silicate, beta-dicalcium silicate, Portland cement, and blends of Portland cement with blast-fumace slag, metakaolin, or silica fume. Cement and Concrete Research 34, 1733-1777.

Richmond, G.L. (2002) Molecular Bonding and Interactions at Aqueous Surfaces as Probed by Vibrational Sum Frequency Spectroscopy. Chemical Reviews 102, 2693-2724.

Rieder, M., Cavazzini, G., D'yakonov, Y.S., Frank-Kamenetskii, V.A., Gottardi, G., Guggenheim, S., Koval, P.V., Mueller, G., Neiva, A.M.R., Radoslovich, E.W., Robert, J.-L., Sassi, F.P., Takeda, H., Weiss, Z. and Wones, D.R. (1998) Nomenclature of the micas. Clays and Clay Minerals 46, 586-595.

Rouquerol, F., Rouquerol, J. and Llewellyn, P. (2013) Chapter 2.12 - Thermal Analysis, in: Faïza, B., Gerhard, L. (Eds.), Developments in Clay Science. Elsevier, pp. 361-379.

Rouquerol, J., Baron, G.V., Denoyel, R., Giesche, H., Groen, J., Klobes, P., Levitz, P., Neimark, A.V., Rigby, S., Skudas, R., Sing, K., Thommes, M. and Unger, K. (2012) The characterization of macroporous solids: An overview of the methodology. Microporous and Mesoporous Materials 154, 2-6.

Russell, J.D. and Farmer, V.C. (1964) Infra-red spectroscopic study of the dehydration of montmorillonite and saponite Clay Miner. Bull. 5, 443-464.

Russell, J.D., Farmer, V.C. and Velde, B. (1970) Replacement of OH by OD in layer silicates, and identification of the vibrations of these groups in infrared spectra, Mineralogical Magazine, pp. 869-879.

Russell, J.D. and Fraser, A.R. (1971) I.R. spectroscopic evidence for interaction between hydronium ions and lattice OH groups in montmorillonite. Clays Clay Miner. 19, 55-59.

Russell, J.D. and Fraser, A.R. (1994) Infrared methods, in: Wilson, M.J. (Ed.), Clay Mineralogy: Spectroscopic and Chemical Determinative Methods. Springer Netherlands, Dordrecht, pp. 11-67.

Sato, T., Murakami, T. and Watanabe, T. (1996) Change in layer charge of smectites and smectite layers in illite/smectite during diagenetic alteration. Clays Clay Miner. 44, 460-469.

Sato, T., Watanabe, T. and Otsuka, R. (1992) Effects of layer charge, charge location, and energy change on expansion properties of dioctahedral smectites. Clays Clay Miner. 40, 103-113.

Schnetzer, F., Thissen, P., Giraudo, N. and Emmerich, K. (2016) Unraveling the Coupled Processes of (De)hydration and Structural Changes in Na+-Saturated Montmorillonite. The Journal of Physical Chemistry C 120, 15282-15287.

Schoonheydt, R.A. and Johnston, C.T. (2013) Chapter 5 - Surface and Interface Chemistry of Clay Minerals, in: Faïza, B., Gerhard, L. (Eds.), Developments in Clay Science. Elsevier, pp. 139-172.

Schuttlefield, J.D., Cox, D. and Grassian, V.H. (2007) An investigation of water uptake on clays minerals using ATR-FTIR spectroscopy coupled with quartz crystal microbalance measurements. Journal of Geophysical Research: Atmospheres 112, n/a-n/a.

Sellin, P. and Leupin, O.X. (2013) The Use of Clay as an Engineered Barrier in Radioactive-Waste Management; A Review. Clays Clay Miner. 61, 477-498.

Sing, K.S.W., Everett, D.H., Haul, R.A.W., Moscou, L., Pierotti, R.A., Robert, J.-L. and Siemieniewska, T. (1985) Reporting physisorption data for gas/solid systems with

special reference to the determination of surface area and porosity (Recommendations 1984), Pure and Applied Chemistry, p. 603.

Skipper, N.T., Sposito, G. and Chou Chang, F.-R. (1995) Monte Carlo simulation of interlayer molecular structure in swelling clay minerals; 2, Monolayer hydrates. Clays and Clay Minerals 43, 294-303.

Slade, P.G., Stone, P.A. and Radoslovich, E.W. (1985) Interlayer structures of the two-layer hydrates of sodium- and calcium-vermiculites. Clays and Clay Minerals 33, 51-61.

Slonimskaya, M.V., Besson, G., Dainyak, L.G., Tchoubar, C. and Drits, V.A. (1986) Interpretation of the IR spectra of celadonites and glauconites in the region of OH-stretching frequencies. Clay Miner. 21, 377-388.

Smykatz-Kloss, W. (1974a) Sheet Silicates, Differential Thermal Analysis: Application and Results in Mineralogy. Springer Berlin Heidelberg, Berlin, Heidelberg, pp. 64-87.

Smykatz-Kloss, W. (1974b) Thermogravimetry and Differential Thermal Analysis, Differential Thermal Analysis: Application and Results in Mineralogy. Springer Berlin Heidelberg, Berlin, Heidelberg, pp. 1-2.

Sposito, G. (1984) The surface chemistry of soils. Oxford University Press.

Sposito, G. and Prost, R. (1982) Structure of water adsorbed on smectites. Chem. Rev. 82, 553-573.

Sposito, G., Prost, R. and Gaultier, J.P. (1983) Infrared spectroscopic study of adsorbed water on reduced-charge Na/Li montmorillonites. Clays Clay Miner. 31, 9-16.

Srodon, J. (1984) X-ray powder diffraction identification of illitic materials. Clays and Clay Minerals 32, 337-349.

Środoń, J. and McCarty, D.K. (2008) Surface area and layer charge of smectite from CEC and EGME/H_2O-retention measurements. Clays and Clay Minerals 56, 155-174.

Stepkowska, E.T., Pérez-Rodríguez, J.L., Maqueda, C. and Starnawska, E. (2004) Variability in water sorption and in particle thickness of standard smectites. Applied Clay Science 24, 185-199.

Stern, H.A., Rittner, F., Berne, B.J. and Friesner, R.A. (2001) Combined fluctuating charge and polarizable dipole models: Application to a five-site water potential function. The Journal of Chemical Physics 115, 2237-2251.

Steudel, A. (2009) PhD thesis: Selection strategy and modification of layer silicates for technical applications, Fakultät für Bauingenieur-, Geo- und Umweltwissenschaften. Universität Karlsruhe (TH), Karlsruher Mineralogische und Geochemische Hefte Schriftenreihe des Instituts für Mineralogie und Geochemie, Universität Karlsruhe (TH) Band 36, p. 258.

Steudel, A. and Emmerich, K. (2013) Strategies for the successful preparation of homoionic smectites. App. Clay Sci. 75-76, 13-21.

Steudel, A., Weidler, P.G., Schuhmann, R. and Emmerich, K. (2009) Cation Exchange Reactions of Vermiculite with Cu-Triethylenetetramine as Affected by Mechanical and Chemical Pretreatment. Clays and Clay Minerals 57, 486-493.

Stevens, R.E. (1945) A system for calculating analyses of micas and related minerals to end members. . U.S. Geol. Survey Bull. 950, 101-119.

Swenson, J., Bergman, R. and Longeville, S. (2001) A neutron spin-echo study of confined water. The Journal of Chemical Physics 115, 11299-11305.

Szczerba, M., Kuligiewicz, A., Derkowski, A., Gionis, V., Chryssikos, G.D. and Kalinichev, A.G. (2016) Structure and dynamics of water-smectite interfaces: Hydrogen bonding and the origin of the sharp O-D$_\Omega$ / O-H$_W$ infrared band from molecular simulations, in: Valúchová, J. (Ed.), MECC 2016. EQUILIBRIA, s.r.o., Kosice, Slovakia.

Tambach, T.J., Bolhuis, P.G., Hensen, E.J.M. and Smit, B. (2006) Hysteresis in Clay Swelling Induced by Hydrogen Bonding: Accurate Prediction of Swelling States. Langmuir 22, 1223-1234.

Tambach, T.J., Bolhuis, P.G. and Smit, B. (2004a) A Molecular Mechanism of Hysteresis in Clay Swelling. Angewandte Chemie International Edition 43, 2650-2652.

Tambach, T.J., Hensen, E.J.M. and Smit, B. (2004b) Molecular Simulations of Swelling Clay Minerals. The Journal of Physical Chemistry B 108, 7586-7596.

Tamura, K., Yamada, H. and Nakazawa, H. (2000) Stepwise Hydration of High-Quality Synthetic Smectite with Various Cations. Clays Clay Miner. 48, 400-404.

Tester, C.C., Aloni, S., Gilbert, B. and Banfield, J.F. (2016) Short- and Long-Range Attractive Forces That Influence the Structure of Montmorillonite Osmotic Hydrates. Langmuir 32, 12039-12046.

Thierfelder, C., Hermann, A., Schwerdtfeger, P. and Schmidt, W.G. (2006) Strongly bonded water monomers on the ice Ih basal plane: Density-functional calculations. Phys. Rev. B 74, 045422.

Thissen, P., Grundmeier, G., Wippermann, S. and Schmidt, W.G. (2009) Water adsorption on the α-Al2O3(0001) surface. Phys. Rev. B 80, 245403.

Thissen, P., Thissen, V., Wippermann, S., Chabal, Y.J., Grundmeier, G. and Schmidt, W.G. (2012) PH-dependent structure and energetics of H 2O/MgO(100). Surf. Sci. 606, 902-907.

Thommes, M., Kaneko, K., Neimark, A.V., Olivier, J.P., Rodriguez-Reinoso, F., Rouquerol, J. and Sing, K.S.W. (2015) Physisorption of gases, with special reference to the evaluation of surface area and pore size distribution (IUPAC Technical Report). Pure and Applied Chemistry 87, 1051-1069.

Tian, R., Seitz, O., Li, M., Hu, W., Chabal, Y.J. and Gao, J. (2010) Infrared Characterization of Interfacial Si−O Bond Formation on Silanized Flat SiO2/Si Surfaces. Langmuir 26, 4563-4566.

Tipton, T., Johnston, C.T., Trabue, S.L., Erickson, C. and Stone, D.A. (1993) Gravimetric / FTIR apparatus for the study of vapor sorption on clay films. Rev. Sci. Inst. 64, 1091-1092.

Tombácz, E. and Szekeres, M. (2004) Colloidal behavior of aqueous montmorillonite suspensions: the specific role of pH in the presence of indifferent electrolytes. Applied Clay Science 27, 75-94.

Tournassat, C. and Appelo, C.A.J. (2011) Modelling approaches for anion-exclusion in compacted Na-bentonite. Geochimica et Cosmochimica Acta 75, 3698-3710.

Tournassat, C., Neaman, A., Villieras, F., Bosbach, D. and Charlet, L. (2003) Nanomorphology of montmorillonite particles: Estimation of the clay edge sorption site

density by low-pressure gas adsorption and AFM observations. American Mineralogist 88, 1989-1995.

Tributh, H. and Lagaly, G. (1986a) Aufbereitung und Identifizierung von Boden- und Lagerstättentonen. I. Aufbereitung der Proben im Labor, GIT-Fachzeitschrift für das Laboratorium, pp. 524-529.

Tributh, H. and Lagaly, G. (1986b) Aufbereitung und Identifizierung von Boden- und Lagerstättentonen. II. Korngrößenanalyse und Gewinnung von Tonsubfraktionen, GIT-Fachzeitschrift für das Laboratorium, pp. 771-776.

Tsipursky, S.I. and Drits, V.A. (1984) The Distribution of Octahedral Cations in the 2:1 Layers of Dioctahedral Smectites Studied by Oblique-Texture Electron Diffraction. Clay Miner. 19, 177-193.

Ulbig, A. (1994) Vergleichende Untersuchungen an Bentoniten, Tuffen und sandig-tonigen Einschaltungen in den Bentonitlagerstätten der Oberen Süßwassermolasse Bayerns, Fakultät für Chemie, Biologie und Geowissenschaften. TU München, München.

Van Der Voort, P., Ravikovitch, P.I., De Jong, K.P., Neimark, A.V., Janssen, A.H., Benjelloun, M., Van Bavel, E., Cool, P., Weckhuysen, B.M. and Vansant, E.F. (2002) Plugged hexagonal templated silica: a unique micro- and mesoporous composite material with internal silica nanocapsules. Chemical Communications, 1010-1011.

van Olphen, H. (1965) Thermodynamics of interlayer adsorption of water in clays. I.—Sodium vermiculite. Journal of Colloid Science 20, 822-837.

Van Olphen, H. (1970) Determination of surface areas of clays—evaluation of methods, IUPAC Supplement to Pure and Applied Chemistry, Surface Area Determination, London, pp. 255-271.

Vantelon, D., Pelletier, M., Michot, L.J., Barres, O. and Thomas, F. (2001) Fe, Mg and Al distribution in the octahedral sheet of montmorillonites. An infrared study in the OH-bending region. Clay Minerals 36, 369-379.

Vega, A., Thissen, P. and Chabal, Y.J. (2012) Environment-Controlled Tethering by Aggregation and Growth of Phosphonic Acid Monolayers on Silicon Oxide. Langmuir 28, 8046-8051.

Wagner, J.F. (2013) Chapter 9 - Mechanical Properties of Clays and Clay Minerals, in: Faïza, B., Gerhard, L. (Eds.), Developments in Clay Science. Elsevier, pp. 347-381.

Wagner, N., Emmerich, K., Bonitz, F. and Kupfer, K. (2011) Experimental Investigations on the Frequency- and Temperature-Dependent Dielectric Material Properties of Soil. IEEE Trans. Geosci. Electron. 49, 2518-2530.

Wernet, P., Nordlund, D., Bergmann, U., Cavalleri, M., Odelius, M., Ogasawara, H., Naslund, L.A., Hirsch, T.K., Ojamae, L., Glatzel, P., Pettersson, L.G. and Nilsson, A. (2004) The structure of the first coordination shell in liquid water. Science 304, 995-999.

White, G.N. and Zelazny, L.W. (1988) Analysis and implications of the edge structure of dioctahedral phyllosilicates. Clays and Clay Minerals 36, 141-146.

Whitney, D.L. and Evans, B.W. (2010) Abbreviations for names of rock forming minerals. American Mineralogist 95, 185-187.

Wolters, F. (2005) Classification of montmorillonites, Fakultät für Bauingenieur-, Geo und Umweltwissenschaften. Universität Fridericiana zu Karlsruhe (TH), Karlsruhe, p. 169.

Wolters, F. and Emmerich, K. (2007) Thermal reactions of smectites—Relation of dehydroxylation temperature to octahedral structure. Thermochim. Acta 462, 80-88.

Wolters, F., Lagaly, G., Kahr, G., Nueesch, R. and Emmerich, K. (2009) A Comprehensive Characterization of Dioctahedral Smectites. Clays Clay Miner. 57, 115-133.

Xu, W., Johnston, C.T., Parker, P. and Agnew, S.F. (2000) Infrared study of water sorption on Na-, Li-, Ca-, and Mg-exchanged (SWy-1 and SAz-1) montmorillonite. Clays Clay Miner. 48, 120-131.

Yan, L., Roth, C.B. and Low, P.F. (1996) Changes in the Si−O Vibrations of Smectite Layers Accompanying the Sorption of Interlayer Water. Langmuir 12, 4421-4429.

Yan, L. and Stucki, J.W. (1999) Effects of Structural Fe Oxidation State on the Coupling of Interlayer Water and Structural Si−O Stretching Vibrations in Montmorillonite. Langmuir 15, 4648-4657.

Zelewsky, A.v. (1996) Stereochemistry of Coordination Compounds. John Wiley, Chichester.

Zöller, M. and Brockamp, O. (1997) 1M- and $2M_1$-illites: different minerals and not polytypes. Results from single-crystal investigations at the transmission electron microscope (TEM). European Journal of Mineralogy 9, 821-827.

Zviagina, B.B., McCarty, D.K., Srodon, J. and Drits, V.A. (2004) Interpretation of infrared spectra of dioctahedral smectites in the region of OH-stretching vibrations. Clays Clay Miner. 52, 399-410.

12 Appendix

XRF Datas

sample	BV-M0.2Na	BC-M0.2Na	SAz-2Na	SHc-0.2Na	VT-2Na	IIt-0.2Na
oxide	amount [%]	amount [%]	amount [%]	amount [%]	amount [%]	amount [%]
SiO_2	60.58	57.71	55.79	56.80	39.37	48,76
Al_2O_3	21.75	19.13	16.51	0.66	10.79	21,62
$Fe_2O_3(t)$	3.78	6.01	1.48	0.35	5.22	8,25
MnO	0.0	0.02	0.03	0.01	0.05	0,06
MgO	2.26	3.09	5.37	24.84	23.22	3,35
CaO	0.05	0.06	0.02	0.09	0.05	0,41
Na_2O	2.65	2.67	3.37	2.23	4.98	0,56
K_2O	0.04	0.58	0.04	0.11	0.03	5,79
TiO_2	0.137	0.188	0.208	0.03	0.572	0,521
P_2O_5	0.03	0.04	0.01	0.00	0.01	0,22
SO_3	0.026	0.011	0.014	0.01	0.006	0,064
Cr_2O_3	0.0002	0.004	0.0004	0.00	0.0835	0,0135
NiO	0.0001	0.001	0	0.00	0.0507	0,0061
LOI	9.62	11.88	17.89	13.75	15.48	9,82

XRD patterns in function of r.h. (BC-M0.2Na)
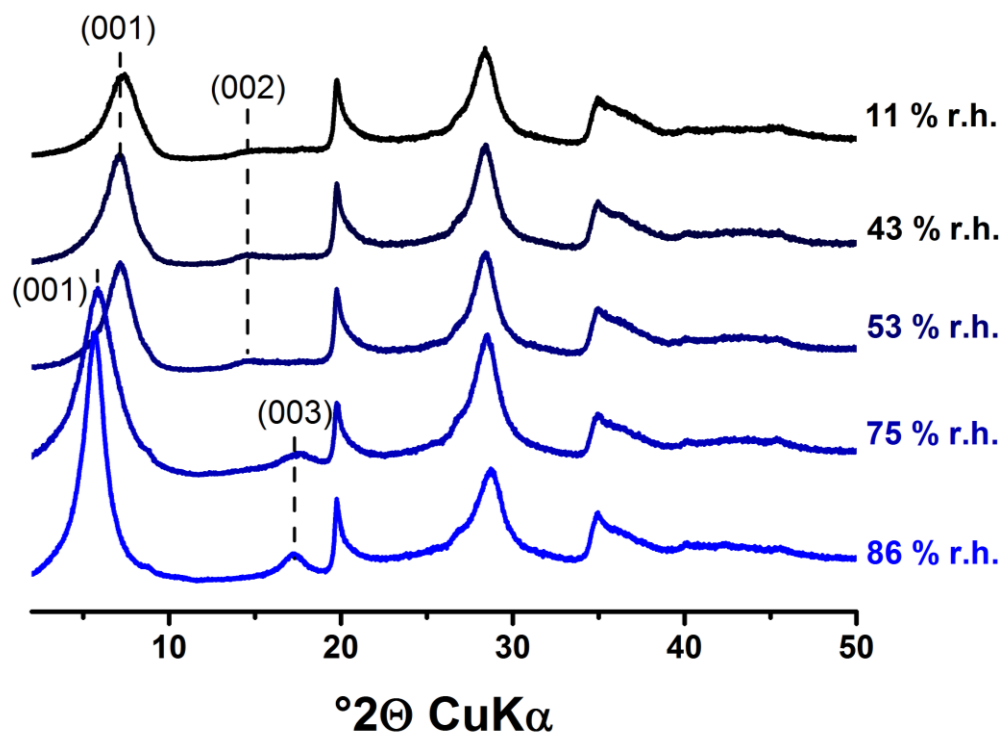
XRD patterns of powdered BC-M0.2Na as a function of r.h..

XRD patterns in function of r.h. (SAz-M2Na)
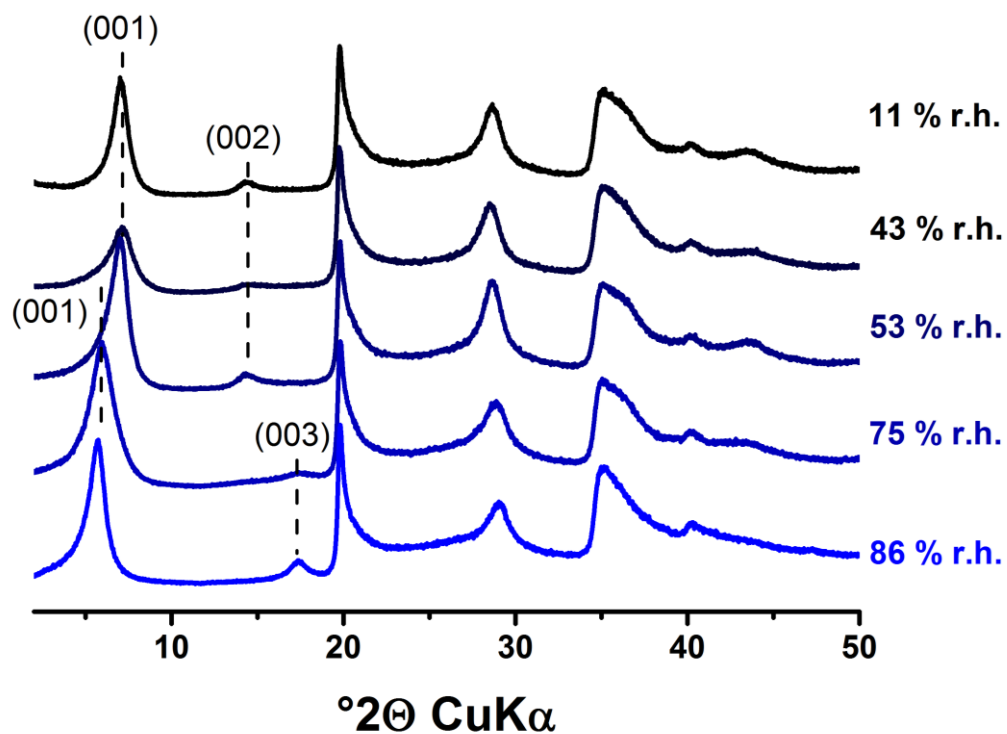
XRD patterns of powdered SAz-M2Na as a function of r.h..

XRD patterns in function of r.h. (SHc-0.2Na)
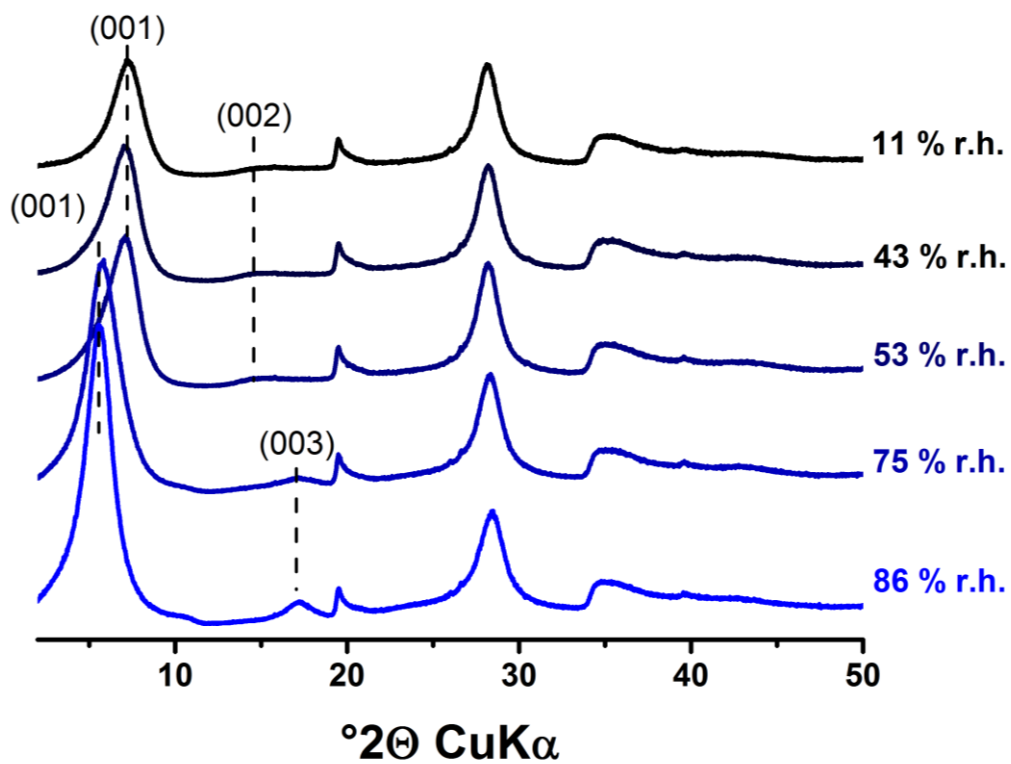
XRD patterns of powdered SHc-0.2Na as a function of r.h..